12-8-2008

Dynamic Supersonic Base Store Ejection Simulation Using Beggar

Michael D. Johnson

Dynamic Supersonic Base Store Ejection Simulation Using Beggar

THESIS

Michael D. Johnson,

AFIT/GAE/ENY/08-D01

DEPARTMENT OF THE AIR FORCE
AIR UNIVERSITY

AIR FORCE INSTITUTE OF TECHNOLOGY

Wright-Patterson Air Force Base, Ohio

The views expressed in this thesis are those of the author and do not reflect the official policy or position of the United States Air Force, Department of Defense, or the United States Government.

AFIT/GAE/ENY/08-D01

Dynamic Supersonic Base Store Ejection Simulation Using Beggar

THESIS

Presented to the Faculty

Department of Aeronautics and Astronautics

Graduate School of Engineering and Management

Air Force Institute of Technology

Air University

Air Education and Training Command

In Partial Fulfillment of the Requirements for the

Degree of Master of Science in Aeronautical Engineering

Michael D. Johnson, B.S.A.E.

December 2008

AFIT/GAE/ENY/08-D01

Dynamic Supersonic Base Store Ejection Simulation Using Beggar

Michael D. Johnson, B.S.A.E.

Approved:

Dr Raymond C. Maple (Chairman)	date
Dr Mark F. Reeder (Member)	date
Maj Andrew J. Lofthouse (Member)	date

Abstract

Static and dynamic conditions throughout various aft supersonic store separation events are examined using the Beggar CFD code. An 8.9° half angle cone is used for the carrier vehicle with an identically shaped store stowed within a hollow compartment in the aft section of the carrier body. Geometric and inertial properties are chosen so as to reflect a typical re-entry vehicle/store configuration. Both the Detached-Eddy simulation (DES) and Baldwin-Lomax (B-L) turbulence models are used in the study. Dynamic store separation simulations are implemented at a free stream Mach of 2.9 with a Reynolds number of $Re = 6.9 \times 10^6/m$ referenced against carrier base diameter. Analysis covered multiple dynamic separation events along with studies of the carrier/store body at various static conditions and configurations.

Dynamic store separation simulations show that a successful store separation is more likely to occur at high angle of attacks and high flight angles. When a low angle of attack and low flight angle is combined with inadequate ejection forces, it appears that the carrier and store will eventually impact each other due to tendency of the store to remain within the low drag wake region of the carrier. At higher ejection forces, angle of attack and flight angle become less important to a successful separation in that the store is ejected far enough downstream from the carrier that impact becomes improbable.

For all dynamic separation cases, a suction effect or negative drag force is observed acting on the store as it separates through the near wake region of the carrier body. The duration of the suction effect is found to be directly related to the initial free stream incidence of the two body system at store deployment. The carrier suction effect acting upon the store is not observed for identical static cases at fixed separation distances. Additionally, carrier/store body drag is found to up to 140% greater than carrier/store drag for the dynamic cases after applying a 15G ejection

load over 0.05 seconds. This finding indicates that an equivalent static system does not accurately capture the body forces of a dynamic store separation event.

When the store is stowed slightly offset of the carrier base prior to deployment, it separates further then when the store is stowed flush to the carrier. This phenomena is due to an increase in mean pressure and thus decrease in drag on the two-body system. This pre-deployment reduction in drag on the carrier effectively reduces the required ejection force necessary for a safe store separation.

Acknowledgements

I would like first to thank my wife for supporting me through the many late and long nights away from home as I worked on this thesis. Many thanks to my advisor, Dr. Raymond Maple, who was always willing to assist me with a problem no matter how trivial or time intensive. Thank you to my flight chiefs past and present, Greg Schaffer, Dave Turich, and Chris Mayrand for allowing me time away from the office to complete this work. Thanks also to Aaron McClung whose Linux expertise was invaluable to me. And finally, thanks to all my family and friends who showed continual interest and support throughout this process.

Michael D. Johnson

Table of Contents

Page

List of Figures

List of Tables

List of Symbols

Symbol		Page
n	time step	22
$\vec{R}$	residual	22
m	Newton sub-iteration	23
$\left\|\bar{A}_{Roe}\right\|$	Roe matrix	25
μ_t	eddy viscosity	28
x_{CP}	x center of pressure	37
x_{CG}	x center of gravity	37
α	angle of attack	44
γ	flight path angle	44
x_o/D	non-dimensional x-distance	57
y_o/D	non-dimensional y-distance	57
C_D	coefficient of drag	59

List of Abbreviations

Dynamic Supersonic Base Store Ejection Simulation Using Beggar

I. Introduction

The ability to support military operations anywhere in the world with a cost-effective, precise, and timely high-speed payload delivery system is an invaluable strategic asset. A maneuverable, re-usable, re-entry vehicle capable of dispensing a payload, cargo or weapon provides that capability. In order to reduce drag, as well as increase survivability, this type of vehicle must carry its payload internally. The F/A-22 RAPTOR and the F-35A/B/C LIGHTNING II are prime examples of a next generation fighter that carries internal weapons allowing stealthy and high-speed flight. Typically aircraft that carry stores internally, such as the F/A-22, will deploy them at subsonic speeds by opening a weapons bay door under the aircraft. This has the undesirable effect of increasing the vehicle's drag and radar cross-sectional area. Furthermore, if traveling at supersonic speeds, the store has to separate through a volatile environment. Separation at such high speeds entails traveling through the unsteady flow dynamics of the bomb bay, across a shear layer blanketing the bomb bay opening and then past a shock [16]. An alternative approach would expel the store aft, into the subsonic, low-pressure wake flow of the carrier vehicle, or as it relates to this study, a re-entry vehicle (RV). This provides a low-drag environment for the store to be released into, along with the added advantage of low aerodynamic heating [13].

An aft supersonic ejection from an RV presents its own share of concerns that must be addressed. Of primary concern is the difference in drag between the trailing and leading bodies upon separation. Any store ejected aft of a vehicle traveling at supersonic speeds will experience subsonic flow resulting in a lower drag than the lead vehicle. This could lead to a 'suction' effect where the trailing store actually impacts

the RV. In addition, due to the unsteady nature of base flow, forces and moments acting upon the ejected store will probably fluctuate requiring a structurally sound payload. Finally, the pitch and yaw rates due to the surrounding flow field of the two bodies during separation need to be considered since the dynamic stability of the two bodies could be affected [29].

Clearly, knowing the aerodynamic drag of the carrier and store body for a given RV is critical to accurately predicting the base store ejection. Generally, total aerodynamic drag for a projectile, ballistic shell, RV or any other axisymmetric blunt based body can be categorized into three types [12, 22]:

1. Pressure drag or wave drag, which is a result of shock formation on the body.
2. Viscous drag or shear forces, mostly from skin friction.
3. Base drag, due to the development of a low pressure recirculation area in the base flow region.

The base drag component has a tremendous effect on the total drag of a body, and can comprise over 50% of the the total drag [7, 12, 29]. Therefore, an accurate dynamic store ejection simulation will depend greatly on the accuracy of the base drag prediction [29]. However, because of the inherently unsteady nature of base flow, it is also the most difficult drag component to determine [12].

In the event of an aft store separation, understanding the aerodynamic influence that the trailing body has upon the the two-body system becomes important. Unfortunately, this phenomena is still not completely understood [27]. Experimental wind tunnel studies are not always reliable due to flow obstruction and interaction from body mounting structures and the wind tunnel itself [29]. Test mounts can skew the resulting data by altering the flow environment. Computational studies can also be difficult to implement because the already complicated flow structure (see Section 2.1.1) is further complicated by flow interaction from the trailing body. In addition, the lack of robust experimental data, without wind tunnel interference, makes it difficult to validate any computational results. Nonetheless, in the past 10-15 years

this subject has been gaining in interest. That interest focuses almost exclusively on determining the flow structure about segmented ballistic projectiles which, if properly aligned, can impart significantly more energy to a given target upon impact than a single projectile could [8, 18, 19, 27]. Methods, results, and conclusions found in the segmented projectile research can still be applied to the problem at hand, if not quantitatively, then at least qualitatively.

It also can become challenging to develop experimental or computational results describing a dynamic supersonic or hypersonic base store ejection where both the carrier body and store body are unconstrained in motion. Finding a test environment and measuring tools suitable to examine the phenomena is quite difficult. The Chimera technique, described in Section 1.3, makes it easier to numerically analyze a dynamic base flow ejection, but there are still myriad complicated flow structures existing, particularly in the near-base flow region. These flow interactions are difficult to capture in the computational domain and, without good experimental data to compare results to, impossible to validate.

1.1 Research Goals

The primary objective of this research is to successfully simulate and subsquently study the dynamic aft ejection of a store from the base of a sphere cone body traveling at supersonic speeds, using the computational fluid dynamics (CFD) Beggar code. In order to accurately demonstrate a separation event, both the carrier vehicle and the store will be unconstrained as it relates to the CFD simulation of motion during separation. This will allow the dynamic effects of the ejection force and the store interaction within the wake region on the lead body to be examined for both the store and the carrier vehicle.

1.2 Research Steps

A series of incremental steps will be taken in order to develop the computational solution to the dynamic supersonic base store ejection of an RV and evaluation of results:

1. Determine flow conditions, body geometry, and inertial properties including mass and moments of inertia
2. Create viscous grid domains for the carrier body and store
3. Consolidate and format the correct static flow required inputs to Beggar
4. Solve the static flow conditions for the RV while carrying the store at different AOA's and orientations
5. Generate dynamic store ejection inputs for Beggar
6. Perform multiple store ejection scenarios at different AOA's and orientations such that the store deploys safely
7. Evaluate resultant forces and moments on the leading and trailing bodies

1.3 Beggar Computational Fluid Dynamics Code

The Beggar CFD code was used to obtain the computational solutions for the current research. This software originated from the Air Force Wright Laboratory Armament Directorate, Eglin AFB, Forida. Since then, the code has been under continual development and improvement by the Computational Aeromechanics Team (CAT) at the Air Force SEEK EAGLE Office (AFSEO) at Eglin AFB. It serves in fulfilling the AFSEO's primary purpose, which is to certify all weapons carried on all (USAF) aircraft, internal or external.

Beggar is a 3D structured grid solver capable of providing a numerical solution to the Reynolds-Averaged Navier-Stokes (RANS) equations, the thin-layer Navier Stokes equations, and the Euler equations [2]. It conveniently allows for a solution domain to be composed of block-to-block, patched, and overset grids. These three

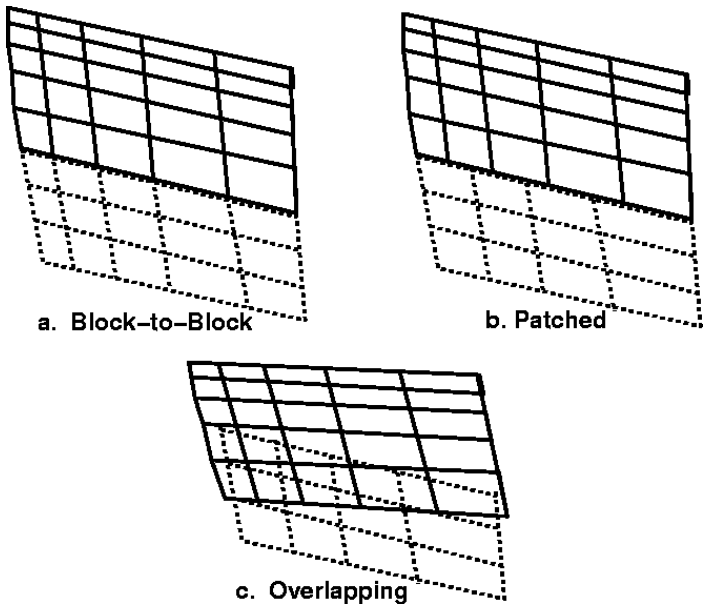

Figure 1.1: Illustration of Blocked, Patch, and Overlapped Grids [31]

types of grid communication are displayed in Figure 1.1. Utilizing multiple and overlapping grids, also known as the Chimera technique, enables the modeling of complex moving geometries that exist during a store separation event. With the Chimera scheme, moving bodies can move in all directions relative to a fixed inertial reference frame without generating new grids. Computations are performed on each body grid individually and the grid overlap regions communicate through interpolation and hole cutting algorithms. A disadvantage emerges, in that governing equations are not preserved in the overlap region [29]. Beggar uses a unique embedded grid data structure which combines the grid assembly, flow solution calculations, body force and moment calculations, and a 6+ degree-of-freedom ((6+)DOF) model into one code [20]. This results in simplifying the process of dynamic store trajectory prediction as well as increasing user ease.

1.4 Validation

As touched on earlier, computational solutions to a dynamic store base separation at supersonic speeds are difficult to validate. There are several main reasons for this:

1. Multi-body, three-dimensional shock interactions, the energetic free shear layer, and large unsteady recirculation regions of local pressure maxima and minima complicate computational solutions [5].
2. Very few free-moving experimental studies of store separation through the base have been undertaken and wind tunnel results are viewed as unreliable because of flow interference effects from test structures (see Section 2.1.2)
3. Experimental or numerical studies in the past have almost exclusively examined a deployable store whose mass is much less than the carrier vehicle. For the current research as well as future re-entry attack vehicles, the expelled store will have a mass greater than that of the carrier vehicle [24]. Thus, the relative inertial properties of smaller models will be significantly different than that of an RV type configuration

Although past research on this subject is qualitatively comparable to the problem of an RV expelling a store aft at supersonic speeds, it is generally not quantitatively so. This creates a problem in that there is no available data to validate the current research implemented in the Beggar CFD code, at least in the strictest sense of the word. However, historically, Beggar has proven itself to be highly capable and accurate when modeling two key components of a supersonic store separation event: base flow, and store separation dynamics.

Simko [29] investigated Beggar's computational results for base flow. A sphere-cone geometry with a 1/2 mm (.02 in) tip radius and 10° cone angle, exposed to Mach 2.9 flow conditions, was used for the study. Spalart-Allmaras (S-A), Detached-Eddy Simulation (DES), and Baldwin-Lomax (B-L) turbulence models were all used to model the turbulent viscous flow components in the computational domain. Simko

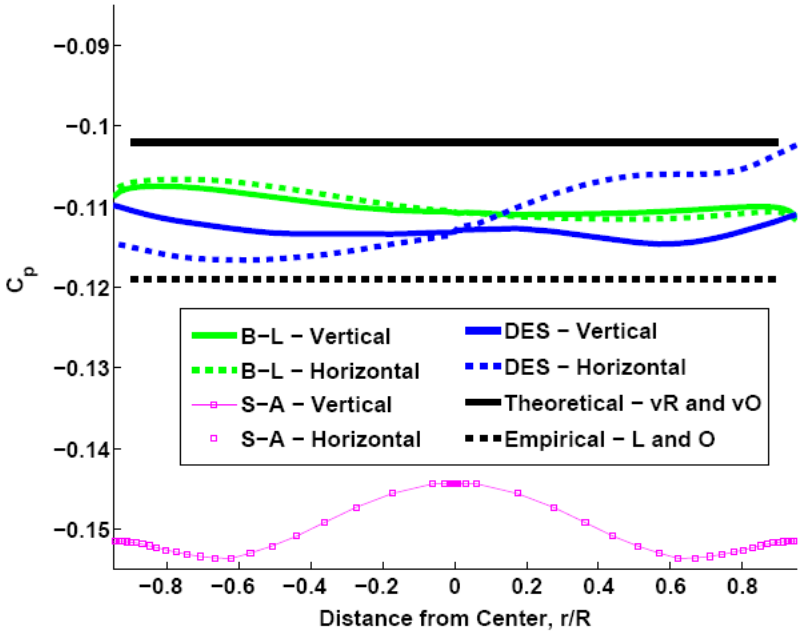

Figure 1.2: Mean Base Pressure Comparison by Simko [29]

found that Beggar was able to compute satisfactory mean base pressures using the DES and B-L turbulence models. Figure 1.2 summarizes his results. It can be seen that mean pressure values using both B-L and DES models fall well within analytical and empirical models of van Raalte *et al.* [21] and Lamb *et al.* [14] respectively. The B-L turbulence model is widely known to be deficient in capturing the intimate details of massively detached flow, particularily in the recirculation region [18,19]; Simko [29] found this to be true in his research as well. Conversely, the DES turbulence model provides a fairly accurate simulation of the detached flow in the near wake region of the base [18,19,29]. In his work, using bodies and flight conditions nearly identical to the current research, Simko [29] found Beggar to be capable of accurately evaluating base flow dynamics.

Babcock [2] supplies an exhaustive list of past research verifying Beggar's accuracy in store release and trajectory prediction simulations. The following highlight some of the notable validation successes, performed by various researchers, and detailed by Babcock [2]:

1. The dynamic ejection of a Mk-84 general purpose bomb from an F-15E aircraft at subsonic conditions
2. A multi-pronged effort including the comparisons of store trajectories to known wind tunnel data and a simulated ejection of three stores from a triple ejector pylon.
3. The separation of a GBU-31 bomb from an F-18C aircraft at transonic speeds
4. The (6+)DOF accuracy of two bodies in relative motion

Lastly, as stated in Section 1.3, Beggar is the high-fidelity computational tool used by the AFSEO to certify all weapons carried internally or externally on all aircraft. Beggar has shown it's accuracy in numerous validation efforts, and continues to reliably predict store separation dynamics today.

II. Background and Theory

2.1 Previous Research

A considerable amount of research has been invested into the phenomena of supersonic base flow and base drag [4, 6, 7, 9, 11, 12, 21, 29]. Less work has been performed when it comes to a trailing body's interaction with that of a leading body's wake [8, 18, 19, 27, 34]. Even fewer experimental or numerical studies have taken place inspecting the dynamic aft supersonic ejection of a store [5, 28]. In order to better understand the scope of the problem along with theory that addresses it, the aforementioned subjects are examined with further detail in the immediate sections.

2.1.1 Supersonic Base Flow and Base Drag. Before delving into a discussion of base drag, it will be helpful to first describe the important features of axisymmetric base flow itself. Figure 2.1 gives a visual representation of a two dimensional supersonic base flow at zero angle of attack (AOA). A developing boundary layer exists along the after-body which could be laminar or turbulent [21]. When the supersonic flow reaches the base corner, the flow boundary layer separates to create a free shear layer and expansion waves form off the base shoulder. A high speed inviscid flow is now separated from a very low speed flow recirculation area at the base. Further

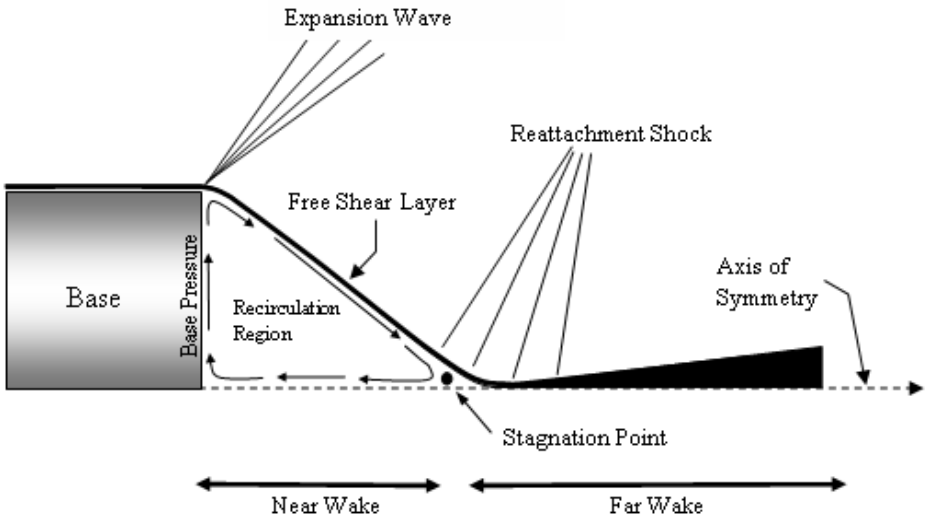

Figure 2.1: Base Flow Description

downstream, the shear layer is forced back toward the axis of symmetry [9], where compression shocks are formed. This is referred to as the reattachment point, characterized by a stagnation point on the centerline where the local mean velocity is zero [11,12,21]. As the re-compression of the shear layer takes place, mass is trapped and accelerated back toward the base (commonly described as flow entrainment). The characteristic re-circulation area associated with supersonic base flow then develops along the base; this is recognized as the near wake region. The flow eventually forms a trailing wake just downstream from the rear stagnation point [11,21]; this is known as the far wake region. The relationship between the re-circulation region and free shear layer dictates the magnitude of the base pressure and therefore the base drag. If the re-circulation region is large, a weaker expansion wave will develop, reducing the strength of the pressure expansion at the base. This results in higher base pressure and lower base drag. For a smaller re-circulation region, a stronger expansion wave will develop, lowering base pressure and increasing base drag.

Base pressure is typically expressed as a coefficient, C_{PB}, which takes the following form:

$$C_{PB} = \frac{p_B - p_\infty}{\frac{1}{2}\rho_\infty {V^2}_\infty} = \frac{2}{\gamma {M^2}_\infty}\left(\frac{p_B}{p_\infty} - 1\right) \tag{2.1}$$

If the base pressure p_B is small, then so is C_{PB} and therefore base drag increases. If base pressure is large, then vice versa.

With work closely related to this study, Simko [29] goes into a detailed account of base pressure. He makes two important points that are worth mentioning here:

1. The base pressure is closely correlated to Mach number.
2. Once the boundary layer has transitioned to turbulent, base pressure becomes almost independent of Reynolds number

The influence of increasing Mach on base pressure was investigated by Bulmer [4] who analyzed free flight test data for a 9° half angle cone at a range of different Mach numbers. Pressure was recorded on the vehicles base at two different locations

located radially from the base center. He concluded that the base pressure has a high dependence on free-stream Mach number (base pressure decreases with increasing Mach) and remains fairly constant across the base face, which is characteristic of most base flow [4, 10, 21, 29]. Since his data originates from flight test data, there are no wind tunnel effects, which makes for much more reliable information [29].

In Chapman's research [6] base pressure was found to be independent of Reynolds number for fully turbulent flows. If the boundary layer is assumed laminar, there is actually a strong correlation between Reynolds number and the base pressure coefficient [6]. The present work is focused on a stream-wise Reynolds number of $6.9 \times 10^6/m$ (referenced from a base diameter of one meter). Therefore, a well established turbulent boundary layer exists, and deviations in the Reynolds number should not have a noticeable effect on base pressure prediction.

A series of complicated flow interactions occurs in the near-wake region of a supersonic base (see Figure 2.1) that make it quite difficult to accurately predict numerically. Dutton [7] mentions those complicating factors, some of which are listed here:

1. The near shear layer exists under highly compressible conditions
2. Upon reattachment, the shear layer confronts a massive adverse pressure gradient
3. The expansion wave at the base corner has a direct effect on the initial near-wake structure which in turn affects the far wake region
4. A highly energetic and chaotic recirculation region within the shear layer

In addition, although there has been a good deal of experimental work done in determining base pressure/drag, there has been relatively very little experimental work done in extracting accurate mean and turbulent flow field measurements. Measurements of this kind are critical to understand these complicated flow structures as well as validating the Navier Stokes computational models [7]. Herron and

Dutton [10] had the following conclusions resulting from their measurements of the supersonic base flow field:

1. The maximum reverse velocity along the wake centerline occurs at approximately 57% of the distance from the base to reattachment
2. There are peaks of high turbulence intensity in the low speed recirculation region which becomes uniform as the far wake develops
3. Turbulent kinetic energy peaks closely following separation, inside the free shear layer

All flow characteristics listed above need to be considered because they will have an impact on a supersonic base store separation as it is forced into the near wake region of the lead body.

2.1.2 Trailing Body Base Flow Interaction. Figure 2.2 gives a simple visual representation of how a conical shaped base wake will change due to the influence of a trailing store. Initially, with the store placed close to the base, it will delay the onset of the compression shock, displacing the rear stagnation point further aft. As the store progresses deeper into the near wake region, the shear layer is unable to

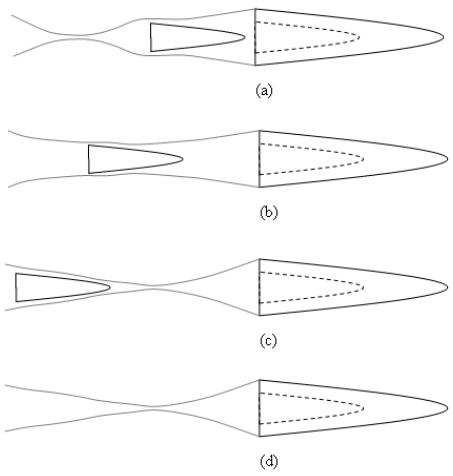

Figure 2.2: Example of Trailing Body Wake Interference

reattach and the trailing flow can't re-connect at the axis of symmetry. Finally, as the store pushes out into the far wake region, it will develop its own leading shock. At this point its interference effects on the parent body's base flow has ended with a successful separation.

One of the earlier, more comprehensive excursions into projectile flow dynamics was undertaken by Sahu *et al.* [27]. They investigated the flow field of a flared base projectile with small cylindrical trailing segments in the wake. These projectiles were positioned at one, four, six, eight, and ten base diameters (x/D) downstream from the base. Thin-layer Navier Stokes equations were implemented along with the Baldwin-Lomax turbulence model. With a small segment immersed in the near-wake zone ($x/D \leq 2$) of a Mach 4.4 flow, They observed an enlarged recirculation region stretching past the trailing body, essentially delaying flow reattachment. As the separation distance was increased to ten base diameters, a shock wave formed on the segment and gained strength. The introduction of a shock means higher pressure and therefore higher aerodynamic drag on the trailing body. Their conclusion was that at small distances from the parent projectile base ($x/D \leq 2$), the trailing small cylinder experiences negative drag, but as x/D increases, leading shocks form in front of the segment which act to increase the drag.

Several Computational studies by Ober *et al.* [18,19] in 1994 and 1995 also concentrated on the high speed flow dynamics of bodies in tandem at different distances from each other. These efforts differ from Sahu *et al.* [27] in that the trailing and leading projectiles had similar base diameters.

The set of numerical studies performed by Ober *et al.* [18] in 1994 examined two different tandem body configurations. The two leading-bodies investigated were a 12° cone-cylinder and a hemisphere-cylinder at Mach 4.95 airflow. A hemisphere-cylinder with identical base diameter was matched to both of the leading bodies as the trailing projectile. Trailing body off-axis and on-axis cases were investigated and aerodynamic results were generated. For the axisymmetric case, drag coefficients on

the tandem bodies at different separation distances were derived and are presented in Figure 2.3.

Some observations can be made based on Figure 2.3. In case A (axisymmetric cone-cylinder configuration) the drag coefficients for the leading and trailing bodies have basically the same order of magnitude. At distances very close to the lead body, the lead and trailing projectile's drag is essentially equal, indicating a sustained separation distance with no 'suction' effects. As the distance between the two bodies increases, so does the respective drag, which is consistent with results from Sahu *et al* [27]. Conversely, for case B (axisymmetric blunt body configuration) the drag coefficient for the leading body is so much larger than the trailing body, that the two bodies would probably impact. This is because the large wake shock generated by the blunt body increases it's drag, which keeps the trailing body's drag lower through longer separation distances.

For the off-axis case, force and moment coefficients on the trailing projectile, submerged in the leading body wake at various small off-axis displacements were found. The results suggested that as the trailing body is displaced radially (from the

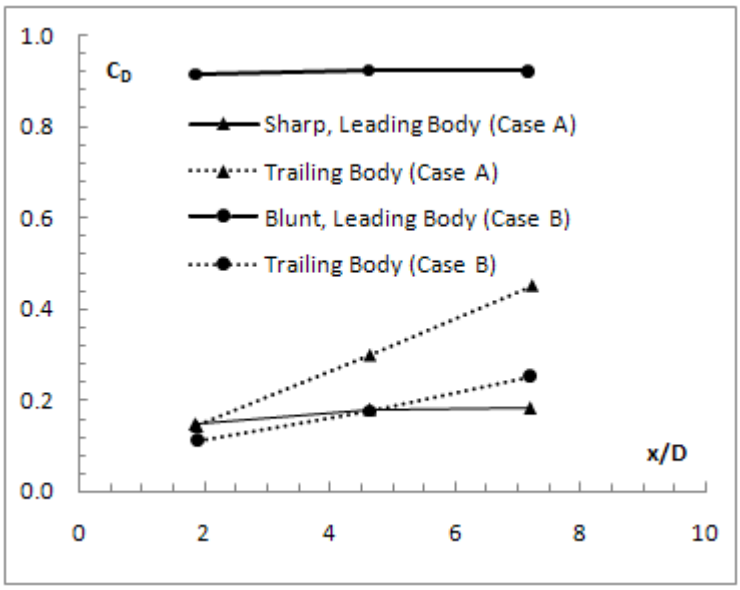

Figure 2.3: Segmented Body Drag Coefficient Comparison at Varying Separation Distances [18]

centerline to 20% of the leading body base radius), the coefficient of lift (C_L) becomes negative and the pitching moment (C_M) increases. Predictably, the drag will increase as the trailing body is gradually exposed to more of the free stream air flow. Ober *et al.* [18] notes that the negative C_L indicates that the trailing body will tend to push to the wake centerline, which is stabilizing maneuver. But the increasing pitching moment could eventually have a destabilizing effect on the trailing body, possibly ejecting it from the wake center.

In a 1995 follow-on study, Ober *et al.* [19] investigated the same type of tandem body configurations, but expanded the radial distance offset from the centerline to 70% of the base radius. Likewise, in a closely related effort, Erengil *et al.* [8], initiated a series of experimental wind tunnel tests on identical tandem body configurations. Both experimental and computational efforts concentrated on separation distances that immersed the trailing body in the near wake of the leading body. The concurrent studies produced interesting results. Figure 2.4 compares the experimentally derived aerodynamic forces and moments to the computational aerodynamic force and moment results, with excellent agreement between the two. Consistent with the

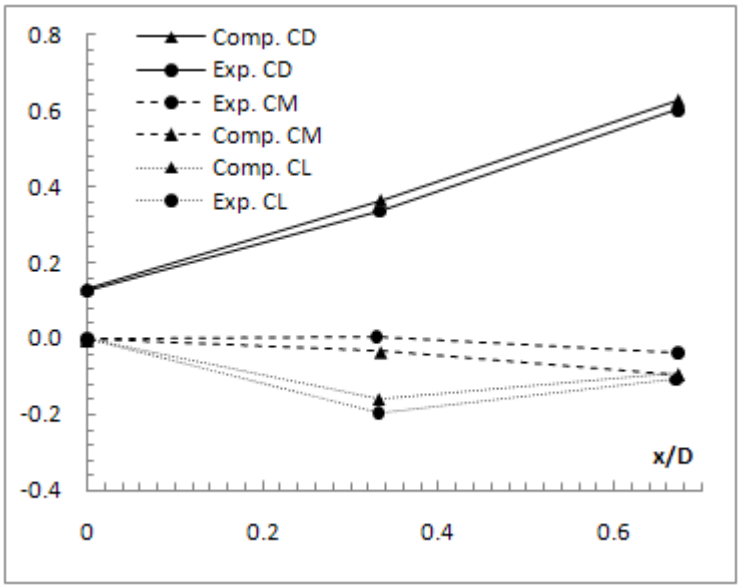

Figure 2.4: Trailing Body Off-Axis Force Coefficient Comparison at Varying Separation Distances by Ober *et al.* [19] 1995

1994 work by Ober *et al.* [18], as the rear body's radial offset increases, it's drag increases almost linearly. Although the trailing body's C_L fluctuates somewhat, it remains negative, which acts to force it back towards the centerline. Finally, C_M was observed slightly decreasing for the computational results and staying nearly zero for the experimental results [19]. Recall that in their 1994 work, Ober *et al.* [18] found that for short radial distances ($\leq 20\%$) of the base radius), C_M was found to increase with a pitch up moment. However, it is apparant in the follow up study that as the radial offset increases to 70% of the base radius, the pitching moment levels off and even decreases. Studies by Ober *et al.* [18, 19] and Erengil *et al.* [8] predict that a projectile located in the near wake of a lead body tends to remain stable and within that wake. This is a helpful insight that can be qualitatively compared to the results of this study.

2.1.3 Dynamic Base Store Ejection. Butler *et al.* [5] experimentally modeled a store deployment aft of a body in supersonic flow in the early 1990's. Testing took place at the Aeroballistic Research Facility (ARF) at Eglin AFB, Florida. The facilities at ARF are used to propel projectiles to high velocities by means of powder guns, air guns, and light-gas guns [5] in a closed testing environment. Ballistic shell range testing is useful in that body shapes similar to an RV, subjected to flow conditions similar to that of an RV, can be examined in a closed environment with no test structure interference. To visualize the flow characteristics, a 'Holographic Interferometry Testing' station, which captures images that can be decomposed to density flow-field data, was used. The carrier body was essentially a ballistic, cone shaped shell with a flared base. It's internally carried store was identically shaped, but it's base diameter was scaled to 20% of the carrier base diameter. Each of the bodies was designed for aerodynamic stability with a static margin over 5%. Two variations of a spring type ejection system were implemented which ejected the store aft almost immediately as the carrier/store package was launched. Ejection velocities of 20 ft/s (6.1 m/s) were realized. Multiple store-ejection tests, at different ejection

forces, were performed with images of the flow characteristics captured at locations down-range.

Figure 2.5 is an example of one such image, showing the store displaced almost six base diameters from the leading projectile base. Note that the store is beginning to pitch down, with the nose exposed to supersonic flow and the base still submerged in subsonic flow. Importantly, Butler *et al.* [5] concluded that store motion was not significantly detrimentally effected as it traversed and exited the leading body flow field. Still, unintended asymmetric ejection forces along with poor inertial properties were cited as causing some instability in the trailing model and complicating store deployment.

Computational studies simulating a supersonic base ejection event were completed by Sahu and Nietubicz [28] in 1993. Sahu *et al.* [28] used chimera overset grids to numerically derive the drag coefficients of single and dual trailing small cylindrical segments in the wake of a lead body with a flared base during a dynamic store separation. The Reynolds-averaged thin-layer Navier-Stokes equations were numerically solved and the Baldwin-Lomax turbulence model handled viscous flow interaction.

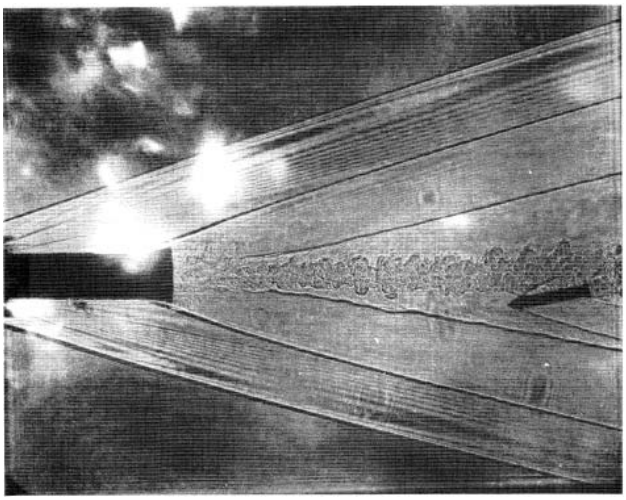

Figure 2.5: Store Separation Density Flow Field Image from Ballistic Range Testing [5]

Static trailing projectile configurations at different separation distances were compared to the dynamic store separation results.

In this case, a cylindrical segment was ejected aft of the carrier body at ejection velocities of over 90 m/s (295 ft/s). In Figure 2.6, experimental results are compared to the numerical results by Sahu and Neitubicz [28]. Figure 2.6(a) provides drag coefficients for the trailing body as a function of separation distance in Calibers (1 Caliber = the diameter of leading body cylindrical section before the flared base). Figure 2.6(b) compares separation distance in Calibers to time from separation. For the dynamic case, at separation distances ≤ 2 Calibers, the trailing body is still well submerged within the subsonic wake of the trailing body and experiences negative drag. As the trailing projectile moves further downstream, a leading shock forms on the segment and drag increases.

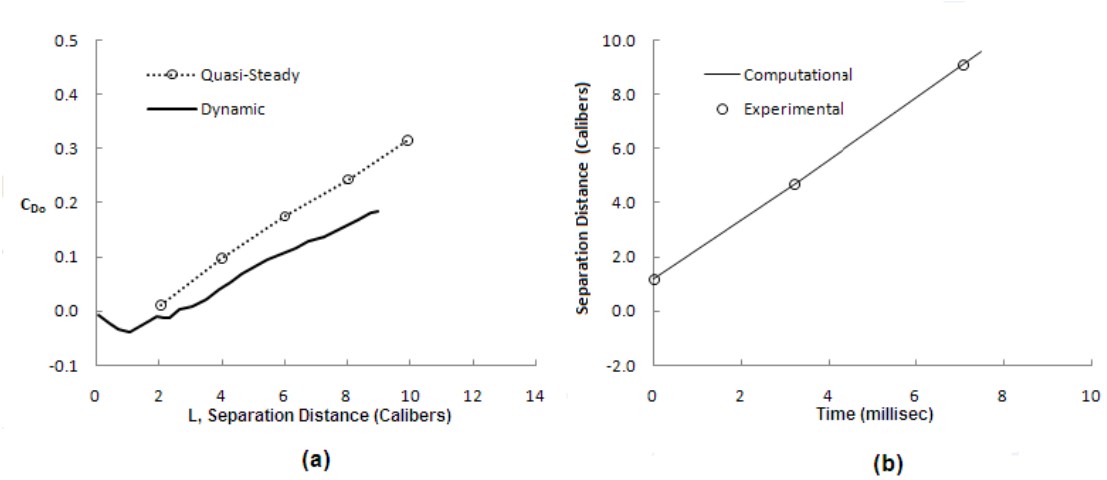

Figure 2.6: (a) Trailing Projectile Drag Coefficient [28]; (b) Trailing Projectile Separation Distance vs. Time [28]

2.2 Governing Equations

The conservation of mass, conservation of momentum and conservation of energy dictate the dynamic behavior of a fluid to make up what is known as the conservation laws [33] which can be applied to a continuum flow within an arbitrary control volume. If multiple components exist in a flow or they are reacting, then auxiliary equations are required. For the purposes of this study, the flow is assumed uniform and non-reacting. With the assumptions of a Newtonian fluid (fluid shear stress is linearly proportional to the fluid velocity gradient) the conservation laws and associated viscous stress components are assembled into the well known Navier-Stokes equations of motion, presented in integral form below:

$$\int_{\mathcal{V}} \frac{\partial \vec{Q}}{\partial t} d\mathcal{V} + \oint_{\mathcal{A}} (\vec{F}_c - \vec{F}_v) d\mathcal{A} = \int_{\mathcal{V}} \vec{W} d\mathcal{V} \tag{2.2}$$

Where $\vec{W}$ is a source term which includes body forces. For this problem all body forces are neglected, which results in the simplified form of the Navier-Stokes equations below:

$$\int_{\mathcal{V}} \frac{\partial \vec{Q}}{\partial t} d\mathcal{V} + \oint_{\mathcal{A}} (\vec{F}_c - \vec{F}_v) d\mathcal{A} = 0 \tag{2.3}$$

$\mathcal{V}$ represents the cell volume and $\vec{Q}$ consists of the conservative variables shown in vector form below:

$$\vec{Q} = \begin{bmatrix} \rho \\ \rho u \\ \rho v \\ \rho w \\ E_t \end{bmatrix} \tag{2.4}$$

Where ρ represents density, u, v, and w are component velocities in the three-dimensional Cartesian coordinate system, and E_t is total energy per unit mass [3] given as

$$E_t = \rho \left(\hat{u} + \frac{1}{2} \left| \vec{V} \right|^2 \right) \tag{2.5}$$

and $\hat{u}$ is the internal energy.

The convective fluxes, $\vec{F}_c$ describe the exchange of mass, momentum, and energy across the boundary face of the cell control volume. In this research and others like it, moving and overset grids are utilized. It becomes necessary to solve the governing equations on a moving grid. Therefore, $\vec{F}_c$, must be defined relative to the motion of the grid as developed in the following [3]:

$$\vec{F}_c = \begin{bmatrix} \rho V_r \\ \rho u V_r + n_x p \\ \rho v V_r + n_y p \\ \rho w V_r + n_z p \\ (E_t + p)V + V_t p \end{bmatrix} \tag{2.6}$$

Where V_t is defined as the contravariant velocity, or velocity normal to the cell surface element $d\mathcal{A}$ of the control volume [3], and directly evaluates the grid motion:

$$V_t = n_x \frac{dx}{dt} + n_y \frac{dy}{dt} + n_z \frac{dz}{dt} \tag{2.7}$$

Likewise, V_r represents the contravariant velocity *relative* to the motion of the grid:

$$V_r = V - V_t = n_x u + n_y v + n_z w - V_t \tag{2.8}$$

The viscous fluxes $\vec{F}_v$ are presented next:

$$\vec{F}_v = \begin{bmatrix} 0 \\ n_x \tau_{xx} + n_y \tau_{xy} + n_z \tau_{xz} \\ n_x \tau_{yx} + n_y \tau_{yy} + n_z \tau_{yz} \\ n_x \tau_{zx} + n_y \tau_{zy} + n_z \tau_{zz} \\ n_x \Theta_x + n_y \Theta_y + n_z \Theta_z \end{bmatrix} \tag{2.9}$$

where

$$\begin{aligned}\Theta_x &= u\tau_{xx} + v\tau_{xy} + w\tau_{xz} + k\frac{\partial T}{\partial x} \\ \Theta_y &= u\tau_{yx} + v\tau_{yy} + w\tau_{yz} + k\frac{\partial T}{\partial y} \\ \Theta_z &= u\tau_{zx} + v\tau_{zy} + w\tau_{zz} + k\frac{\partial T}{\partial z}\end{aligned} \tag{2.10}$$

describe the work performed by the viscous stresses and heat conduction in the fluid.

The viscous stresses, or frictional forces between the fluid and element surface, are described by the stress tensor $\overline{\tau}$ [3]:

$$\overline{\tau} = \begin{bmatrix} \tau_{xx} & \tau_{xy} & \tau_{xz} \\ \tau_{yx} & \tau_{yy} & \tau_{yz} \\ \tau_{zx} & \tau_{zy} & \tau_{zz} \end{bmatrix} \tag{2.11}$$

in which the following relationship exists:

$$\begin{aligned}\tau_{xx} &= \lambda\left(\frac{\partial u}{\partial x} + \frac{\partial v}{\partial y} + \frac{\partial w}{\partial z}\right) + 2\mu\frac{\partial u}{\partial x} \\ \tau_{yy} &= \lambda\left(\frac{\partial u}{\partial x} + \frac{\partial v}{\partial y} + \frac{\partial w}{\partial z}\right) + 2\mu\frac{\partial v}{\partial y} \\ \tau_{zz} &= \lambda\left(\frac{\partial u}{\partial x} + \frac{\partial v}{\partial y} + \frac{\partial w}{\partial z}\right) + 2\mu\frac{\partial w}{\partial z} \\ \tau_{xy} &= \tau_{yx} = \mu\left(\frac{\partial u}{\partial y} + \frac{\partial v}{\partial x}\right) \\ \tau_{xz} &= \tau_{zx} = \mu\left(\frac{\partial u}{\partial z} + \frac{\partial w}{\partial x}\right) \\ \tau_{yz} &= \tau_{zy} = \mu\left(\frac{\partial v}{\partial z} + \frac{\partial w}{\partial y}\right)\end{aligned} \tag{2.12}$$

where μ is the dynamic viscosity coefficient and λ is the so-called second viscosity coefficient.

Implementing Stokes hypothesis $\lambda + \frac{2}{3}\mu = 0$, simplifies the normal viscous stresses τ_{xx}, τ_{yy}, τ_{yy} and gives the following:

$$\begin{aligned}\tau_{xx} &= 2\mu\left(\frac{\partial u}{\partial x} - \frac{1}{3}\nabla\cdot\vec{v}\right) \\ \tau_{yy} &= 2\mu\left(\frac{\partial v}{\partial y} - \frac{1}{3}\nabla\cdot\vec{v}\right) \\ \tau_{yy} &= 2\mu\left(\frac{\partial w}{\partial z} - \frac{1}{3}\nabla\cdot\vec{v}\right)\end{aligned} \tag{2.13}$$

Typically, the governing equations are re-formulated into a non-dimensional form. This way flow parameters can be implemented independently of each other. There is also an added advantage in that all flow variables become normalized with their values falling between known limits. Beggar non-dimensionalizes flow variables as seen below [30]:

$$\begin{aligned} &u^* = u/a_\infty \qquad v^* = v/a_\infty \qquad w^* = w/a_\infty \\ &\rho* = \rho/\rho_\infty \quad p^* = p/p_\infty {a_\infty}^2 \quad t^* = ta_\infty/L_{ref} \quad E_t^* = E_t/\rho_\infty {a_\infty}^2 \end{aligned} \tag{2.14}$$

where ρ_∞ and a_∞ are freestream density and speed of sound respectively.

2.3 Flow Discretization

2.3.1 Navier Stokes. In order to use the Navier-Stokes equations to solve any type of practical flow problem, a numerical solution must be obtained. Almost all solution strategies achieve this by first spatially and then temporally discretising the flow variables [3]. For Beggar, physical space is discretized using a structured, finite-volume, cell-centered scheme where it is partitioned into a series of hexahedra (3D) grid cells which describe the computational domain. Cell coordinates are uniquely identified in the computational space through a coordinate transform which greatly simplifies spatial discritisation. Beggar implicitly discretises the Navier-Stokes equations in time using a first order Euler scheme [3, 26]:

$$\frac{\mathcal{V}_I}{\Delta t_I}\Delta\vec{Q}_I^n = -\vec{R}_I^{n+1} \tag{2.15}$$

where I is the given control volume, n is the current time step, and $\vec{R}^{n+1}$ is the vector of the sum of the fluxes ($\vec{F}_c$, $\vec{F}_v$), or the residual, at time step $n+1$. Next, the residual, $\vec{R}^{n+1}$, is linearized resulting in:

$$\vec{R}_I^{n+1} \approx \vec{R}_I^n + \left(\frac{\partial\vec{R}}{\partial\vec{Q}}\right)_I \Delta\vec{Q}_I^n \tag{2.16}$$

where $\Delta\vec{Q}_I^n = \vec{Q}_I^{n+1} - \vec{Q}_I^n$.

The linearized residual, $\vec{R}^{n+1}$, is substituted back into Eq. 2.15 and the following first order time accurate implicit scheme results [3]:

$$\left[\frac{\mathcal{V}_I}{\Delta t_I} + \left(\frac{\partial\vec{R}}{\partial\vec{Q}}\right)_I\right]\Delta\vec{Q}^n = -\vec{R}_I^n \tag{2.17}$$

where the left-hand side in brackets of Eq. 2.17 is referred to as the implicit operator and the right-hand side is called the explicit operator. The explicit operator determines spatial order of accuracy [3]. The flux Jacobian, $(\partial\vec{R})/(\partial\vec{Q})$, takes the following form:

$$\frac{\partial\vec{R}}{\partial\vec{Q}} = \sum\left(\frac{\partial\vec{F}_c^n}{\partial\vec{Q}} - \frac{\partial\vec{F}_v^n}{\partial\vec{Q}}\right) \tag{2.18}$$

and the residual, or explicit operator, $\vec{R}^n$ can be written as:

$$\vec{R}^n = \sum\left(\vec{F}_c^n - \vec{F}_v^n\right) \tag{2.19}$$

In Beggar, the flux-Jacobians and the residuals are determined using either the Steger-Warming flux splitting scheme (Section 2.3.2) or the Roe upwind scheme (Section 2.3.3).

To compute a time accurate solution to an unsteady flow problem, Beggar applies Newtons Method to Eq. 2.15. The full method, applied in Beggar and given at time n and Newton sub-iteration m, is as follows [26]:

$$\begin{aligned}\frac{\mathcal{V}}{\Delta T^{n,m}}\Delta Q^{n,m+1} + \left[\left(\frac{\partial\vec{R}}{\partial\vec{Q}}\right)\Delta\vec{Q}^{n,m+1} + \left(\frac{\partial\vec{R}}{\partial\bar{\vec{Q}}}\right)\Delta\bar{Q}^{n,m+1}\right] \\ = \left[\frac{\left(\vec{Q}^{n+1,m} - \vec{Q}^n\right)}{\Delta t}\mathcal{V} + \vec{R}^{n,m}\right]\end{aligned} \tag{2.20}$$

where $\vec{R}^{n,m} = \vec{R}\left(\vec{Q}^{n,m}, \bar{Q}^{n,m}, \tilde{Q}^{n,m}\right)$.

Notice that Eq. 2.20 handles the discretization of the flow variables in the cells within the grid ($\Delta\vec{Q}$ and $\vec{Q}$) as well as the 'ghost' cell variables ($\Delta\bar{Q}$ and $\bar{Q}$) which are required to satisfy the desired boundary conditions. A diagonal matrix ΔT replaces the fixed time step with a variable time step in the iterative solution. Note that $\vec{R}$ is now a function of $\vec{Q}$ and $\bar{Q}$, as well as $\tilde{Q}$ which holds the vectors of the stored flow variables across grid overlap regions.

At every time step $n+1$, Eg. 2.20 is solved for $\Delta\vec{Q}^{n+1,m+1}$ by iterating through $m+1$ sub iterations until reaching a user specified max Newton sub-iteration count or meeting a selected convergence tolerance. Beggar accomplishes this is by using the symmetric Gauss-Seidel relaxation scheme implemented as follows [26]:

$$\begin{aligned}
&\left[l^{n+1,m} + (1-\pi)\, D^{n+1,m}\right] \Delta\vec{Q}^{n+1,m+1,l+1/2} \\
&\qquad + \left(\pi D^{n+1,m} + u^{n+1,m}\right) \Delta\vec{Q}^{n+1,m+1,l+\pi} \\
&= -\left[\frac{\left(\vec{Q}^{n+1,m} - \vec{Q}^{n}\right)}{\Delta t}\vec{\mathcal{V}} + \vec{R}^{n+1,m}\right] - \frac{\partial\vec{R}}{\partial\bar{Q}}\Delta\bar{Q}^{n+1,m+1,l}
\end{aligned} \tag{2.21}$$

Here, l stands for the number of 'inner' iterations and π specifies whether the inner iterations progress in a forward sweep or backward sweep. The matrices $l^{n+1,m}$, $D^{n+1,m}$, and $u^{n+1,m}$ fill the coefficient matrix for $\Delta\vec{Q}^{n+1,m+1}$. By the time the inner iterations have converged, an implicit update to the boundary conditions will have taken place.

2.3.2 Steger-Warming Flux Splitting Scheme. The Steger-Warming flux-vector splitting scheme takes the flux vector and decomposes it into two parts according to their eigenvalues. It spatially discretises the two parts of the flux vector using an upwind scheme which can distinguish the wave propagation direction. The convective fluxes are first divided into a positive and negative part [3]:

$$\vec{F}_c = \vec{F}_c^{+} + \vec{F}_c^{-} \tag{2.22}$$

with the fluxes defined as

$$\vec{F}_c^{\pm} = \bar{A}_{SW}^{\pm}\vec{Q} = \left(\bar{T}\bar{\Lambda}^{\pm}\bar{T}^{-1}\right)\vec{Q} \tag{2.23}$$

here, $\bar{A}_{SW}^{\pm}$ stores the Stegar-Warming flux splitting Jacobian. Additionally, $\bar{T}$ and $\bar{T}^{-1}$ are the matrices of right eigenvectors and left eigenvectors of the Jacobian, respectively. The eigenvalue matrices are therefore defined as:

$$\bar{\Lambda}^{\pm} = \frac{1}{2}\left(\bar{\Lambda}_c \pm \left|\bar{\Lambda}_c\right|\right) \tag{2.24}$$

and the diagonal matrix, $\bar{\Lambda}_c$ is:

$$\bar{\Lambda}_c = \begin{bmatrix} \Lambda_1 & 0 & 0 & 0 \\ 0 & \Lambda_2 & 0 & 0 \\ 0 & 0 & \Lambda_3 & 0 \\ 0 & 0 & 0 & \Lambda_3 \end{bmatrix} \tag{2.25}$$

2.3.3 Roe Upwind Scheme. Roe's method is considered a flux-difference splitting scheme which approximately solves the Reimann (shock tube) problem by evaluating the left and right state at the face of a control volume [3]. Specifically, Roe's scheme reduces the convective flux difference, at a control volume face, into left and right running wave contributions. For a cell centered scheme, the flux difference is represented at the face of the cell centered control volume $(I + 1/2)$ [3]:

$$(\vec{F}_c)_{I+1/2} = \frac{1}{2}\left[\vec{F}_c(\vec{Q}_L) + \vec{F}_c(\vec{Q}_R) - \left|\bar{A}_{Roe}\right|_{I+1/2}(\vec{Q}_R - \vec{Q}_L)\right] \tag{2.26}$$

where L and R represent the left or right state and $\left|\bar{A}_{Roe}\right|$ is the diagonalized flux Jacobian or Roe matrix ($\bar{A}_{Roe} = \bar{T}\left|\bar{\Lambda}_c\right|\bar{T}^{-1}$), modified with Roe-averaged variables. Eq. 2.26 is only valid as long as the so called jump condition is satisfied [32]:

$$(\vec{F}_c)_R - (\vec{F}_c)_L = \bar{A}_{Roe}(\vec{Q}_R - \vec{Q}_L) \tag{2.27}$$

For the sake of brevity, the Roe-averaged variables themselves are not included in this discussion. Different approaches in presenting and applying the Roe-averaged variables are widely available; two such examples can be found in refs. [3, 32].

2.4 Turbulence Modeling

According to Blazek [3], "The outstanding feature of turbulent flow, in the opposite of laminar flow, is that molecules move in a chaotic fashion along complex irregular paths." Because of this, in a turbulent flow, higher values of friction drag and pressure drop will usually occur. Typically an energetic mixing of the flow among the different layers of the viscous layer takes place. Also, a turbulent boundary layer is able to maneuver through large regions of unfavorable pressure gradients, delaying separation much longer than a laminar boundary layer [30].

The unsteady Navier Stokes equations govern all turbulent flows in the flow continuum [30]. However, direct numerical simulation (DNS) of all the turbulent length scales, applied to a practical problem, is still not possible today because of the prohibitively high computing time required. The grid resolution required to resolve the smallest eddy scales and up to scales on the order of the computational domain would be $\propto Re^{9/4}$ leading to a required CPU time $\propto Re^3$ [3]. Therefore, an alternative approach is taken where turbulence models are developed which approximate or predict turbulent flow effects. Beyond DNS, there are two levels of turbulence model approximations. [3]:

1. The *Reynolds-Averaged Navier-Stokes equations (RANS)* are used to decompose the turbulent flow variables into mean and fluctuating components while implementing a time averaging. Because the turbulent parts of the flow are essentially averaged, a detailed turbulent structure is not obtainable. An additional term, the Reynolds-stress tensor, is introduced requiring a closure model of which there are two types.

- *second-order closure* models employ nonlinear and complex second order relationships to determine the Reynolds Stresses
- *first-order closure* models express the Reynolds stresses by determining the turbulent eddy viscosity based on the Boussinesq eddy viscosity hypothesis. The eddy viscosity is found by employing *algebraic* or zero-equation models, and *one- and two-equation* models. For the algebraic model, eddy viscosity is calculated from empirical relationships and history effects cannot be simulated. This generally results in poor prediction of massively separated flows. One- and two-equation models take history effects into account where the convection and diffusion terms are generated from transport equations for kinetic energy and turbulence dissipation [3].

2. *Large-Eddy Simulation (LES)* is a complex, computationally demanding model that attempts to resolve only large-scale eddies accurately and approximate the small scales. This is based on the idea that the more problem-dependant large eddies transfer the bulk of the momentum, while the smaller eddies are more uniform in their makeup and thus easier to estimate.

The nature of the current research requires the inclusion of a turbulence model in the flow solver. Highly separated flow is to be expected off the base of the cone shaped carrier vehicle and unsteady turbulent flow interactions exist during an aft store ejection. Beggar allows the use of the algebraic Baldwin-Lomax (B-L) turbulence model, the Spalart-Allmaras (S-A) one-equation model, and Detached-Eddy Simulation (DES) (where S-A is implemented as the RANS model). In his work, Simko [29] found that the S-A turbulence model on its own inadequately described the base pressure. Therefore, only the B-L turbulence model and the S-A turbulence model with DES will be used in this study.

2.4.1 Baldwin-Lomax. As mentioned in Section 2.4, the B-L turbulence model is an algebraic closure model to the RANS approach. It is somewhat simplified as compared to the other closure models in that it employs a series of emperical

relationships based on the velocity profile. Baldwin and Lomax use Prandtl's mixing length hypothesis and expand on their definition of eddy viscosity, μ_t, by dividing the turbulent boundary layer into an inner and outer region which are defined by the two parameters [17]:

$$\begin{aligned} u^+ &= \frac{u}{u_\tau} \\ y^+ &= \frac{\rho_w u_\tau y}{\mu_w} \end{aligned} \tag{2.28}$$

in which u_τ is the friction velocity,

$$u_\tau = \sqrt{\frac{\tau_w}{\rho_w}} \tag{2.29}$$

In the above three equations, w signifies conditions on the wall and y is physical distance from the wall. Recall that the B-L model employs a two region strategy to modeling the turbulent flow structure. The inner region is given by:

$$(\mu_t)_{inner} = \rho L^w{}_m \, |\Omega| \tag{2.30}$$

where the fluid vorticity Ω is given by:

$$|\Omega| = \sqrt{\left(\frac{\partial v}{\partial x} - \frac{\partial u}{\partial y}\right)^2 + \left(\frac{\partial w}{\partial y} - \frac{\partial v}{\partial z}\right)^2 + \left(\frac{\partial u}{\partial z} - \frac{\partial w}{\partial x}\right)^2} \tag{2.31}$$

The eddy viscosity for the outer region, $(\mu_t)_{outer}$, is more complicated and presented below [30]:

$$(\mu_t)_{outer} = 0.0168 \rho V_{t0} L_0 \tag{2.32}$$

where:

$$V_{t0} = min(F_{max}, 0.25 {q^2}_{Diff}/F_{max})$$

$${q^2}_{Diff} = \left(u^2 + v^2 + w^2\right)_{max} - \left(u^2 + v^2 + w^2\right)_{min}$$

$$F_{max} = max\left[y\left|\omega\right|\left(1 - e^{-(y^+/A^+)}\right)\right]$$

$$L_0 = 1.6 y_{max} I^k$$

$$I^k = \left[1 + 5.5\left(\frac{0.3y}{y_{max}}\right)^6\right]^{-1}$$

in which $y_{max} = y$ at F_{max}.

The B-L turbulence model is generally considered critically deficient when it comes to modeling details of massively separated flows like the base flow on a supersonic projectile, as it relates to this research. Nonetheless, for numerous computational investigations into base flow, the B-L model was found to be adequate at determining general flow characteristics of the near wake and upstream conditions for a base flow environment [18, 19, 27, 34]. Furthermore, Simko [29] found that the B-L model, as implemented in Beggar, resulted in base pressures closely matching analytical and empirical data. Therefore, for the purposes of this study, the B-L turbulence model should provide a sufficient computational picture of the events surrounding a supersonic ejection aft into a base wake. If any detailed features of the unsteady recirculation region are to be resolved, a more accurate turbulence model is required.

2.4.2 Spalart-Allmaras. The Spalarat-Allmaras model adds the parameter $\tilde{\nu}$ in order to obtain closure to the RANS equations and approximate the Reynolds stresses. This turbulence variable is essentially proportional to the turbulent kinematic viscosity given as $\nu_T = \tilde{\nu} f_{\nu 1}$. $\tilde{\nu}$ is obtained from the solution to the transport

equation [30]:

$$\frac{\partial \tilde{\nu}}{\partial t} + u_j \frac{\partial \tilde{\nu}}{\partial x_j} = \frac{1}{\sigma} \frac{\partial}{\partial x_k} \left[(\nu + \tilde{\nu}) \frac{\partial \tilde{\nu}}{\partial x_k} \right] + c_{b1} (1 - f_{\nu 2}) \tilde{S} \tilde{\nu} - c_{w1} f_w \left(\frac{\tilde{\nu}}{d} \right)^2 + \frac{c_{b2}}{\sigma} \frac{\partial \tilde{\nu}}{\partial x_k} \frac{\partial \tilde{\nu}}{\partial x_k} \tag{2.33}$$

where:

$$\begin{aligned}
c_{b1} &= 0.1355 & c_{b2} &= 0.622 \\
c_{\nu 1} &= 7.1 & \sigma &= 2/3 \\
c_{w3} &= 2 & \kappa &= 0.41 \\
c_{w2} &= 0.3 & c_{w1} &= \tfrac{c_{b1}}{\kappa^2} + \tfrac{(1+c_{b2})}{\sigma} \\
f_{\nu 1} &= \frac{X^3}{X^3 + {c^3}_{\nu 1}} & f_{\nu 2} &= 1 - \tfrac{X}{1+X f_{\nu 1}} \\
f_w &= g \left(\frac{1 + {c^6}_{w3}}{g^6 + {c^6}_{w3}} \right) & X &= \tfrac{\tilde{\nu}}{\nu} \\
g &= r + c_{w2} \left(r^6 - r \right) & r &= \tfrac{\tilde{n}u}{\tilde{S} \kappa^2 d^2} \\
\tilde{S} &= S + \frac{\tilde{\nu}}{\kappa^2 d^2} f_{\nu 2} & S &= \sqrt{2 \Omega_{ij} \Omega_{ij}} \\
\Omega_{ij} &= \frac{1}{2} \left(\frac{\partial u_i}{\partial x_j} - \frac{\partial u_j}{\partial x_i} \right)
\end{aligned}$$

and d is the distance from the closest wall. Take note that the second term on the right hand side of Eq. 2.33 represents eddy production and the third term immediately following controls eddy viscosity destruction. The first term on the right is turbulent and viscous diffusion, while the last term models the laminar to turbulent transition [3]. The S-A model is a favorite turbulence model for many due to its robustness and quick convergence. In addition, high grid resolution near the wall is not critical to accurately define the boundary layer. Simko [29] applied the S-A turbulence model to his base flow research (using Beggar) and found the base pressure prediction to be so poor that he discontinued using it. However, when applied to a hybrid RANS/LES turbulence modeling method known as Detached Eddy Simulation (DES), much better

results were realized. For that reason, DES is being used in the current research as well.

2.4.3 Detached Eddy Simulation. As touched on earlier in Section 2.4, LES attempts to directly compute the contribution of the large eddy structures in the flow, and model the effects of the smaller turbulent structures. This is based on the idea that the larger eddies dictate the bulk of the turbulent flow character due to their high energy and momentum transfer. Unfortunately, this is still a computationally intensive task requiring a highly refined grid. To reduce computer clock time, Spalart proposed that the RANS method be mated with the LES model and called it Detached Eddy Simulation or DES. This is advantageous in that the RANS turbulence model can be used to capture the attached boundary layer, dramatically reducing the number of cells that LES would have required, allowing LES to be used only on regions away from the wall. To do this, a switch is implemented in the RANS turbulent model, which seamlessly changes turbulence model methods depending on grid density. In the case of this research, the wall distance variable d (Eq. 2.33) is modified in the S-A RANS model by substituting it with the length scale l [3] where:

$$\begin{aligned} l &= min\left(d, C_{DES}\Delta\right) \\ \Delta &= max\left(\Delta x, \Delta y, \Delta z\right) \end{aligned} \tag{2.34}$$

where C_{DES} is a constant dependant on the flow type (for this work it is set to 0.65). This relationship acts to trigger the RANS model in the highly asentropic region of the boundary layer by setting $l = d$. As a grid point moves far enough away from the wall such that $d \leq C_{DES}\Delta$, the LES model is triggered. It is important to note that effective use of the DES model requires a well designed grid, with refined isentropic spacing in *all* directions in regions where LES is desired.

2.5 Beggar Grid Assembly

2.5.1 Grid Heirarchy. Beggar allows two ways to define its structured grid system: the superblock and dynamic group [26]. The superblock is defined as an assemblage of non-overlapping grid blocks holding similar boundary faces. With point matched faces, it is possible to directly pass flow variables between grids within the same superblock. Typically, the major components of a system are managed by superblocks, i.e. for this project, one superblock is used for the carrier body and a different superblock is assigned to the internally carried store.

Dynamic groups in Beggar provide a way to link multiple superblocks together to define a rigid body for a dynamic motion analysis [26]. Dynamic groups point to force specification statements which provide reference quantities for the bodies of interest. Inertial properties and external forces can be applied to each superblock in the dynamic group and dynamic data can be dumped at varying time steps. This way, any number of superblocks will behave as a single system according to user inputs, creating an efficient and user friendly computational environment.

2.5.2 Grid Communication. Beggar's different methods of grid communication were introduced in Section 1.3. The three methods discussed include block-to-block, patched, and overlapping and a simplified depiction of the grids was given in Figure 1.1. These will be covered in more detail here.

Block-to-block communication takes place across the boundary faces of the grids making up a superblock. By Beggar's definition, a block-to-block boundary is one where identical (x, y, z) Cartesian coordinates meet to define two separate grid cell faces. Block-to-block boundaries can occur within single grids or across separate grid faces. Care must be taken to avoid point mismatches with a block-to-block boundary because boundary detection could fail, resulting in undesired computational results or incorrect grid assembly. In many instances, block-to-block boundaries are incorrectly identified because the user-defined tolerance which tells Beggar whether or not two points are close enough to be coincident is too large. This occurs especially

in boundary layer regions and near existing singularities where closely related points are incorrectly pulled together [31].

Patched communication also takes place across the boundary faces of grids in superblocks. It differs from the block-to-block communication by not requiring coincident points and matching cell faces. It can be especially helpful in 'patching' failed block-to-block boundaries, maintaining grid-grid communication. Beggar uses phantom (ghost) cells in the patched grid to interpolate flow values to the connecting grid. Interestingly, singularities (a collapsed cell face) are treated as patched communication requiring a ghost cell for accurate cross-boundary information transfer. If interpolation fails, the singularity will not communicate any information across the boundary [31]

As stated in Section 1.3, Beggar makes use of overlapping grids as well. This type of grid communication only takes place between superblocks. Information is passed, utilizing interpolation algorithms, from one grid to another grid throughout the overlap regions. This process, also referred to as the Chimera technique, is completely automated in Beggar and provides the only practical way to simulate dynamic store ejections or other movement. Cells within a solid object or otherwise outside the computational domain are removed through a process called 'hole-cutting' or 'blanking'.

Correct solution interpolation across grid boundaries is critical. There must be an appropriate number of interpolation sources in the grid overlap regions in order for a dynamic store separation to be successful. These regions are also referred to as interpolation fringes. Figure 2.7 illustrates a typical interpolation stencil for a second order inviscid and viscous solution domain. Beggar goes through a complex vetting process in order to determine the best interpolation source for a given fringe cell during a grid assembly. If an appropriate interpolation stencil cannot be found, the code iterates until all overlap cells are correctly interpolated or until it reaches a user specified maximum iteration count, in which case the grid assembly fails. In

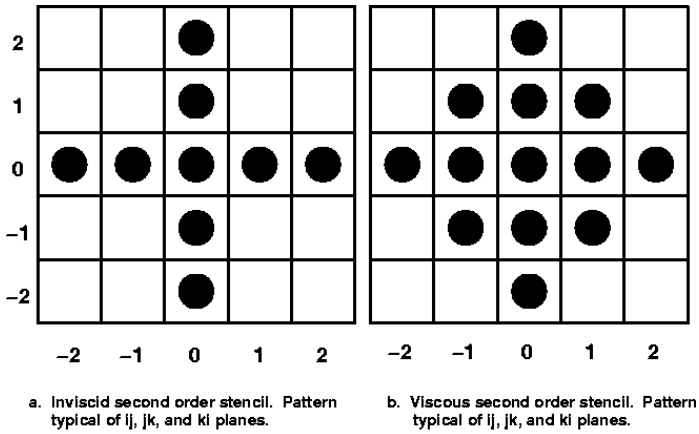

Figure 2.7: Flow Solver Stencils [31]

order to increase the stability of the code, so-called orphan points can be assigned to cells in the overlap region that are unable to find interpolation sources during the grid assembly process. After the orphan points are identified and directly following grid assembly, Beggar will assign them a valid, weighted flow field value. The flow field on all grids is then solved for and grid communications resume [31].

2.6 (6+)DOF Model

Beggar is unique in that a (6+)DOF model is integrated into the grid assembly and flow solver code. In order to correctly apply the (6+)DOF model, four operations are performed in order [25]:

1. Grid assembly
2. Solve flow governing equations
3. Determine forces and moments on the body by integrating pressure and viscous stresses
4. Solve dynamic equations of motion for body

This creates a powerful, all in one computational tool capable of solving virtually any store separation problem. The (6+)DOF model is labeled such (as opposed to 6-DOF) because in addition to solving the rigid body dynamic equations of motion,

it also solves the equations of motion for moving components on the rigid body itself. Beggar generally refers to the rigid store body as SB (store body) and the moving store body component as SMC (store moving component). For the purposes of this research, only the 6-DOF portion of the code is necessary because there are no moving components on the carrier or internally carried store. This results in a simplified expression of the equations of motion for a rigid body [26] applied to the carrier and store individually:

$$m^c \frac{d^I}{dt} v_s = F^s_{appl} \tag{2.35}$$

$$\frac{d^I}{dt}\left(I^s{}_s \omega^S\right) = N^S_{S(appl)} \tag{2.36}$$

where the velocity and angular velocity are found in the two above equations respectively. F^s_{appl} is the applied force on the SB and $N^S_{S(appl)}$ is the moment applied force on the SB. Both F^s_{appl} and $N^S_{S(appl)}$ can result from any combination of user designated forces, gravitional forces, and aerodynamic forces. The center of mass of the SB is m_c and d^I/dt is the time derivate relative to the chosen intertial reference frame. Finally, ω^S is the angular velocity of the SB and v_S is the velocity of the SB from which the trajectory x_S of the body of interest can be determined [25]:

$$\frac{d^I}{dt} x_S = v_s \tag{2.37}$$

Beggar uses a conventional CFD coordinate system where the nose of the store is located at the origin and the x-axis runs positively fore to aft with positive flow in the x-direction. The coordinate system of any given SB or SMB superblock is initially read in to Beggar using it's global coordinate system. If no translational, rotational or scaling commands are issued, a given superblock(s) keeps that coordinate system. However, if a superblock is altered in any of the aforementioned ways, a transformation matrix is used to reposition the superblock appropriately. This does not actually change the grid's coordinate system itself but instead acts to place the

superblock relative to a reference global coordinate system. These transformation matrices are preserved for every superblock added to a solution domain. During a body's movement, it's own unique transformation matrix is updated relative to the global coordinate system thus preserving the grids own local coordinates. The creation of the transformation matrix is documented fully in [2]. With the coordinate system defined, SB orientation can be determined. Beggar achieves this by forming it's three-dimensional rotation in terms of quaternians. A quaternion consist of one real and three imaginary parts. They are often used to find rotational transforms by essentially creating a four-dimensional space to calculate three dimensional rotations. There is a scalar part, Q_S and vector part $\vec{Q}_v$ of the quaternion which governs the SB's orientation, given as [25]:

$$\frac{d}{dt} Q_S = -\frac{1}{2} \vec{Q}_v \cdot \omega^8 \tag{2.38}$$

$$\frac{d^I}{dt} \vec{Q}_v = \frac{1}{2} Q_S \omega^8 + \frac{1}{2} \omega^8 \times \vec{Q}_v \tag{2.39}$$

The coordinate transformation, mentioned above, that relates the global coordinate system to the SB's own local coordinate system is also computed in terms of the quaternion. All the governing equations for motion and orientation can be assembled into a set of ordinary differential equations with the following form [26]:

$$\frac{d}{dt} \vec{y} = f\,(y, t) \tag{2.40}$$

where $\vec{y}$ contains all the dependant variables of the problem. A fourth order Runge-Kutte scheme is used to solve the above ordinary differential equations [25].

2.7 Stability and Inertial Properties

Beggar requires inertial properties, including center of gravity, for any body undergoing a dynamic store separation. Since all bodies of interest are symmetrical, only longitudinal stability values are required. For a sphere-cone RV, the center of

pressure (x_{CP}) can be determined using Newtonian approximation [23]:

$$\frac{x_{CP}}{x_L} = \frac{2}{3}\left(sec^2\left(\alpha_c\right)\right) \tag{2.41}$$

where α_c is the cone half angle and x_L is the cone body length along the x-axis. The static margin (SM)for a symmetrically shaped RV can be found as the distance between the x_{CP} and it's center of gravity in the x-direction (x_{CG}):

$$SM = 100\%\frac{x_{CP} - x_{CG}}{x_L} \tag{2.42}$$

A positive static margin means that the vehicle has a positive static stability. This implies that a vehicle subjected to a disturbance will respond with an aerodynamic moment that acts to bring the AOA back to a pre-disturbance setting. For an RV, positive static stability is a desirable vehicle stability and control property. An SM of 10% provides suitably positive static stability for an RV [1] and was applied against the carrier body and payload.

Lastly, the moments of inertia for each body are required. These can be found through the empirical approximation of the moments of inertia for a sphere-cone shaped re-entry vehicle, provided by [1]:

$$I_{xx} = 0.057 \cdot m \cdot 4.0 \cdot r^2 \tag{2.43}$$

$$I_{yy} = I_{zz} = \left(0.131071 \cdot m \cdot 4.0 \cdot r_b^2\right) + \left(0.064124 \cdot m \cdot l^2\right) \tag{2.44}$$

where I_{xx} is the roll moment of inertia and I_{zz} and I_{yy} are moments of inertia in the pitch and yaw direction. They are identical because the body is symmetric. m is the mass of the body in kilograms, r_b is the RV's base radius in meters, and l is the body's length in meters. With a symmetric body in this coordinate reference frame, only the product of inertia in the non-symmetric xy plane I_{xy} exists, the other product of inertia's around the xz and yx plane will be zero. For this problem, it's contribution to overall inertial stability is neglected.

III. Methodology

3.1 Geometry

The size, shape, and mass of the carrier vehicle was chosen such that it would represent a real-life, generic, sphere-cone shaped re-entry vehicle. In contrast, the store itself does not represent a particular munitions or payload, but is essentially a smaller shaped version of the carrier vehicle. The relative size and shape of the computational models are presented in Figure 3.1 where the carrier vehicle is semi-transparent to better illustrate it's base cavity. The isometric view of the two bodies in Figure 3.1 takes place at a separation distance of two carrier base diameters or 2 meters (6.56 ft).

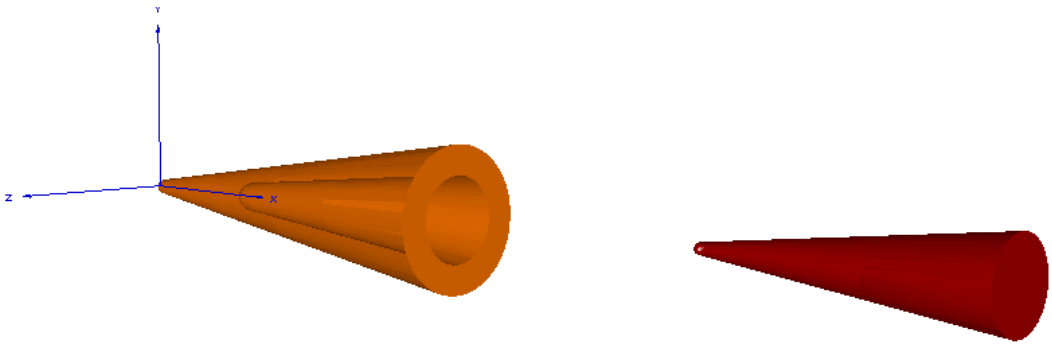

Figure 3.1: Carrier Shell with Store Deployed Aft

Dimensional data and mass properties were chosen based on guidance from an expert in the field of re-entry vehicle dynamics [1]. From those discussions, the geometry for a typical re-entry vehicle was developed. This resulted in a sphere-cone shaped carrier body with a 0.05 m (0.164 ft) radius nose tip and a 1 m (3.280 ft) base diameter. The similarly shaped store was designed with a nose tip radius of 0.0375 m (.123 ft) and a 0.575 m (1.886 ft) base diameter. The cavity of the carrier vehicle is 2.2 m (7.218 ft) long to accommodate the 2.175 m (7.136 ft) long store. The carrier vehicle and store have half-cone angles of 8.9° and 7.5° respectively. Drawings of the carrier vehicle and store are provided in Figure 3.2 on the x-y plane where x

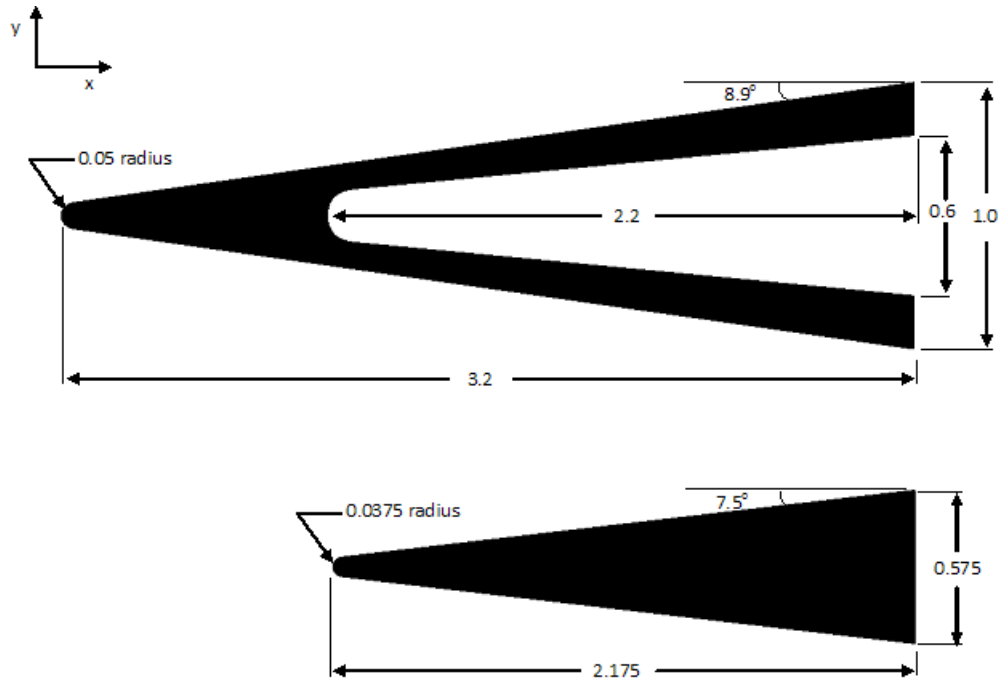

Figure 3.2: Dimensional Drawing of Carrier Shell and Store

runs positive fore-to-aft along the body. All units are stated in terms of the carrier vehicle's base diameter. The carrier shell's mass is set to 350 kg (770 lb) while the store's mass is 450 kg (990 lb). This creates a realistic mass ratio of payload to carrier for an RV [1].

3.2 Grid Topology

Two separate computational grid systems were created such that flow solutions and individual body's trajectories could be captured entirely. The initial solution domain used is pictured in Figure 3.3 and includes three superblocks that define the solution domain of the carrier and store body. Each superblock is likewise composed of multiple grids or blocks themselves. This configuration was used only where the carrier and stowed store system were initialized, before separation, at zero or low AOA's ($\leq 2°$). In Figure 3.3, the green grid defining the carrier is the global grid for the system and the store grid in blue is embedded in the carrier along with an interface grid shown in yellow. There are 4.4 million cells in the carrier body superblock, which

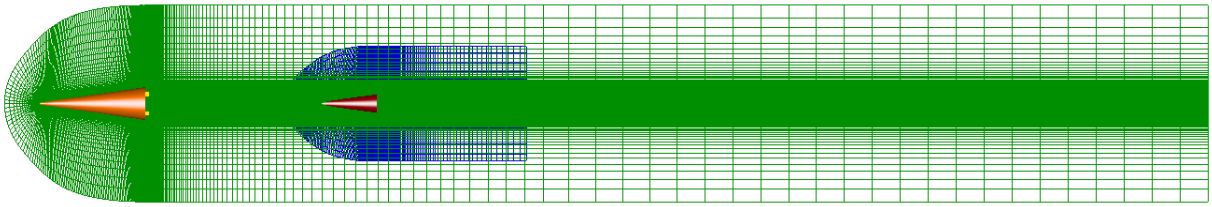

Figure 3.3: Computational Domain of Carrier and Store: Low AOA Cases

is stretched aft past the body base 25 base diameters. This was done so that a given store separation event would be captured in its entirety. The store superblock is composed of 2.65 million cells, and stretches aft 4 base diameters. The size of the store's domain is not as important, since it stays within the global grid for the complete store ejection simulation.

The second solution domain, pictured in Figure 3.4, is significantly larger and allows for the additional rotation and movement associated with a high AOA separation event. Four superblocks are used to define the computational domain. This domain is simply an augmented version of the low AOA case grid discussed in the previous paragraph. In both cases the goal is to fully capture all shock and wake interaction between the leading and trailing bodies. Once again, the green grid built around the carrier body is the global or background grid for the system and it has 4.76 million cells. The store grid in blue consists of 3.36 million cells and an additional overset grid (in pink) acting to refine the aft region of the carrier grid consists of 268,000 cells. The interface grid remained unchanged from the baseline grid shown in Figure 3.3.

Grids on each body were created using *Gridgen*®. The body grids were extruded 360°, at 90° intervals around the x-axis (axis of symmetry). To capture the viscous turbulent boundary layer with the RANS turbulence model, an initial grid spacing of 3×10^{-6} at $y+ < 1$ was generated on both bodies. *Gridgen's*® hyperbolic solver was used to grow the cell-structured boundary layer out from the forward wall boundaries to far-field conditions. A growth rate of 1.2 was implemented through the first 15 cells, at which point a constant spacing was maintained through 10 additional cells. Once

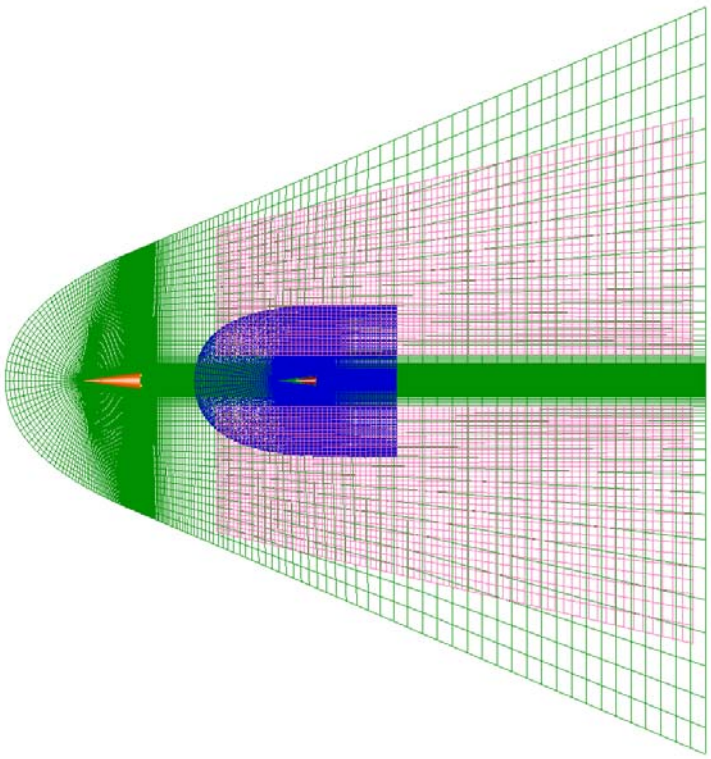

Figure 3.4: Computational Domain of Carrier and Store: High AOA Cases

the boundary layer had been captured appropriately, a growth rate of 1.5 continued until the desired solution domain size was reached. In order to reduce computational time, the grid spacing at the base of both the store and carrier was not designed to specifically capture the turbulent boundary layer. As it has already been discussed, this is an extremely low velocity recirculation region, and a refined boundary layer on the base would have very little impact on the overall computational solution.

The interface grid is small relative to the body grids and difficult to see in Figures 3.3 and 3.4. A close up view in Figure 3.5 shows the interface grid located at the base face of the carrier when the store is stowed within the carrier body's cavity. This is a key transitional location in the computational domain where several block-to-block boundaries meet within each superblock, in addition to overlapping boundaries between superblocks. The interface grid is extremely dense at 1.2 million

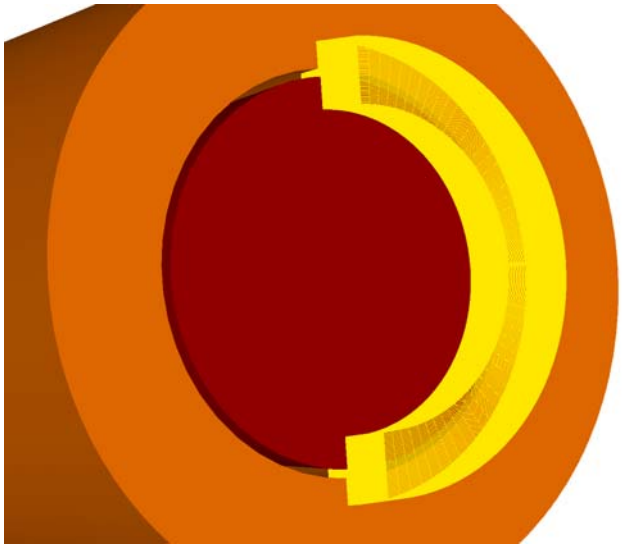

Figure 3.5: Carrier Cavity and Store Gap with Interface Grid

cells in size and sustains an adequate interpolation region at the faces of the carrier and store base, aiding the grid assembly process.

When the store is located within the carrier cavity, there must be enough cells overlapping to allow communication throughout the static solution and into the dynamic solution. A 0.0125 meter gap between the store wall and the inner cavity wall at the base face is employed to maintain communication between superblocks. See Figure 3.5 for a close up view of the gap existing between the store body and carrier cavity at the base.

3.3 Computational Approach

The static solution for the two body system must be determined first before any dynamic problems can be determined. In all initial solutions, the store is positioned inside the carrier cavity such that its base extends past the base of the carrier 5 mm (.197 inches). A minimum .0125 m gap between the two body's bases at the cavity face exists to allow for interpolation during motion. Time accuracy is not required for a steady state type solution. Therefore, ramped local time stepping was used starting at a non-dimensional time step (dt) of 1×10^{-4}, gradually increasing to a final dt of

10.0 (3.40×10^{-2} seconds of physical time) by the 1,000th iteration. Flow conditions included a free stream Mach number of 2.90 and Reynolds number of $6.9X \times 0^6$/m which is referenced to the carrier body's base diameter. No-slip boundary conditions were gradually applied to the wall boundaries through the first 20 iterations to allow the flow to be turned gradually. Additionally, pre-initialization of the flow field in and around the base region and carrier cavity to Mach 0.25 was of critical importance. Without initializing the flow in those regions to a low subsonic Mach number, high speed flow tended to 'leak' out of the carrier cavity and into the near wake region causing solution divergence.

For the next phase, dynamic calculations were started from the static solution. The 6-DOF solver was called to run 600 to 1,300 time-accurate iterations using a non-dimensional dt of 0.25 (8.475×10^{-4} seconds of physical time) for a total physical time of 0.60 to 1.10 seconds. Five Newton sub-iterations were computed at each time step to accurately measure the unsteady flow characteristics. Recall from Section 2.6 that as motion is called for each time step, the superblocks move appropriately as rigid bodies. Once the grids have moved relative to each other, the flow solution must be interpolated across the overlapping boundaries. The flow solver is then used to compute the flow solution at another time step - repeating this process until the maximum number of iterations is reached. Time can be saved here by forcing grid assembly to take place at evenly spaced time intervals during the simulation. However, this can make the solution less stable. In the current effort, grid assembly was initiated every time step along with output of the intermediate flow solution at that point in time.

Orphan cells were required mostly during approximately the first 20 iterations of motion and periodically throughout each simulation. Orphan cells are described in detail in Section 2.5.2. In this case, the maximum number of orphans claimed at any one time step, made up less than 0.5% of the total number of grid cells in the multi-superblock system. As the two bodies initially move past each other during the 6-DOF simulations, a maximum number of orphan cells were required. As the store

gains separation distance from the carrier shell ($\approx$ .01 m), the number of orphan cells quickly drops off to zero, occasionally requiring a few orphan cells toward the end of the simulation. Relative to the number of cells in the two body system, there were very few orphan cells used at any one time step resulting in virtually no impact on the accuracy of the overall solution.

3.4 Separation Simulation Test Matrix

Because of the long computing times required, the scope of the problem was narrowed to two specific cases. Table 3.1 provides the simulation test matrix for an AOA (α) sweep with dynamic store ejection simulations taking place at every AOA. In these cases, the effort is aimed at determining quantifiable aerodynamic forces on the bodies for a given ejection force and AOA using the B-L turbulence model. The contribution of gravity is neglected in the AOA sweeps so that only the aerodynamic forces contribute to the solution.

Table 3.1: Separation Test Matrix for AOA Sweep

	B-L	
AOA	Mach	Re/l
0°		
2°		
4°	2.9	6.9×10^6
6°		
8°		

Table 3.2 gives the investigation schedule for the second of the two targeted cases. Here, the flight path angle (γ), or body orientation, is adjusted by altering the gravity vector on the vehicle. A 0° flight path angle means the body is on a level flight path relative to the horizon, whereas a 90° flight path angle puts the RV vertical relative to the horizon. The B-L turbulence model was used in this set of data runs as well.

Table 3.2: Separation Test Matrix for Flight Angle Sweep

	B-L	
Flight Path Angle	Mach	Re/l
0°	2.9	$6.9X10^6$
30°		
60°		
90°		

As stated earlier, the store separation simulations were developed with the store body face initially extended slightly past the face of the carrier body a distance of 5 mm (positive x direction). When the carrier base face and the store base face sat flush to each other, the flow solution with motion developed far too many orphan cells causing solution divergence and failure. The 5 mm store base face offset succeeds in allowing the separation simulation to be completed without failure. Therefore, all comparison data for the AOA sweeps are generated from the initial 5 mm store base offset.

3.5 Coordinate System and Aerodynamic Coefficients

Beggar outputs multiple formats of body trajectory and angular position history files, as well as force and moment tracking data on a given body for the duration of a separation simulation. The reference coordinate system is under limited control by the user and all data output is relative to the initial state (orientation, speed, etc.) of the body or bodies referenced against that particular coordinate system and in dimensional reference units. The standard CFD coordinate system shown in Figure 3.1 (where x is positive fore to aft, y is positive up, and z is positive out the left hand side) was used in all calculations and results. Therefore, in discussing and defining the trajectory and orientation of the carrier and store bodies, the following convention will be used:

- positive pitch or pitch up in degrees = $-\theta$
- positive yaw in degrees = $-\psi$

- positive roll in degrees = $-\phi$

where θ, ψ, and ϕ are the angular displacements about the z, x, and y axis respectively in the CFD coordinate system.

Likewise, all force and moment data to be presented in Chapter IV are determined in the global reference frame within the standard CFD coordinate system. Body force and moment coefficients are non-dimensialized as follows:

$$C_F = F\frac{2}{M_\infty^2 A_{ref}} \tag{3.1}$$

$$C_M = M\frac{2}{M_\infty^2 A_{ref} L_{ref}} \tag{3.2}$$

where F is the force and M is the moment, L is the body length and M_∞ is the free stream Mach number.

Almost all tabular and plotted data will reference the separation distance between the carrier and store vehicle as a way to track and measure the progress of the separation simulations. For the purposes of this study, the separation distance (x/D) is defined as the distance in carrier base diameters between the base face of the store and the base face of the carrier as shown in Figure 3.6.

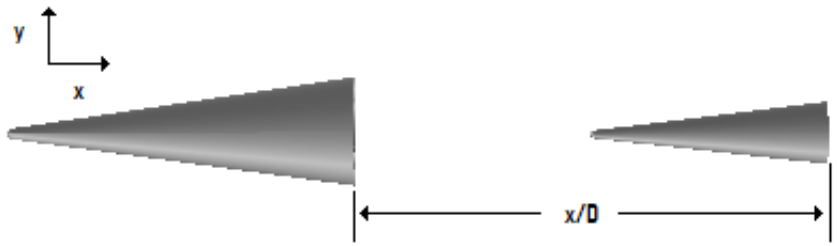

Figure 3.6: Separation Distance (x/D)

3.6 Computational Requirements

AFIT's High Performance Computing environment was utilized in determining all static and dynamic solutions. Static solutions required anywhere from 6,000 it-

erations to 10,000 iterations to reach convergence. Convergence was determined by monitoring the stabilization of forces and moments on the carrier shell and store. Dynamic separation simulations were computed out to a fixed 1,300 iterations for all the cases mentioned in Tables 1 and 2.

Both static and dynamic jobs were submitted in parallel to ten 2.2GHZ processors, with 4GB of memory per CPU, via Portable Batch System (PBS) located on the high performance computing server. A wall time ranging from 65 hrs to 100 hrs for 6,000 to 10,000 iterations respectively, was realized. Accordingly, CPU time for the static solutions ended up at 650 hrs to 1,000 hrs. The store separation simulations had significantly longer runtimes due to a variety of reasons including the small time-steps, additional Newton sub-iterations at every time-step, and required assembly and grid interpolation at every time step. Wall times up to 120 hrs with CPU times of 1,200 hrs were required.

3.7 Beggar Input Files

The main input file for Beggar consists of multiple components inputs which can be include within the main input file itself or used as individual files that are called by the main input file. Core inputs to the main input file include solver initialization parameters and flow properties. Force specifications and dynamic specification need to be created for each moving body in order to obtain integrated body forces and trajectory data for the given separation simulation. In this case, grid definitions are created separately and called by the main input file. Appendix B provides a sample set of static and dynamic input files along with the associated grid definitions.

IV. Results and Discussion

Recall from Section 3.4 that two baseline investigations were developed: a gravity sweep or flight angle (γ) sweep from 0° to 90° and an AOA (α) sweep from 0° to 8°. Results and discussion for both cases are presented later in this section. An examination of specialized cases and flow conditions including failed separation simulations, static DES base flow results, static and dynamic derivations of body drag coefficients, and an alternative store stowage configuration is also provided. Note that a tremendous amount of data has been generated for this discussion. Much of that information has been placed in Appendix A for additional reference.

4.1 Static/Dynamic Body Drag Analysis

A comparison of the resultant dynamic solutions to static solutions at fixed separation distances (x/D) for both the carrier and store was initially carried out in order to examine differences that might exist between the two solution types. Of particular interest is the effect that the dynamic separation solution will have on drag of the two bodies compared to a static solution where the store and carrier are evaluated at fixed distances from one another.

Figure 4.1 compares C_D for the carrier and store at separation distances of x/D = 2, 4, and 6 for static and dynamic solutions. The static/dynamic systems were subjected to 15G ejection load at a free stream Mach number of 2.9 and $\alpha = 0°$, at a $\mathrm{Re}/l = 6.9 \times 10^6$. The colored squares represent static and dynamic solutions for the carrier body and the colored triangles represent static and dynamic solutions for the store body. For the static solutions, all C_D data was averaged over the last 200 iterations of the solution.

Upon examination of Figure 4.1, it can be seen that there is a notable difference between the static and dynamic runs, for both carrier and store. The static solutions at all three x/D locations is over-predicting the drag as compared to the dynamic solutions. At x/D = 2, the static C_D for the carrier is 9% greater and the static solution for the store is 122% greater than the dynamic solution.At x/D = 4, the

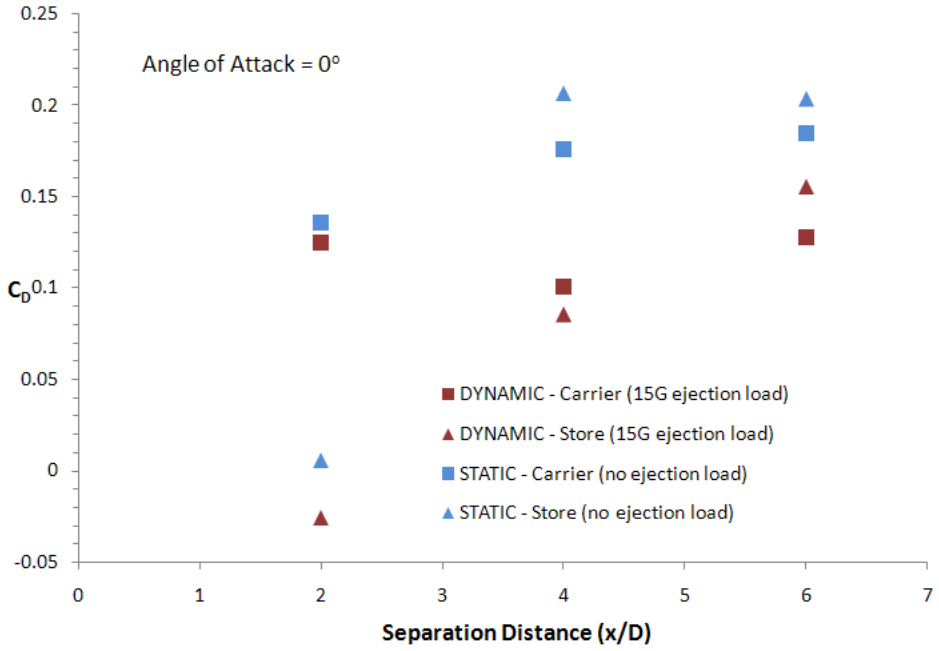

Figure 4.1: Drag Coefficient of Static Solutions Compared to Dynamic Solutions

static C_D for the carrier is 74% greater and the static solution for the store is 141% greater than the dynamic solution. At x/D=6, the static C_D for the carrier is 44% greater and the static solution for the store is 30% greater than the dynamic solution. The noted disparity in drag between static and dynamic cases is consistent with previous research results provided in Figure 2.6(a).

Both types of store drag solutions exhibit similar behavior, with the store drag gradually increasing as x/D increases. The carrier drag for the two solution types trend somewhat differently, with the dynamic solution showing a dip in drag at x/D = 4, while the static solution has carrier drag always increasing relative to separation distance.

At x/D = 4, the static solution displays unrealistic results, with the store experiencing higher drag than the carrier body. At x/D = 6, both systems appear to have computed this unrealistic C_D, where store drag has increased higher than the carrier drag. Simko [29] experienced similar results in his work and attributed it to the inability of the B-L turbulence model to accurately model separated flows, effec-

tively washing out the wake. Possibly the store could reach drag values equivalent to the carrier from a dynamic solution if it were slipping out of the wake environment of the carrier body. This is not likely, however, as shown in Sections 4.2 and 4.3.1, where at a release of zero incidence to the free-stream, the store remains quite stable in the wake and tends to remain there.

Finally, note that no 'suction' effect, or negative C_D, is computed for the store using the static solution. In contrast, the dynamic solution is portraying the expected suction as the store is drawn back to the carrier while submerged within in its low drag, near wake region. The inability of the static method to distinguish the negative drag or suction forces on the store at close proximity to the carrier points to inherent differences in the flow field of the dynamic system as compared to that of the static system.

Disparities in drag between the static and dynamic solutions are largely due to differences between the base pressure of the bodies, which in turn is related to the computed strength of the expansion region for the carrier and store respectively. Recall from Section 2.1.1 that the size of the recirculation region directly affects the base pressure and therefore body drag. This is visualized in Figures 4.2 - 4.4 where contours of Mach for the three separation cases comparing static solutions to dynamic solutions are provided. The sharper expansion angle in the static solutions and larger recirculation region in the dynamic solutions specifically at x/D = 4 and 6 is readily visible.

With the larger wake and recirculation regions in the x/D = 4 and x/D = 6 cases, it would follow that the dynamic system is predicting weaker expansions at the base of both store and carrier, than the static system. This is shown to be true in Figures 4.5 - 4.6 where C_P, passing through the expansion fan, is plotted at a given Y-distance from the symmetry line for the different separation distances (C_P data was extracted at a point just aft of both the carrier and store base faces for x/D = 4 and x/D = 6, and just aft of the store base face for x/D = 2).

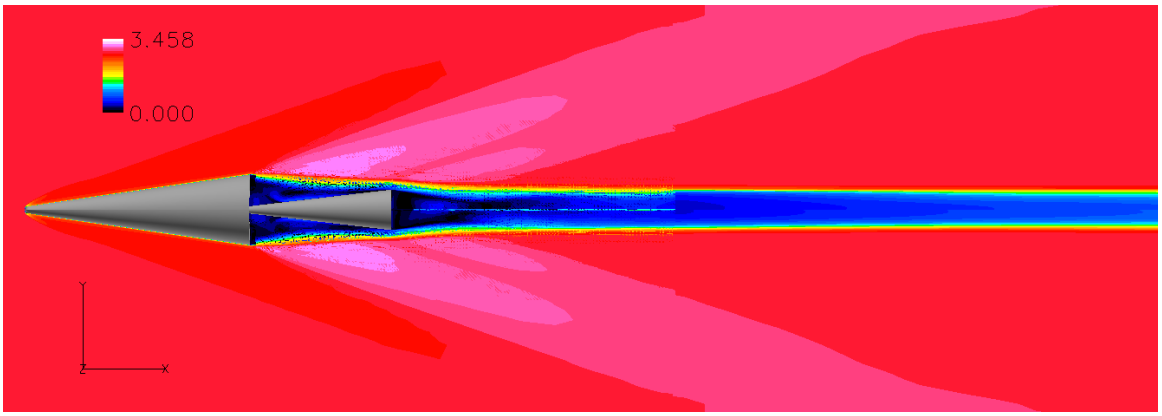

(a) Static Solution at x/D = 2

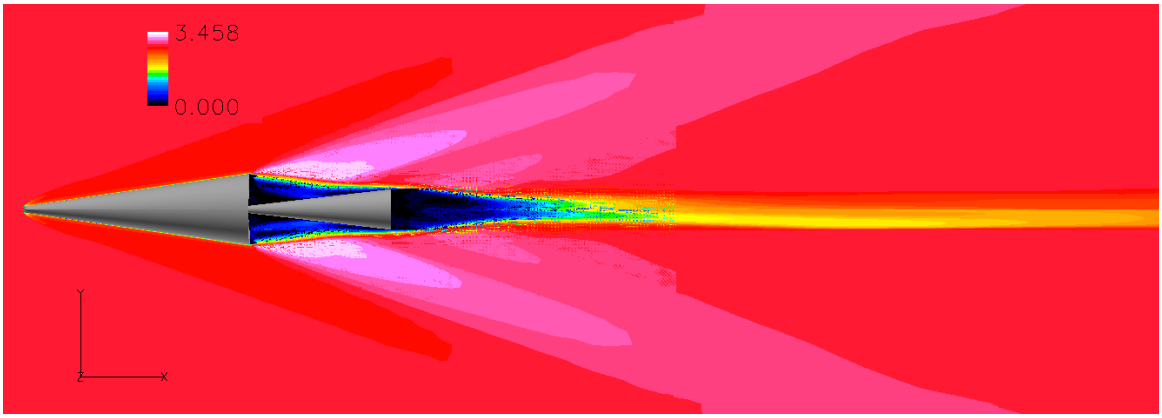

(b) Dynamic Solution at x/D = 2 (15G Ejection Load)

Figure 4.2: Contours of Mach for Static/Dynamic Solution at x/D = 2

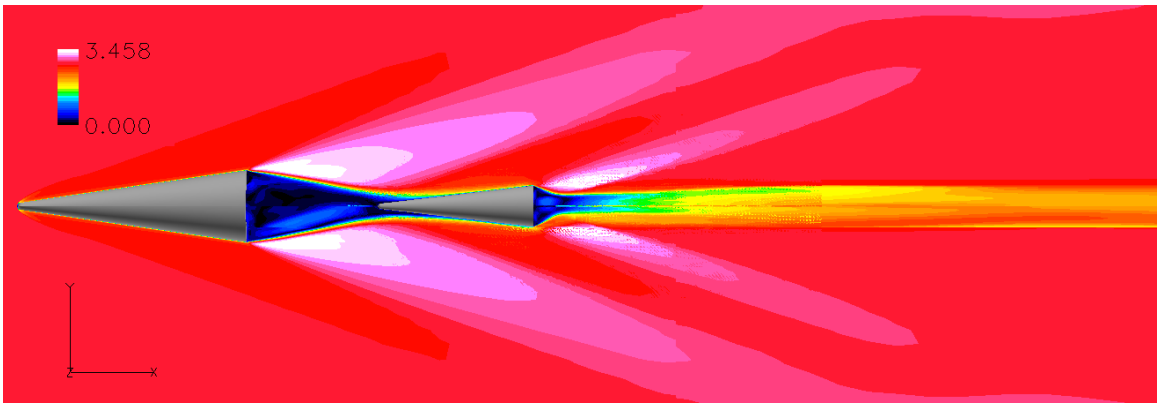

(a) Static Solution at x/D = 4

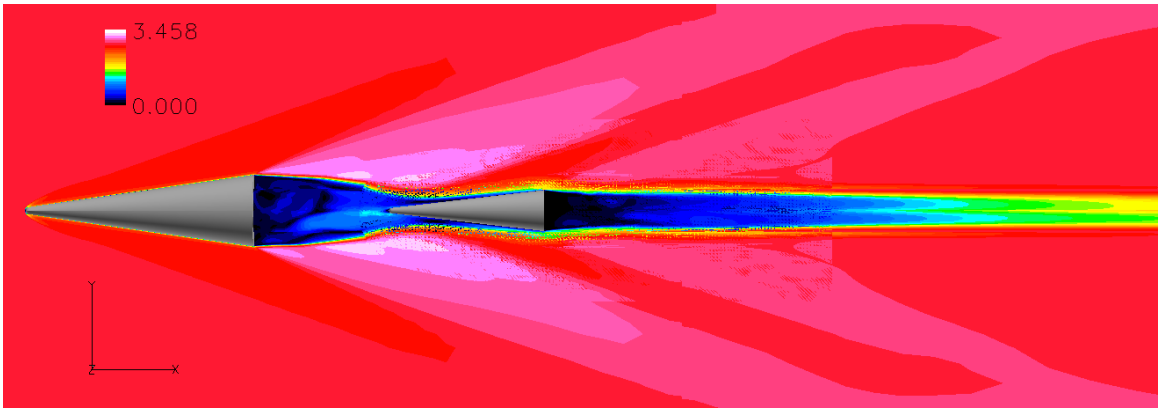

(b) Dynamic Solution at x/D = 4 (15G Ejection Load)

Figure 4.3: Contours of Mach for Static/Dynamic Solution at x/D = 4

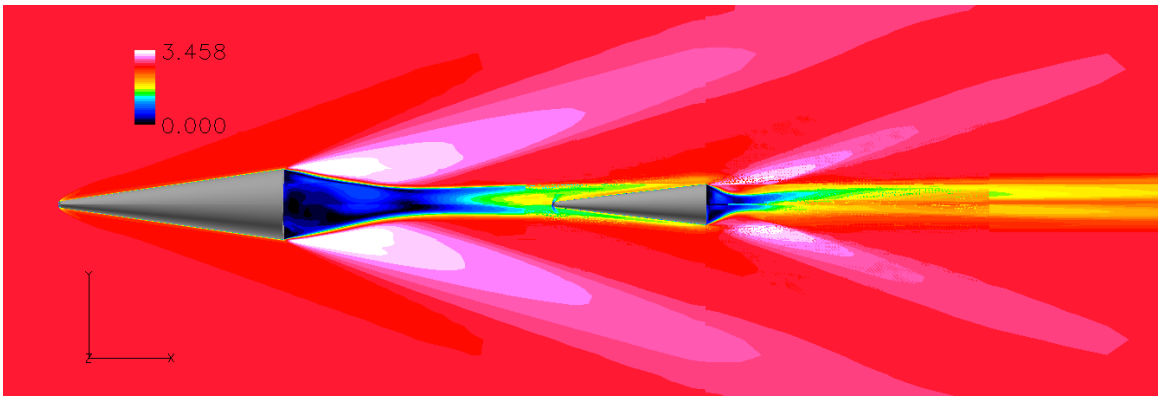

(a) Static Solution at x/D = 6

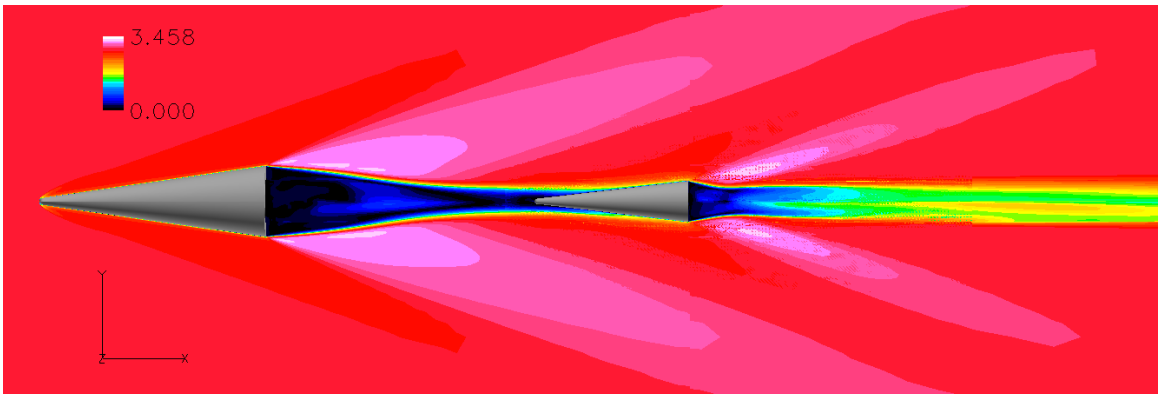

(b) Dynamic Solution at x/D = 6 (15G Ejection Load)

Figure 4.4: Contours of Mach for Static/Dynamic Solution at x/D = 6

The x/D = 2 case in Figure 4.7 differs from the previous two separation instances in that C_P in the inviscid flow region (separated from the turbulent recirculation region by the shear layer) is completely different between static and dynamic problems. The static case shows a much lower C_P from the inviscid region (y $\approx$ 0.5), passing through the shear layer and into the viscous recirculation near wake region of the store. Even though the static/dynamic systems at x/D = 2 have approximately the same pressure expansion strength, the lower C_P through the inviscid flow region means lower base pressure and higher drag for the static case.

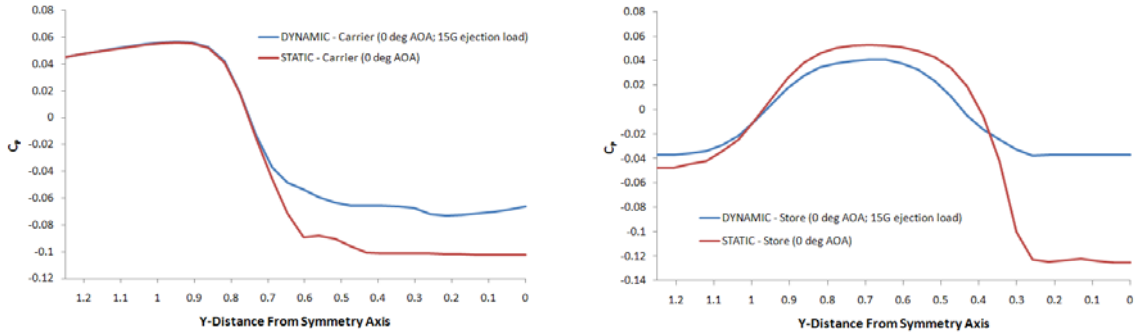

(a) C_P Through Carrier Expansion Region (b) C_P Through Store Expansion Region

Figure 4.5: C_P Through Expansion and Shear Layer for Static/Dynamic Solutions at x/D = 4

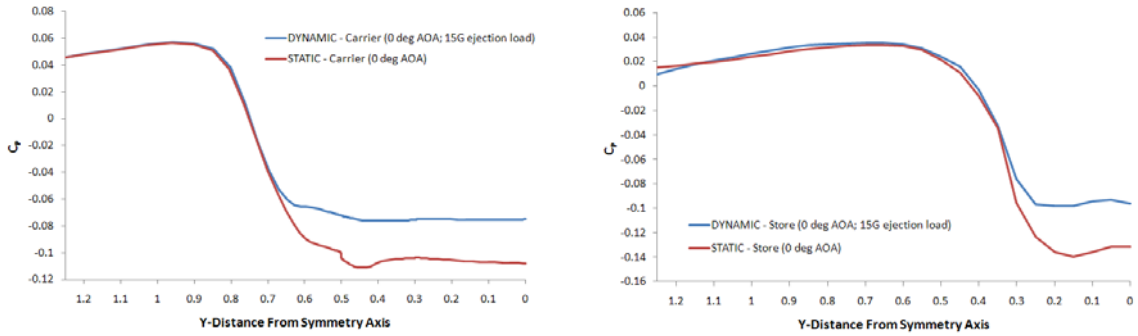

(a) C_P Through Carrier Expansion Region (b) C_P Through Store Expansion Region

Figure 4.6: C_P Through Expansion and Shear Layer for Static/Dynamic Solutions at x/D = 6

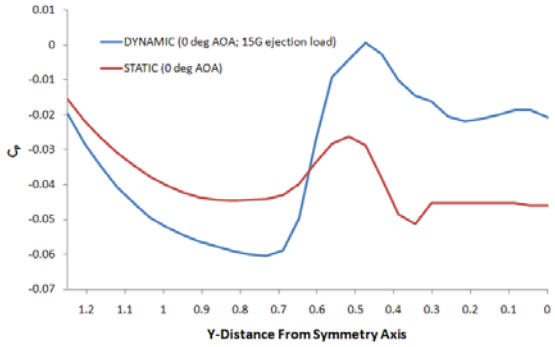

Figure 4.7: C_P Through Expansion and Shear Layer for Static/Dynamic Solutions at x/D = 2

It is apparent that when the store/carrier system is allowed to dynamically separate, the flow field changes to such an extent that an equivalent static system does not accurately represent the dynamic solutions. This because the static system does not account for the relative motion between the carrier and store which has a significant effect on base pressure and drag.

4.2 Separation at Various Flight Path Angles

For the following series of separation simulations, the vehicle flight path angle was changed by adjusting the gravity force vector from 0° to 90° relative to the horizon. In all four cases, an ejection load of 15G's (15,000 lbs) was applied in the ±x-direction at the center of gravity of the carrier vehicle and store body over the span of 0.05 seconds. Since both bodies are completely unconstrained through motion, the ejection force at any given γ has an equal and opposite effect on each of the two bodies. The separation event was initiated at a free stream Mach number of 2.90 and run out for a total of 1.10 seconds.

Figure 4.8 gives the Mach contours for the $\gamma = 0°$ case at different separation distances (x/D) throughout the separation simulation. These flow visualizations illustrate the expected characteristic flow field at different points in the separation event as discussed in Section 2.1.1. Initially, in Figure 4.8(a), the store is in the stowed position and a classic base flow profile is visible with an expansion wave off the aft

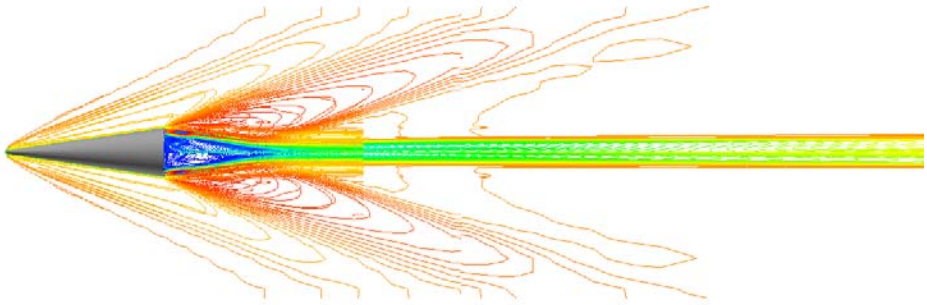

(a) x/D = 0 (time = 0.0 sec)

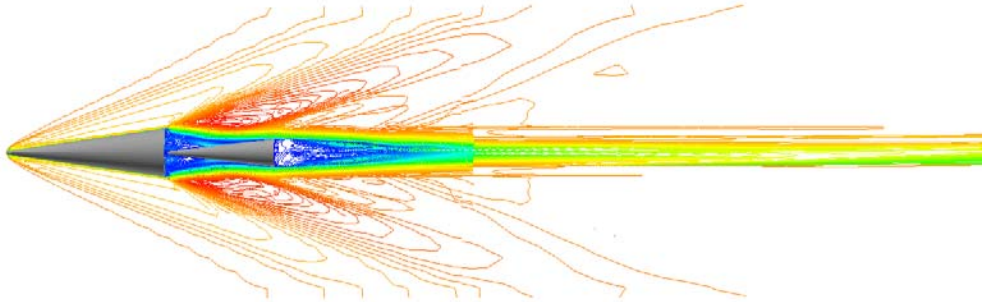

(b) x/D = 2.22 (time = 0.165 sec)

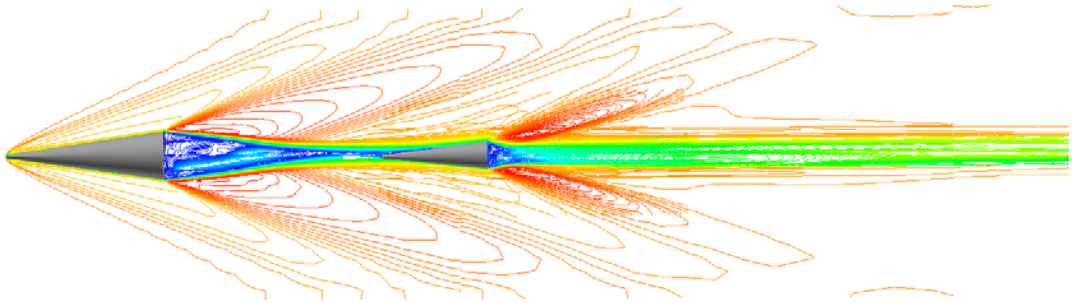

(c) x/D = 6.56 (time = 0.509 sec)

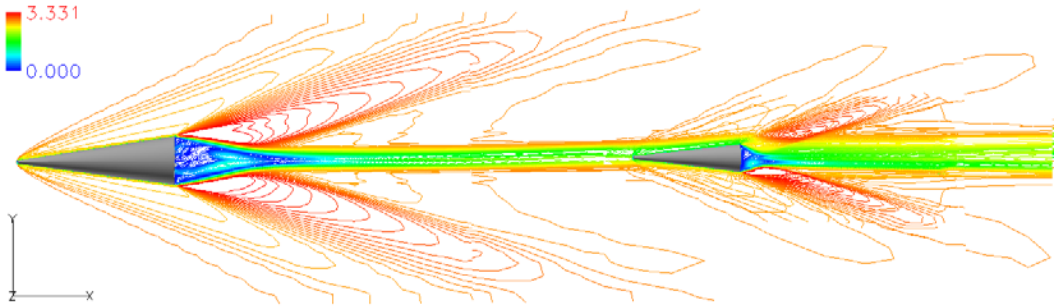

(d) x/D = 11.45 (time = 1.10 sec)

Figure 4.8: Mach Contours at Various Separation Distances for $\gamma = 0°$

corner of the carrier body and compression shocks forming as the flow reattaches at the axis of symmetry. In addition, the low velocity, low pressure, recirculation area in the near wake region can be seen.

In Figure 4.8(b), the store has separated a distance of x/D = 2.20. It can be seen that the compression shock occurs further aft, displacing the rear stagnation point. At a separation distance $2.2 \geq x/D \leq 6.55$ the shear layer is unable to reattach, preventing flow reattachment at the axis of symmetry. Up to this point the store is under a 'suction' force as it stays submerged in wake of the lead vehicle.

Finally, as shown in Figure 4.8(d), at x/D of 11.44, the store is no longer influencing the lead vehicle and has developed its own leading shock. The lead vehicle has in fact reached a point of maximum drag, and begun moving back in the positive x-direction.

For the other three cases at $\gamma = 30°$, $\gamma = 60°$, and $\gamma = 90°$, the Mach contours look quite similar at the same separation times as Figure 4.8. This is not necessary surprising since none of the vehicles have been set at any incidence to the free-stream. Mach contour plots for each of the other three cases are included in Appendix A.

Figures 4.9 and 4.10 provide an overview of the carrier and store trajectory vs. simulation time in seconds. In these figures, x_o/D and y_o/D give the distance traveled in the x and y direction respectively from time t=0 seconds, referenced against the carrier base diameter. For all cases in this section, the ejection force was applied over a time span of 0.05 seconds resulting in an ejection stroke length of x/D = 0.39 (ejection stroke length is represented by the green dot located on the figure).

Since gravity components are included, the force of gravity will delay the carrier's movement back in the positive x-direction at flight angles of $\gamma = 30$, $\gamma = 60$, and $\gamma = 90°$. At a $\gamma = 90°$, the store could impact the carrier if it does not reach terminal velocity much sooner than the carrier does. By the end of the simulation, the $\gamma = 90^0$ case has started movement in the opposite direction (negative x-direction)

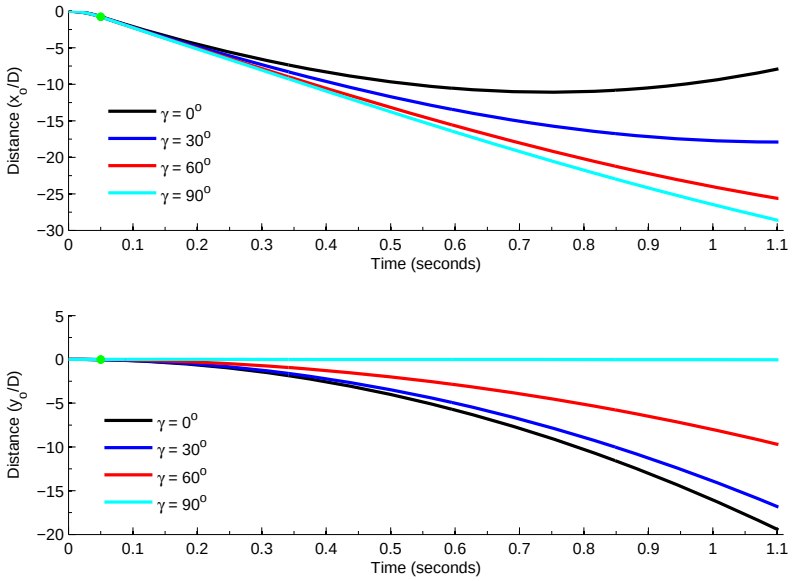

Figure 4.9: Carrier Trajectory at Varying Flight Path Angles (γ)

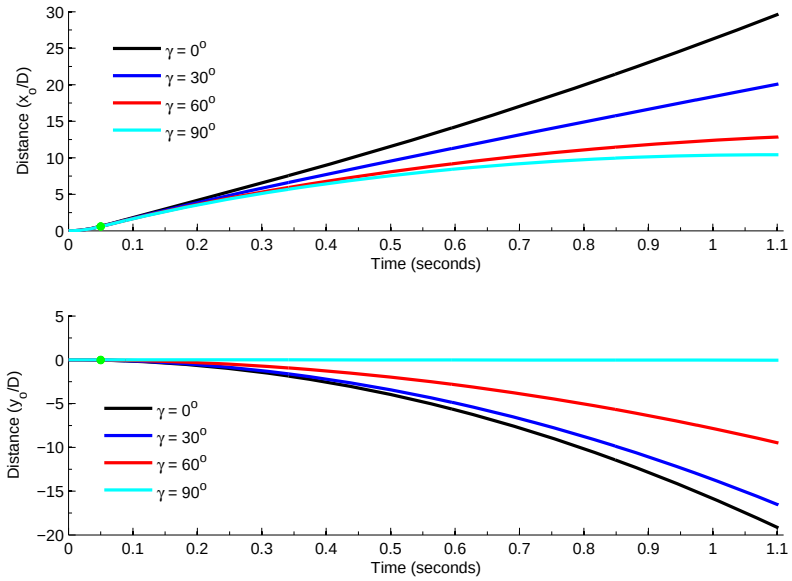

Figure 4.10: Store Trajectory at Varying Flight Path Angles (γ)

due to gravitational and drag forces. There is evidence of this in Figure 4.10(a), where the distance traveled by the store has plateaued.

In Figure 4.11 the coefficient of drag or C_D for the carrier and store is plotted for all γ as a function of the separation distance (x/D) between the two bodies. For further data on the coefficients of body force in the x, y, and z directions on either body, refer to Figures A.4 and A.5 in Appendix A. Generally the bodies had little movement in the y and z direction as x/D increased.

For all cases, a similar trend emerges in the C_D profiles where a minimum drag 'bucket' appears early in the simulation. In the flight angle cases shown, the minimum drag point for the carrier body takes place at a separation distance of x/D = 3.0.

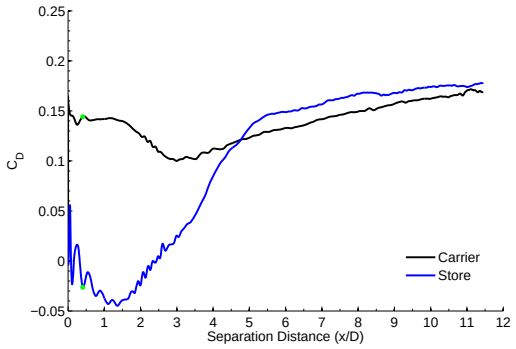

(a) Carrier/Store C_D at $\gamma = 0°$

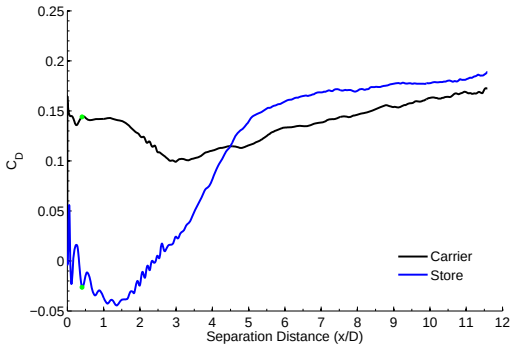

(b) Carrier/Store C_D at $\gamma = 30°$

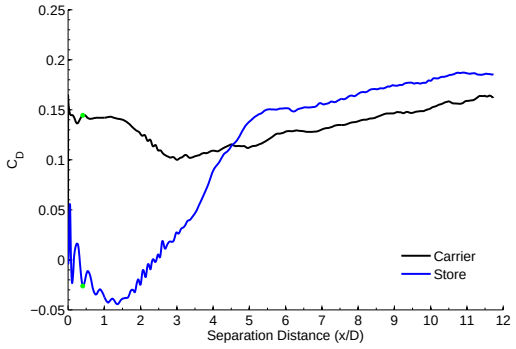

(c) Carrier/Store C_D at $\gamma = 60°$

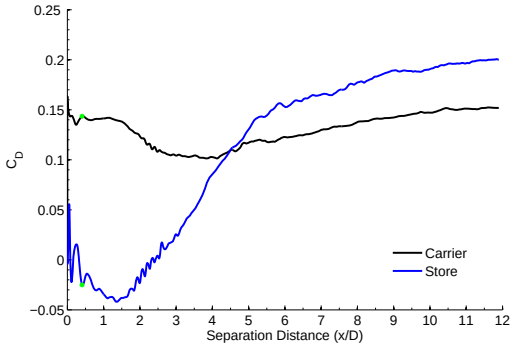

(d) Carrier/Store C_D at $\gamma = 90°$

Figure 4.11: Carrier/Store Drag Coefficients at all $\gamma's$

The reduction in drag of the lead vehicle plotted in Figure 4.11 is consistent with experimental and numerical results in which base drag can be reduced by altering the afterbody of a projectile with the introduction of some angle relative to the forebody [7]; typically this is referred to as a boattailed body. In Figure 4.12, a schematic of supersonic flow over the separating carrier/store system illustrates how a boattailing effect might take place (shown in red). That phenomena is probably occurring in this problem, where the separating store is effectively reducing the strength of the expansion wave as it sweeps across the carrier/store system. This leads to reduced mass entrainment and an increase in base pressure, or otherwise reduction in drag, on the carrier body. As the carrier and store separate further, drag on the carrier begins to increase.

Since the RV system was not placed at any incident to the flow prior to deployment, the store body drag coefficients in 4.11 exhibit similar drag profiles. As the flight path angle steepens, the gravity vector increasingly contributes to the axial body forces, causing an increase in store C_D. It can also be seen that the store drag has become greater than the carrier drag as the separation distance increases. As

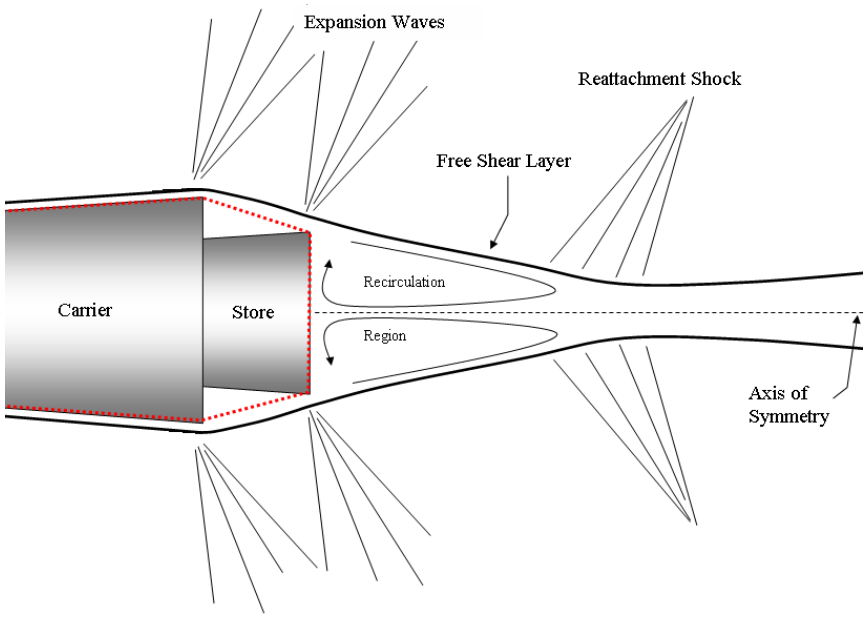

Figure 4.12: Axisymmetric boattailed flow over carrier with separating store

pointed out in Section 4.1, this is probably not realistic and could be due to shortcomings in the algebraic turbulence model. At no point should the store actually have a greater C_D than that of the carrier - particularly since the store is firmly positioned directly in the wake of the carrier for the entirety of the separation event [29]. Finally, there is the characteristic negative or suction force/drag, similar to that seen in the carrier C_D curves, which begins immediately upon deployment and ends for all cases at x/D=2.43 for the store bodies.

Relative pitch, yaw and roll data, as well as body moment coefficient plots are provided in Appendix A.1. From both the angular displacement data and moment coefficient data, the store is shown to be quite stable in the wake of the lead vehicle, and tends to stay there. This is consistent with numerical and experimental results from Ober *et al.* [19], [18] and Erengil *et al.* [8].

Acceleration and velocity data (in the x-direction) relative to the carrier and store body's initial state are plotted in Figures 4.13 and 4.14 against separation distance. In the carrier velocity and acceleration history plots (Figure 4.13), the initial ejection force accelerates the carrier for the $\gamma = 0°$ case nearly instantaneously at about $580 ft/sec^2$, while at an initial $\gamma = 90°$, the carrier accelerates to over $615 ft/sec^2$. The acceleration rates for the other two cases are bounded by those values and follow a trend of greater carrier acceleration rates for higher initial γ's. These differences in acceleration rates are due to the increasing contribution of gravity forces acting on the carrier. Immediately following the conclusion of the ejection force, the carrier experiences acceleration in the opposite direction due to drag. The minimum drag point discussed previously can be seen with a lower acceleration around the x/D=2.98 mark along with a slight leveling of the velocity curve.

In Figure 4.13(a), the point where the carrier starts moving back (maximum drag point) at x/D=9.0 is more easily seen because of the change to positive velocity. Referencing Figure 4.13(b), at an initial $\gamma = 30°$, it can be seen that by the end of the simulation, the carrier has begun to move back in the direction of the moving

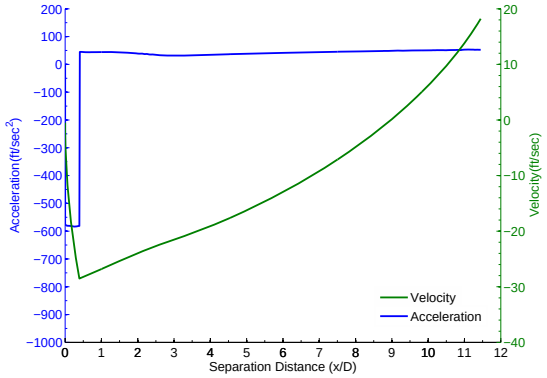

(a) Acceleration/Velocity at $\gamma = 0°$

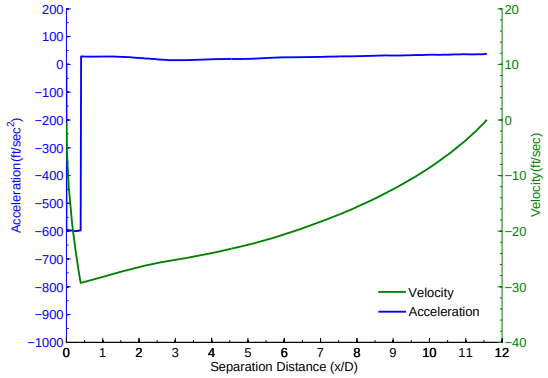

(b) Acceleration/Velocity at $\gamma = 30°$

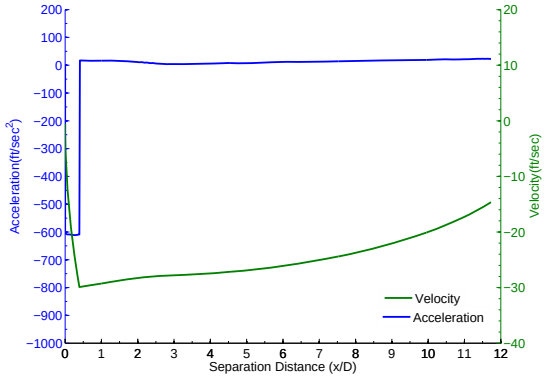

(c) Acceleration/Velocity at $\gamma = 60°$

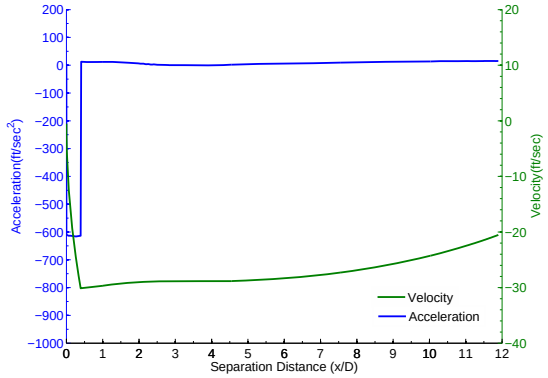

(d) Acceleration/Velocity at $\gamma = 90°$

Figure 4.13: Carrier: Acceleration and Relative Velocity at all $\gamma's$

store. It is apparent that this will eventually take place for all cases presented as the velocity trends towards positive.

Because it is heavier and working against gravity in some cases, the store accelerated at significantly reduced rates compared to the carrier over the course of the imparted ejection force. For the $\gamma = 0°$ case, the store was accelerated away at $\approx 487 ft/sec^2$ while at $\gamma = 90°$ it was accelerated away at $\approx 456 ft/sec^2$.

A synopsis of the final state (after 1.10 seconds) of the carrier and store for each case is provided in Table 4.1 and Table 4.2 respectively. These tables nicely illustrate the trending conditions of the store and carrier as the separation event continues. Note that the $\gamma = 90°$ case results in the largest separation distance by the end of

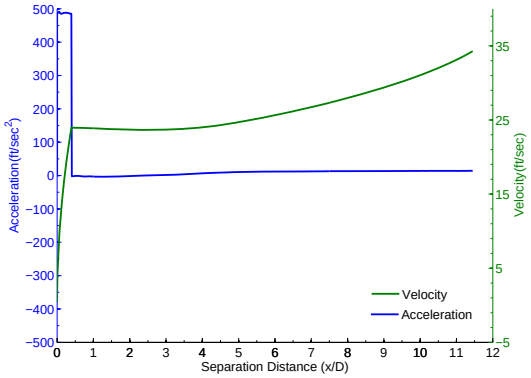

(a) Acceleration/Velocity at $\gamma = 0°$

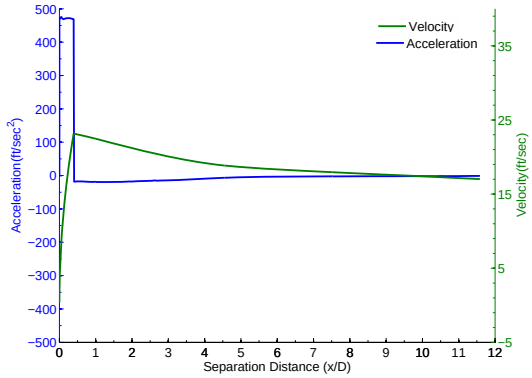

(b) Acceleration/Velocity at $\gamma = 30°$

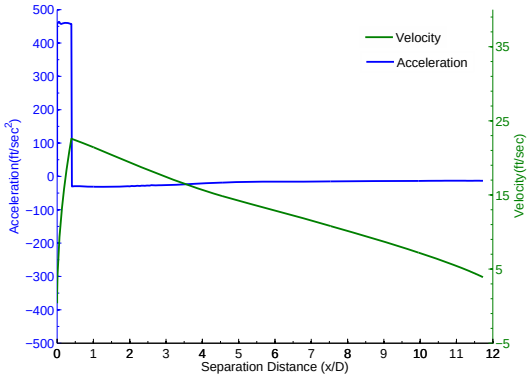

(c) Acceleration/Velocity at $\gamma = 60°$

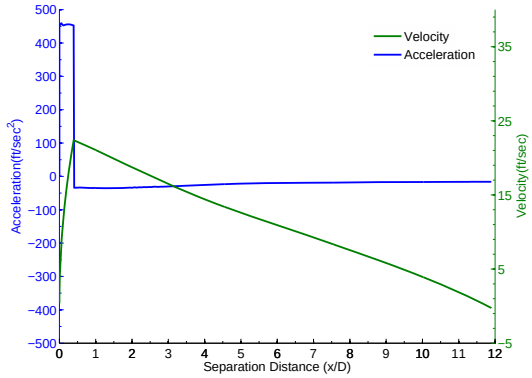

(d) Acceleration/Velocity at $\gamma = 90°$

Figure 4.14: Store: Acceleration and Relative Velocity at all $\gamma's$

the simulation while the $\gamma = 0$ case has the smallest separation distance. This is all relative, however, in that the total difference in separation distance between all cases is only x/D = 0.44.

With the complex relationship that exists between the separation distance, drag, and gravitational forces, it is difficult to predict an optimum flight path angle to initiate store separation. If the store were 'smart' or guided in some way, γ would be irrelevant to the separation success because it could be steered away from the influence of the carrier wake almost immediately without adverse effects on the carrier.

However, when dealing with a 'dumb' or unguided store, a separation event would ideally occur at some $\gamma > 0°$. At $\gamma = 0°$, the store is only moving away from

the carrier at a relative velocity of 7.08 ft/sec at a separation distance of $x/D = 11.45$. With the tendency of the store to stay embedded in the carrier wake, the likelihood of the carrier impacting the store is high. Conversely, when examining a case at some $\gamma > 0°$ such as $\gamma = 90°$, the store is moving away from the carrier at a relative velocity of 20.50 ft/sec and is at a greater x/D than the cases at lower flight path angles. Since the carrier is moving away from the store at such a high relative velocity, it will have time to maneuver out and away from the trailing store before any risk of impact emerges.

Table 4.1: Carrier state at 1.10 seconds for all flight path angles

Case	Separation Distance (x/D)	X-Distance x_o/D	Y-Distance y_o/D	Acceleration ft/sec^2	Relative Velocity ft/sec
$\gamma = 0°$	11.45	-2.40	-5.096	52.59	18.20
$\gamma = 30°$	11.58	-5.45	-5.14	37.56	0.38
$\gamma = 60°$	11.73	-7.81	-2.96	22.86	-14.64
$\gamma = 90°$	11.89	-8.73	-.014	15.15	-20.53

Table 4.2: Store state at 1.10 seconds for all flight path angles

Case	Separation Distance (x/D)	X-Distance x_o/D	Y-Distance y_o/D	Acceleration ft/sec^2	Relative Velocity ft/sec
$\gamma = 0°$	11.45	9.043	-5.852	14.25	35.28
$\gamma = 30°$	11.58	6.12	-5.050	.096	17.029
$\gamma = 60°$	11.73	3.92	-2.89	-13.048	3.90
$\gamma = 90°$	11.89	3.172	-.014	-16.15	-.026

4.3 Separation at Various Angles of Attack

Results of a sweep through angle of attacks from 0° to 8° are provided in this section. For this series of tests, two different computational domains were required; one for the low AOA cases ($\alpha = 0°$ and 2°) and a larger one for the high AOA cases ($\alpha = 4°$, 6°, and 8°).

At this time, Beggar does not allow the store to be appropriately constrained within the carrier cavity such that trim conditions of the carrier/store system can

be met before store ejection. Additionally, for all cases in this section, gravitational forces were neglected in order to observe only the aerodynamic impact on the bodies. Therefore, upon store ejection, the carrier and store experienced wind driven pitching oscillations which were proportional in magnitude to the initial incidence of the two body system.

With more movement and angular displacement in the higher AOA cases, the larger grid discussed in Section 3.2 was necessary to completely capture all flow characteristics. In addition, two separate ejection loads were applied: a 15G ejection force over the span of 0.05 seconds for the low AOA cases and a 40G ejection force over the span of 0.07 seconds for the higher AOA cases.

Since Beggar does not allow a store to be constrained relative to a moving body, the ejection force had to be much greater at higher AOA's due to large moments and pitching of the carrier body. With lesser ejection forces the store would impact the carrier cavity while exiting. Possible code improvement and modification to allow lower ejection forces will be discussed in Chapter IV

4.3.1 Low Angle of Attack Cases. For the low AOA cases, the separation simulation was initiated at a free stream Mach number of 2.90 and run out to a time of 1.10 seconds. Both carrier and store were released at untrimmed conditions and are unconstrained for free movement. Mach contours for $\alpha = 2^\circ$ at different separation distances are presented in Figure 4.15. Mach contours for the $\alpha = 0^\circ$ case are almost identical to Figure 4.8 and are therefore provided in Appendix A.

In Figure 4.15, because of the RV's initial incidence to free-stream, the store and carrier behave differently than the $\alpha = 0^\circ$ or $\gamma = 0^\circ$ cases. It can be seen that store appears to slip into a position somewhat below the symmetry axis of the carrier vehicle very early in the simulation, and maintains that off-axis location through the duration of the separation. This is due to an immediate windward pitch down action on the part of the carrier as the store is ejected aft, acting to place the store below the carrier symmetry line. In addition, the store experiences a more gradual and

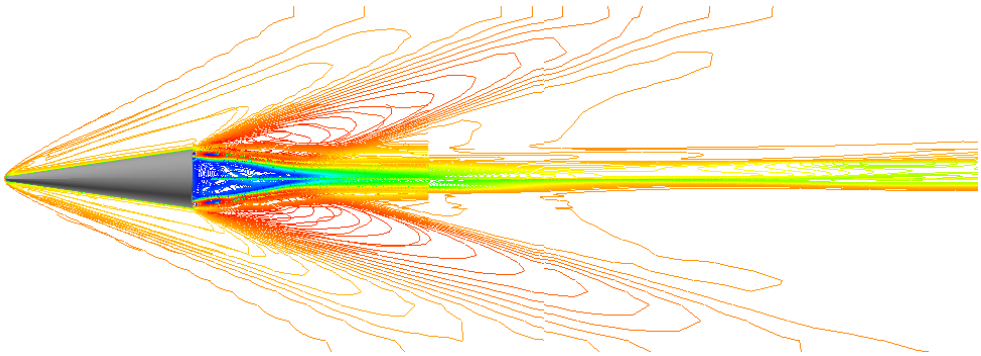

(a) x/D = 0 (time = 0.0 sec)

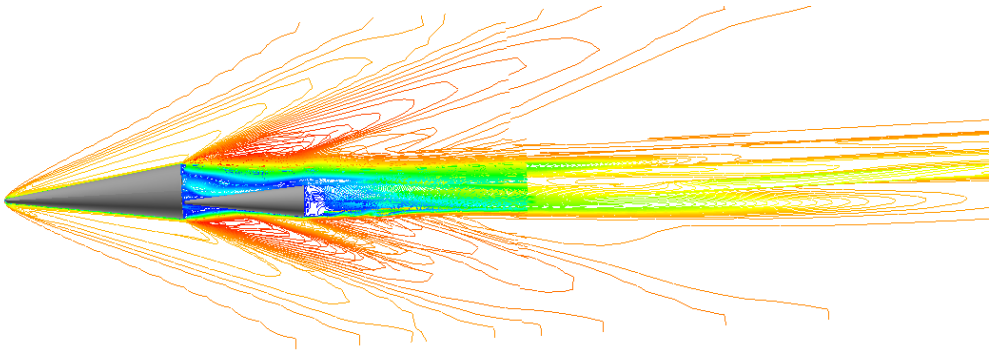

(b) x/D = 2.20 (time = 0.165 sec)

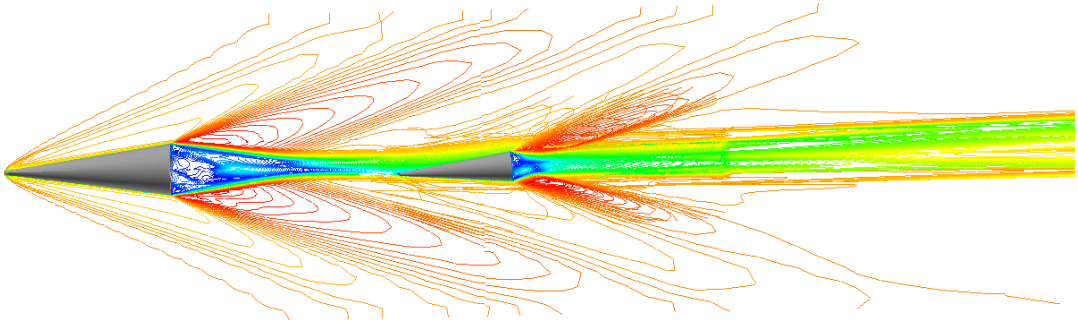

(c) x/D = 6.54 (time = 0.509 sec)

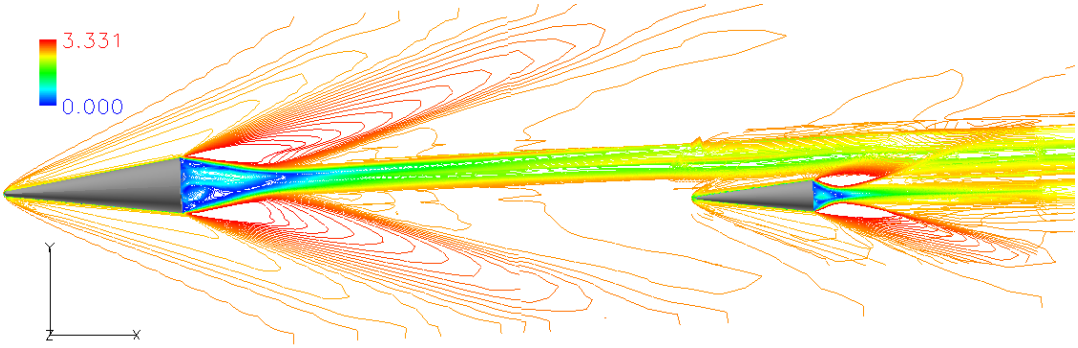

(d) x/D = 11.35 (time = 1.10 sec)

Figure 4.15: Mach Contours at Various Separation Distances for $\alpha = 2°$

larger pitch down orientation as it travels aft and moves largely out of the wake of the carrier.

To illustrate the oscillatory pitching conditions that the carrier/store bodies experienced, the angular displacement history of the carrier and store flights are provided in Figures 4.16 and 4.17. Both the carrier at initial $\alpha = 0°$ and $\alpha = 2°$ have oscillatory tendencies in pitch and yaw, but at $\alpha = 2°$, the amplitudes in pitch and yaw are at least a magnitude greater. Similarly, the store at $\alpha = 2°$ has larger pitch and yaw values, but peaks much less frequently than the store released at an initial $\alpha = 0°$. Body force moment history plots are provided in Appendix A and reflect the oscillatory behavior in angular displacement of the store and carrier. As discussed

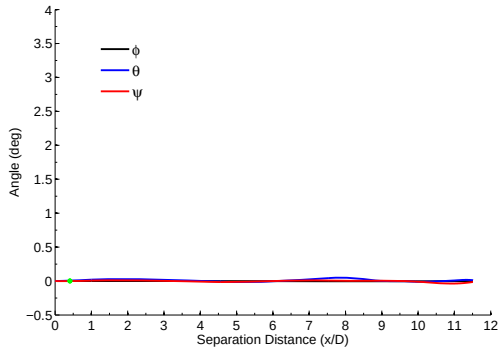

(a) Angular Displacement at $\alpha = 0°$

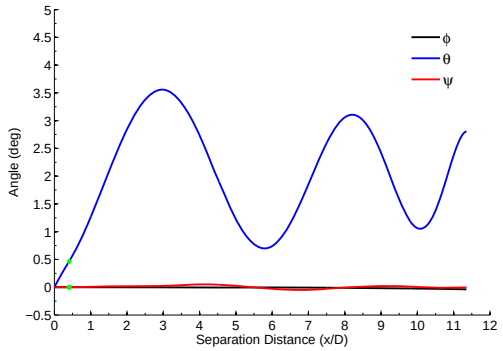

(b) Angular Displacement at $\alpha = 2°$

Figure 4.16: Carrier: Relative Angular Displacement at $\alpha = 0°, 2°$

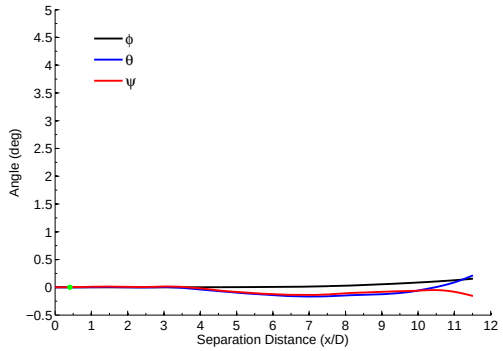

(a) Angular Displacement at $\alpha = 0°$

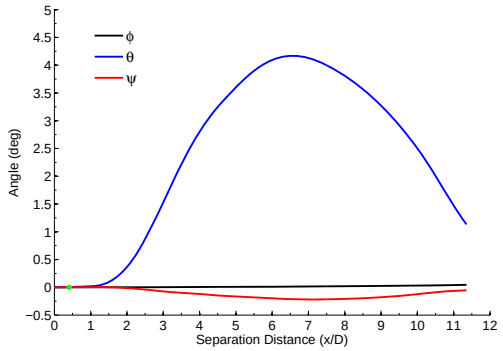

(b) Angular Displacement at $\alpha = 2°$

Figure 4.17: Store: Relative Angular Displacement at $\alpha = 0°, 2°$

earlier, this is to be expected since the carrier/store system has not settled to a trim condition prior to store release.

Trajectory data for this set of separation tests are displayed in Figure 4.18 and 4.19. As in previous plots, the length of the ejection stroke is indicated by a green dot on the plots. In these instances, the ejection stoke length is identical to the γ sweep tests at x/D = .39. In Figure 4.18, both carriers are moving back towards the store after reaching a drag/momentum match by the end of the simulation. At $\alpha = 0°$ the carrier begins to return back by 0.75 seconds into the simulation (x/D = 9.1) and at $\alpha = 2°$, the carrier begins to return back at 0.71 seconds (x/D = 8.60). By the end of the simulation at 1.10 seconds, the carrier/store system at $\alpha = 2°$ reaches a separation distance of 11.35 while the carrier/store system at $\alpha = 0°$ reaches a separation distance of 11.51.

The body drag coefficients show why the carrier in the $\alpha = 2°$ case reverts back in the direction of free stream flow earlier than the carrier at $\alpha = 0°$ while at the same time, the store at $\alpha = 2°$ travels further than the store at $\alpha = 0°$. As given in

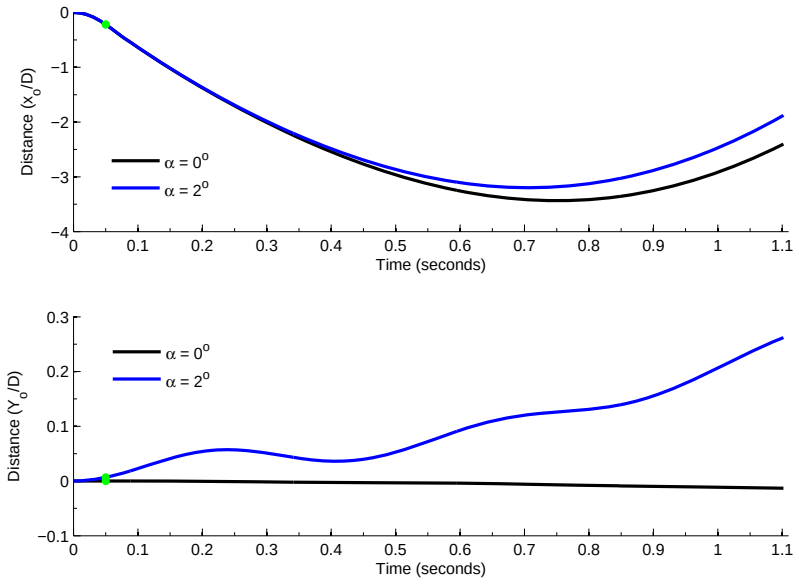

Figure 4.18: Carrier Trajectory at Low AOA's ($\alpha = 0°, 2°$)

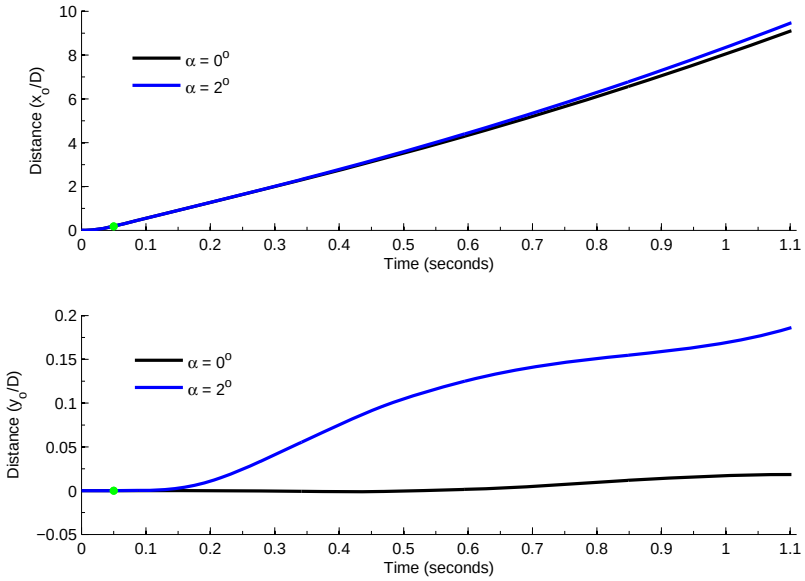

Figure 4.19: Store Trajectory at Low AOA's ($\alpha = 0°, 2°$)

Figures 4.20 and 4.21, C_D is greater for the carrier at $\alpha = 2°$ due to the larger force lift component which retards it's acceleration in the negative x-direction. Furthermore, the so called 'drag bucket' mentioned previously, is shallower and shortened for the $\alpha = 2°$ case compared to the $\alpha = 0°$ case, causing drag to increase earlier and hastening a reversal in direction. Over the same separation distance, Figure 4.21 shows that the suction effect that was observed for all previous separation cases is shortened and reduced for the store released at 2° AOA.

Interestingly, a complex relationship has emerged, where the carrier and store distance traveled (x_o/D) is closely related to amount of time the store spends within the carrier's near wake region. A store that spends more time in the carrier wake achieves a greater separation distance from the carrier and vice-versa for a store that spends less time in the carrier wake. In this 2° AOA case, the store is forced down slightly out of the wake region of the carrier vehicle (due to its pitching movement), acting to move it off centerline, increasing drag on itself as well as the carrier. This type of behavior is also observed in the high AOA cases discussed in Section 4.3.2.

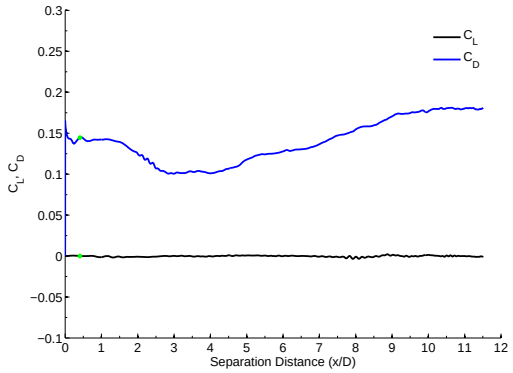

(a) Carrier C_L, C_D at $\alpha = 0°$

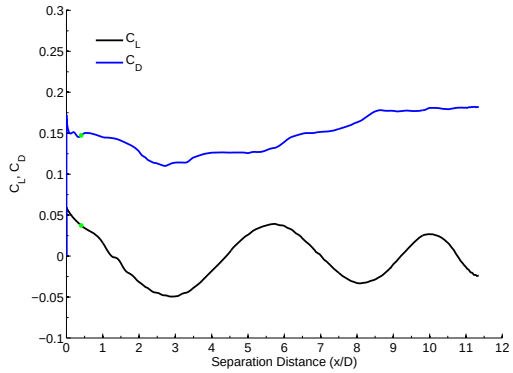

(b) Carrier C_L, C_D at $\alpha = 2°$

Figure 4.20: Carrier Lift/Drag Coefficients at $\alpha = 0°, 2°$

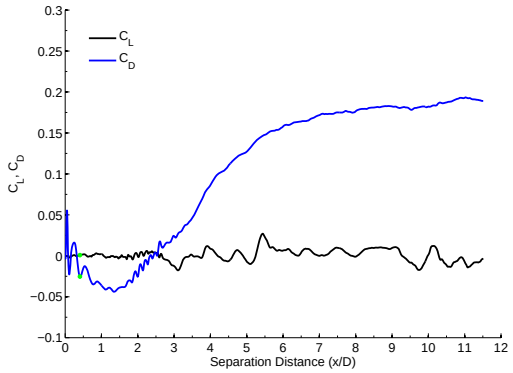

(a) Store C_L, C_D at $\alpha = 0°$

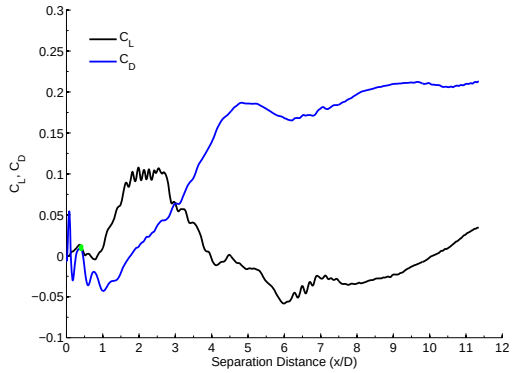

(b) Store C_L, C_D at $\alpha = 2°$

Figure 4.21: Store Lift/Drag Coefficients at $\alpha = 0°, 2°$

Baseline force coefficient plots for the carrier and store at separation distance are provided in Appendix A. Velocity and acceleration plots are provided in the same location for additional reference. Both separation profiles in the velocity/acceleration plots are very similar and do not contribute significantly to this discussion.

Pertinent data for the Carrier/Store state at the end of the 1.10 second simulation is given in Tables 4.3 and 4.4. Here it can be seen that the store is moving away from the carrier at the initial $\alpha = 0°$ state at a rate of 15.48 ft/sec, while at the $\alpha = 2°$ case the store is separating from the carrier at a velocity of 15.01 ft/sec. Although the $\alpha = 2°$ case ends with a smaller separation distance, the store has slipped mostly out

of the carrier wake and is probably in no danger of impacting the carrier as it moves back in the positive x-direction. Even though there is a larger net separation distance for the $\alpha = 0°$ case, the store is still embedded in the wake of the carrier vehicle and remains at risk of eventually impacting the carrier. If the store is guided, this would not present a problem. However, if the store were unguided, it would be safer to release the store at some AOA $> 0°$ so that successful separation was guaranteed.

Table 4.3: Carrier State at 1.10 seconds for $\alpha = 0°, 2°$

Case	Separation Distance (x/D)	X-Distance x_o/D	Y-Distance y_o/D	Acceleration ft/sec^2	Relative Velocity ft/sec
$\alpha = 0°$	11.51	-2.40	-.031	56.27	19.47
$\alpha = 2°$	11.35	-1.88	.26	56.71	22.06

Table 4.4: Store State at 1.10 seconds for $\alpha = 0°, 2°$

Case	Separation Distance (x/D)	X-Distance x_o/D	Y-Distance y_o/D	Acceleration ft/sec^2	Relative Velocity ft/sec
$\alpha = 0°$	11.51	9.11	0.018	15.13	34.95
$\alpha = 2°$	11.35	9.48	0.19	16.95	37.070

4.3.2 High Angle of Attack Cases. The high AOA series of separation tests consisted of $\alpha = 4°$, $6°$, and $8°$ initial conditions for the carrier/store system. As mentioned earlier, an ejection load of 40G's was applied for the ejection force resulting in an equivalent ejection stroke length of x/D = 2.2, which is the approximate length of the store body. The combination of ejection stroke length and ejection force magnitude was required to safely deploy the store aft. As a reminder, both store and carrier were unconstrained for the length of the separation simulation and released at untrimmed conditions. The separation scenarios covered a total physical time of 0.60 seconds in a free-stream flow of Mach 2.90.

The Mach contours at $4°$, $6°$, and $8°$ AOA show increasingly larger pitch and yaw displacements as expected, due to the untrimmed conditions. The $\alpha = 8°$ set of Mach contours, is provided in Figure 4.22 for different separation distances during

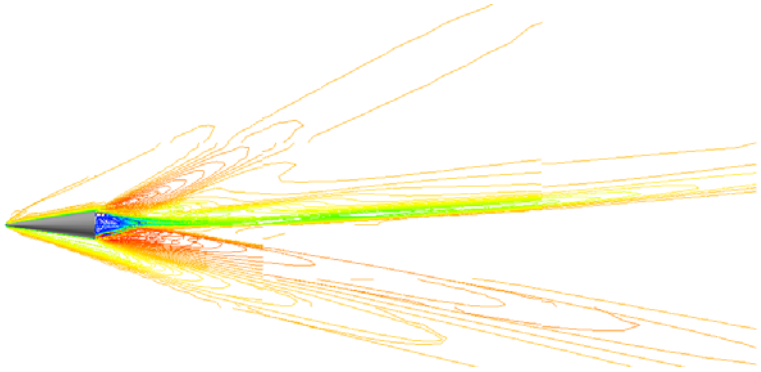

(a) x/D = 0 (time = 0.0 sec)

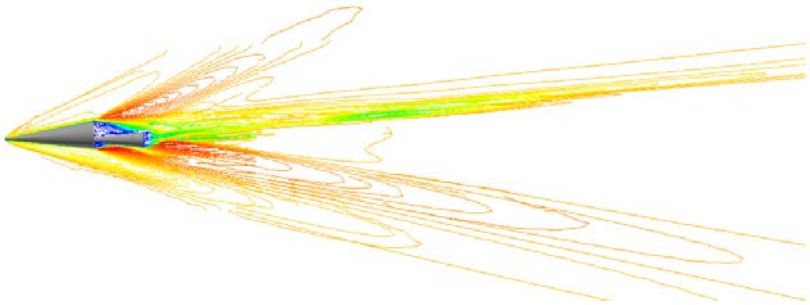

(b) x/D = 1.80 (time = 0.063 sec)

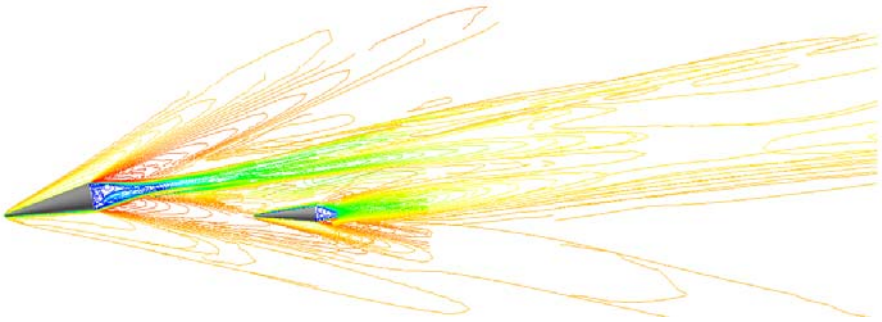

(c) x/D = 7.99 (time = 0.165 sec)

(d) x/D = 32.72 (time = 0.60 sec)

Figure 4.22: Mach Contours at Various Separation Distances for $\alpha = 8°$

the simulation. Figures A.17, A.18 in Appendix A shows the separation sequence at 4° and 6° respectively. The rotation and movement of the carrier and store relative to each other is clearly visible and similar, albeit on a larger scale, to the simulations in Section 4.3.1.

Yaw and roll angle remains basically constant for this set of simulation results due to the high ejection force and shortened time span. Therefore, only change in pitch for the carrier and store relative to the different ejection orientations is presented in Figure 4.23. Predictably as the release AOA gets higher, so does the change in pitching angle. Even with the short simulation time and large ejection force, a pattern of continually damped oscillatory behavior, similar to Figures 4.16 and 4.17 does emerge. It is also likely that the pitching motion will continue to damp out - probably somewhere near 0° AOA.

Force histories in the x, y, and z direction are provided in Appendix A. With the x and y components of force contributing more and more to drag and lift, it is difficult to see a comparison of the aerodynamic forces action on the two body systems. To more easily compare, the drag and lift coefficients or C_L and C_D relative to the global CFD coordinate system, are provided in Figure 4.24.

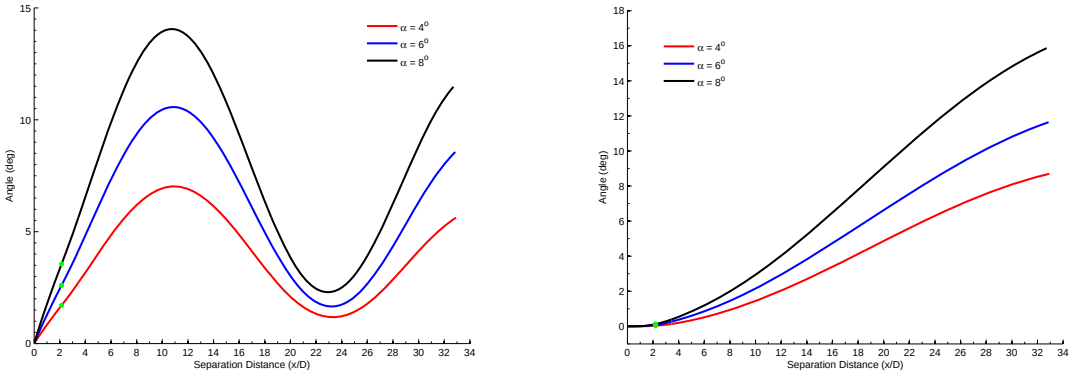

(a) Carrier: Pitch Angle Displacement at $\alpha = 4°, 6°, 8°$

(b) Store: Pitch Angle Displacement at $\alpha = 4°, 6°, 8°$

Figure 4.23: Relative Pitch Angular Displacement at $\alpha = 4°, 6°, 8°$

In Figure 4.24(d) the characteristic drag bucket is once again observed for the store body when it is near the carrier. When the store is deployed at $\alpha = 8°$ it breaks free of the suction effect sooner than the $\alpha = 6^0$ case which in turn is subjected to positive drag forces sooner than the $\alpha = 4°$ case. The C_D profile for the carriers does not exhibit any noticeable benefit of reduction in drag from the trailing store in its wake as was observed in the lower AOA cases (and associated lower ejection force). Instead, it changes in concert with the pitching of the vehicle, resulting in overall increased drag at higher initial angles of attack.

At such high ejection forces, trajectory and velocity/acceleration show little difference. For reference, those figures are included in Appendix A. The state of the two bodies at the end of the simulation is more useful and provides a performance

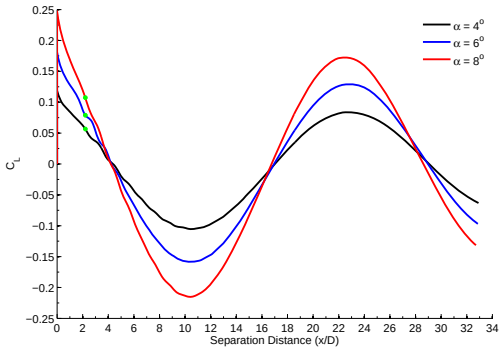

(a) Carrier C_L at $\alpha = 4°, 6°, 8°$

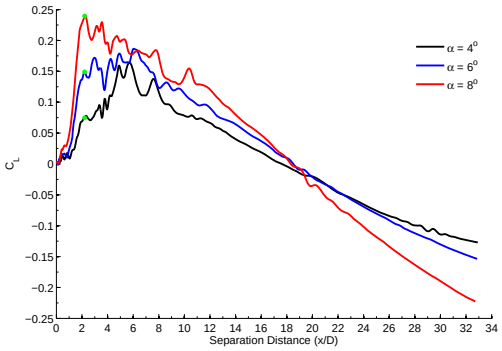

(b) Store C_L at $\alpha = 4°, 6°, 8°$

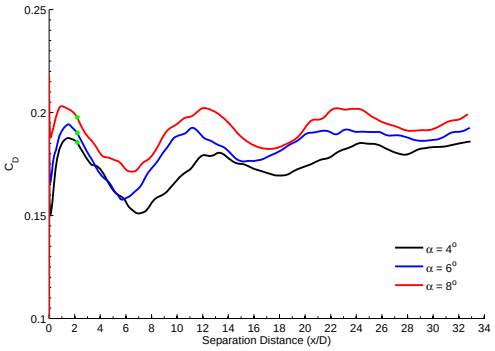

(c) Carrier C_D at $\alpha = 4°, 6°, 8°$

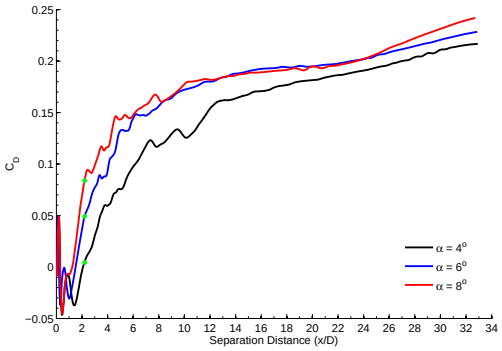

(d) Store C_D at $\alpha = 4°, 6°, 8°$

Figure 4.24: Carrier/Store Lift/Drag Coefficients at $\alpha = 4°, 6°, 8°$

benchmark of sorts. Tables 4.5 and 4.6 give this data. The relative velocity between store and carrier is consistent with the results in Section 4.3.1. At the highest initial AOA of $\alpha = 8°$, the store is moving away from the carrier at 178.89 ft/sec whereas at $\alpha = 4°$ the relative store velocity is 180.62 ft/sec.

The difference between the two is fairly insignificant, but nonetheless continues the trend as it relates to a separation event. Consistent with the results from Section 4.3.1, the lower initial AOA system has a larger net separation distance, but stays nearer to the wake region of the lead vehicle. Realistically, this data shows that at ejection loads as high as 40G's, AOA is only a factor as it relates to the given vehicle's control authority (pitch, yaw, roll). The store and carrier accelerate away from each other at such high speeds that it is almost a certainty that the store will adequately clear the carrier wake influence and move towards its target before any danger of reconnection or impact materializes. Other issues related to such a high ejection force would be determining the impact on vehicle avionics/electronics equipment as well as the carrier and store structural integrity.

Table 4.5: Carrier State at 0.6 seconds for $\alpha = 4°, 6°, 8°$

Case	Separation Distance (x/D)	X-Distance x_o/D	Y-Distance y_o/D	Acceleration ft/sec^2	Relative Velocity ft/sec
$\alpha = 4°$	33.30	-17.39	0.21	59.08	-83.67
$\alpha = 6°$	32.87	-16.87	0.34	62.7	-82.22
$\alpha = 8°$	32.72	-16.71	0.43	67.04	-80.81

Table 4.6: Store State at 0.6 seconds for $\alpha = 4°, 6°, 8°$

Case	Separation Distance (x/D)	X-Distance x_o/D	Y-Distance y_o/D	Acceleration ft/sec^2	Relative Velocity ft/sec
$\alpha = 4°$	33.30	15.91	0.16	18.02	96.95
$\alpha = 6°$	32.87	16.00	0.11	19.46	97.86
$\alpha = 8°$	32.72	16.01	0.065	21.65	98.08

4.3.3 Base Pressure at Angle of Attack. As discussed in Section II, the base pressure and resulting base drag plays an enormous role in the aerodynamic

properties of any given vehicle whose geometry lends itself to the formulation of a base flow environment. For a qualitative comparison of the base pressure on the base of the RV carrier/store system while stowed, refer to Figure 4.25. As the two body configuration is swept through from an incidence of $\alpha = 0^\circ$ to $\alpha = 8^\circ$, a corresponding decrease in C_{PB} occurs. Since the base pressure plays such an important role in the overall drag (over 50% of the total drag can be attributed to the base drag), it also plays in important role in the dynamics of a base store separation event as shown in Sections 4.3.1 and 4.3.2 (Note the slight asymmetry in base pressure across the base for all cases; this could be a result of interpolation error associated with the overset grid configuration or possibly some related numerical artifact).

More intriguing, however, is the significant effect on base pressure that the store body has as it is extended aft only 5 mm or a distance of x/D = .005. Recall from Section 3.4 that the base face had to be offset aft of the carrier face 5 mm (necessary for all cases set at incidence to the flow and applied to the 0° AOA cases for consistency) in order to achieve a successful store separation simulation. From Figures 4.25 a significant difference in base pressure is clearly visible between that of the store and base. The pressure on the store base stays visibly higher than pressure on the carrier base, effectively increasing the base pressure on the two body system. In Section 4.6, the full impact of the extended face is examined in detail.

A comparison of the base pressure coefficients for each case at AOA is shown in Figure 4.26. C_{PB} data was taken directly from the two body system base on the z=0 coordinate and plotted against the non-dimensional radius of the two body system. The increase in pressure on the store face compared to the carrier face is clearly seen in the data. For reference, empirical and theoretical base pressure values [14, 21] at 0° with continous base geometry are included on the plot. In all cases, the base pressure values in this study are higher than the predicted empirical and theoretical values. For those cases at some AOA, this is to be expected because the empirical and theoretical data is only provided at zero incidence to the freestream (in addition to geometric and numerical differences described below).

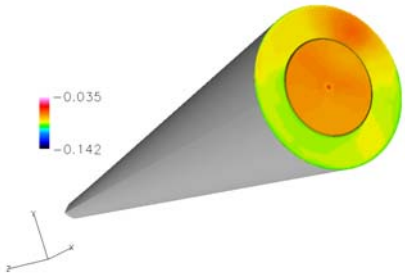

(a) C_PB at $\alpha = 0°$

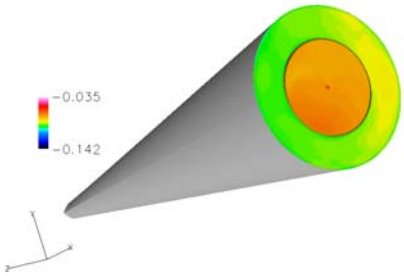

(b) C_PB at $\alpha = 2°$

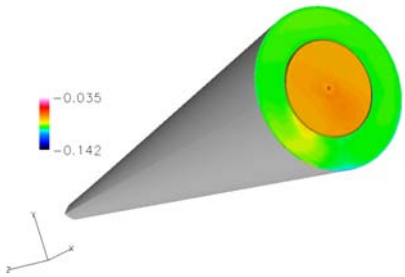

(c) C_PB at $\alpha = 4°$

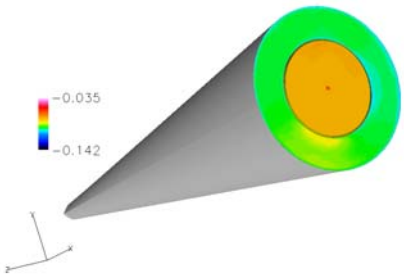

(d) C_PB at $\alpha = 6°$

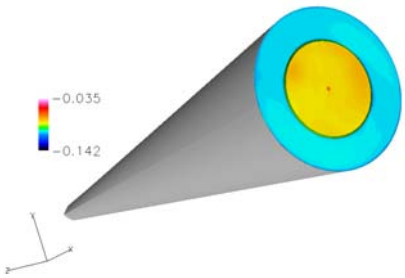

(e) C_PB at $\alpha = 8°$

Figure 4.25: Base Pressure Contours at $\alpha = 0°, 2°, 4°, 6°, 8°$

Results at 0° AOA also do not fall between the theoretical and empirical values for base drag. This also differs from Simko's [29] work (see Figure 1.2) where his numerical base pressure values for the B-L and DES turbulences models (at $\alpha = 0°$) closely matched the theoretical and empirical predictions. The primary reason for this difference is probably due to the store base face offset stowage condition which increases mean base pressure significantly. Another reason for this difference could be the gap at the carrier base face between the store face and carrier face, which may alter the near wake flow field. In addition, recall that with overset grids, the solution across overlapping grid boundaries is non-conservative and could therefore be introducing some numerical error.

As AOA increases, C_{PB} drops from a nominal $C_{PB} = -.0890$ at $\alpha = 0°$ to $C_{PB} = -.1037$ at $\alpha = 8°$ nearing the theoretical base pressure curve. The reason for this continuing drop in pressure becomes obvious once the near wake region is examined.

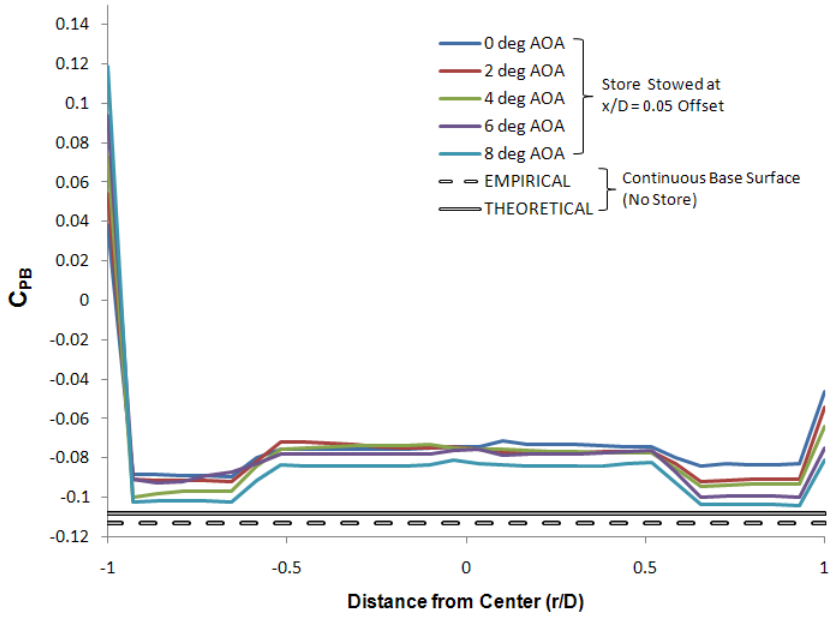

Figure 4.26: C_{PB} at $\alpha = 0°, \alpha = 2°, \alpha = 4°, \alpha = 6°, \alpha = 8°$

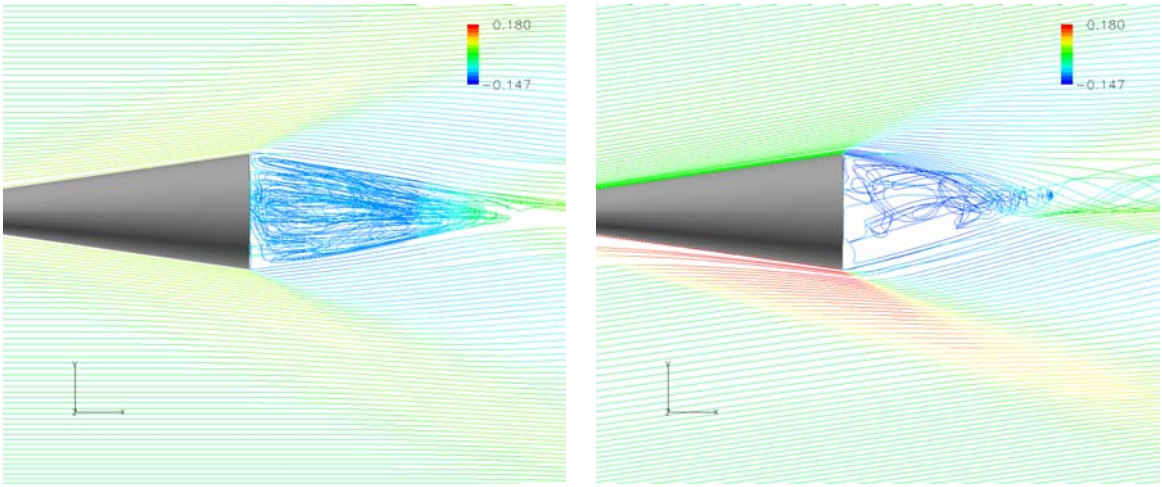

(a) Streamlines of C_P at $\alpha = 0°$ (b) Streamlines of C_P at $\alpha = 8°$

Figure 4.27: Streamlines of C_P for $\alpha = 0°, 8°$

In Figure 4.27, streamlines colored by C_P are displayed, targeting the low pressure near wake region of the stowed store configuration. In this figure, the near wake region of the vehicle for $\alpha = 0°$ is compared to $\alpha = 8°$. From Section 2.1.1 it is known that the size of the recirculation region is directly correlated to the strength of the expansion wave and it's interaction with the shear layer: the smaller the recirculation region, the stronger the expansion wave and therefore the lower the base pressure. This phenomenon is observed here. Figure 4.27(b) shows that at angle of attack, the high speed windward flow impinges on and squeezes the wake, reducing its size and creating a strong expansion wave, thus decreasing C_{PB}. At the same time, in Figure 4.27(a) the comparatively large, axisymmetric near wake region for $\alpha = 0°$ acts to weaken the expansion wave at the body shoulder thus increasing C_{PB}.

The decrease in C_{PB} will not continue indefinitely with angle of attack, however. Lin *et al.* [15] found that for turbulent flows, C_P at the base will decrease for a cone shaped vehicle subjected to supersonic/hypersonic speeds, up to an angle of attack of approximately 15°. At AOA's beyond 15°, C_{PB} will actually begin to increase as the base recirculation region starts to grow.

4.4 Failed Separation

A simulated failed store separation event was examined for the carrier and store at a deployment incidence to free-stream of $\alpha = 0°$. To create the conditions for the failure, the original separation load of 15G's used in Section 4.3.1 was reduced by 50% to 7.5G's. The same ejection force time span of 0.05 seconds was implemented for a total ejection stroke length of 0.19 m. Maximum separation distance achieved for the simulation was at x/D = 2.17 and as shown in Figure 4.28, the end separation distance was at x/D = 0.42, where the store actually re-enters the carrier cavity. Surprisingly, the store did not impact the carrier base or cavity.

The store fails to separate from the carrier(by the end of the simulation) due to an inadequately low ejection force. With the low ejection force, the store stays imbedded in the low pressure wake of the carrier for the entire length of the simulation; it in fact never fully exits the cavity region. Figure 4.29 provides the carrier and store C_D over the time span of the simulation. The black curve represents Carrier/Store C_D over the time period of increasing x/D. The red curve represents C_D over the time period of decreasing x/D, up unto the point where the simulation ends and the store is re-stowed within the carrier cavity.

The distance traveled (in the x-direction) over the time span of the simulation of the carrier and store is shown in Figure 4.30. In that figure, the store is always moving in the positive x-direction, while the carrier has separated a short distance and then moved back to overtake the store. At no point does the store get sucked into the carrier (although it is experiencing a suction force for the majority of the simulation); rather the carrier is pushed back onto the store. The inadequate ejection force combined with the persistent presence of the store within the carrier wake results in the eventual carrier/store impact. Additionally, as the carrier begins to accelerate back towards the store, the store develops a second drag bucket, as it is increasingly submerged into the carrier cavity. As the store returns to the carrier cavity, the carrier drag begins to grow because of a shrinking low pressure wake region.

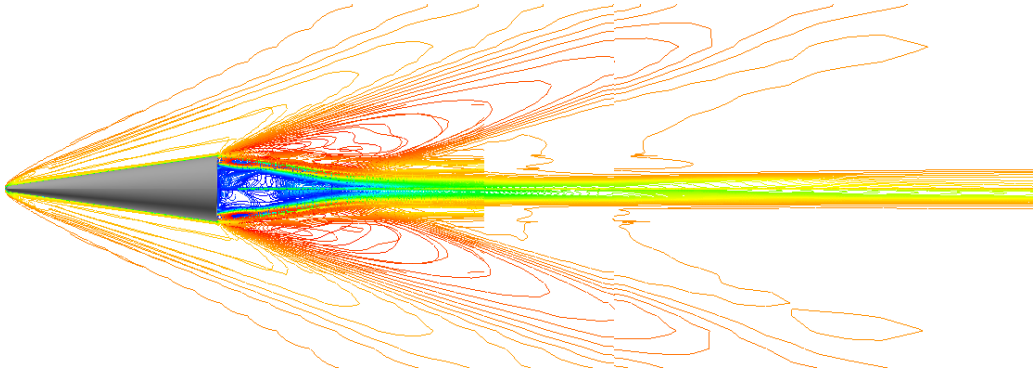

(a) x/D = 0

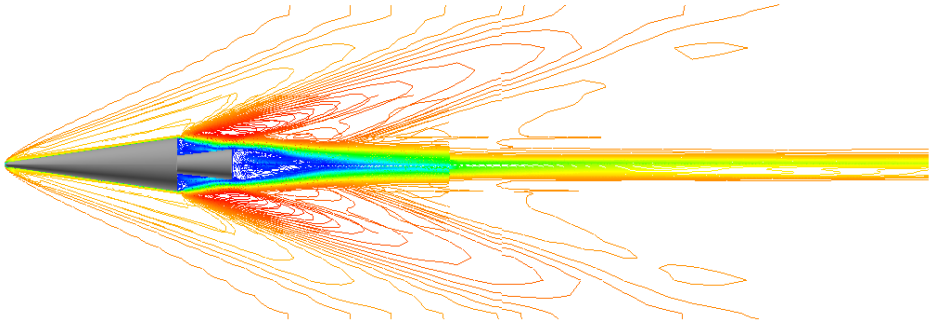

(b) x/D = 0.99

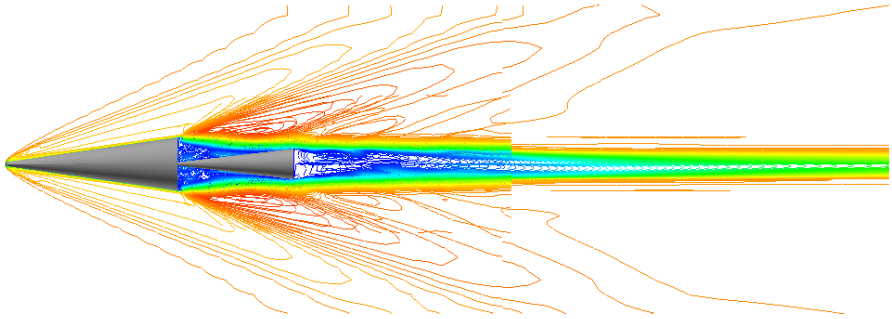

(c) x/D = 2.13

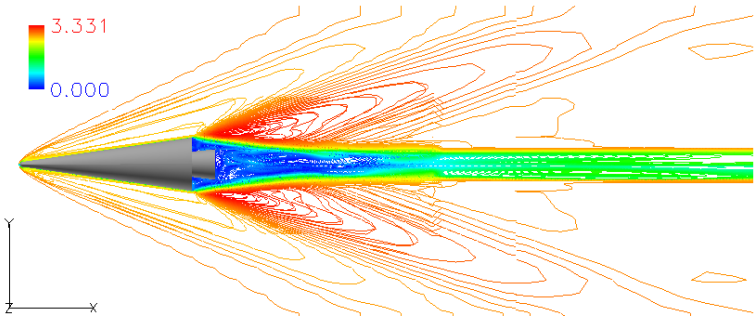

(d) x/D = 0.42

Figure 4.28: Mach Contours at Various Separation Distances for Failed Separation at $\alpha = 0°$

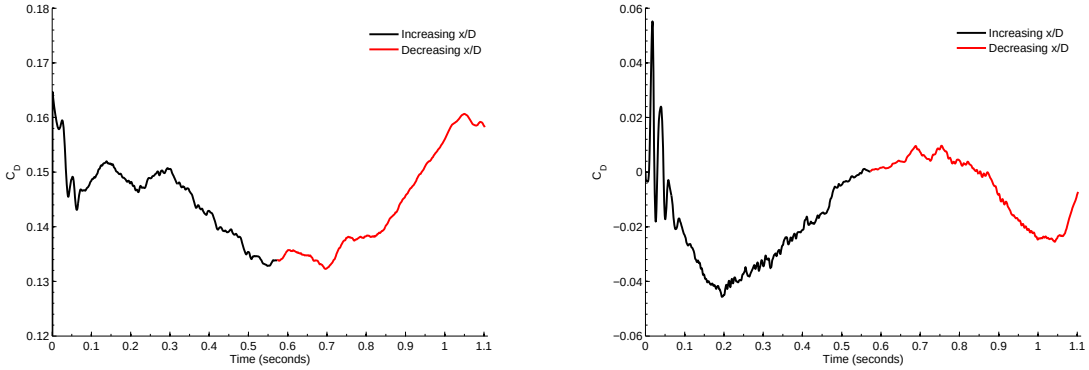

(a) Carrier C_D for Failed Separation at $\alpha = 0°$ (b) Store C_D for Failed Separation at $\alpha = 0°$

Figure 4.29: Drag Coefficients For Failed Separation Event at $\alpha = 0°$

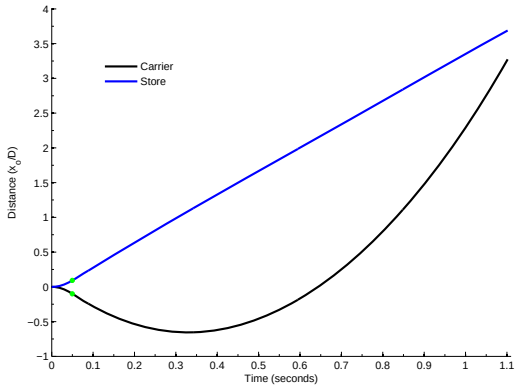

Figure 4.30: Distance Traveled (x-direcion) of Carrier/Store for Failed Separation at $\alpha = 0°$

4.5 Detached Eddy Simulation Study

Dynamic store separation simulations were not performed with the DES turbulence model because of difficulties within the solution that arose which could not be resolved. However, multiple DES static solutions were created and can compared against static results found with the B-L turbulence model.

The nature of DES, as an unsteady turbulence model, means that it is capable of predicting the large scale structures and turbulent fluctuations of the base flow region. Without history or any way of capturing the unsteady and non-linear characteristics

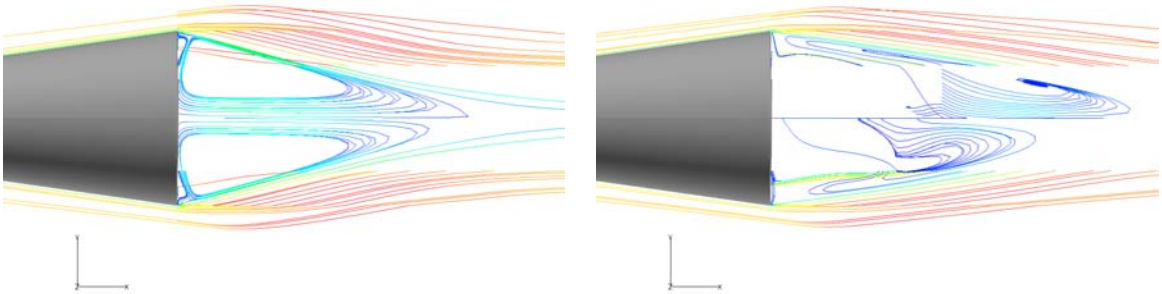

(a) Streamlines of Constant Mach (DES) (b) Streamlines of Constant Mach(B-L)

Figure 4.31: Streamlines of Mach at $\alpha = 0°$ using DES and B-L

of the base flow environment, the B-L model should not be used for detailed study of the near-wake.

Figure 4.31 demonstrates the stark difference between DES and B-L in defining the recirculation near wake region of the base. Streamlines of Mach have been provided on the x-y cut plane. The DES solution is given in Figure 4.31(a) and the B-L solution is given in Figure 4.31(b). Note the structured, symmetric, and ordered depiction of the recirculation region that DES provides compared to the asymmetry and poor recirculation definition of the B-L solution. The observed near wake flow field differences using DES and B-L are consistent with Simko's [29] work when contrasting DES and B-L solutions at the base region of a supersonic cone.

The impact on base pressure with the offset store base face configuration for the DES and B-L models is compared in Figure 4.32 along with the empirical and theoretical models predicting base pressure for a continuous base geometry (no offset or gap in base face). From the C_{PB} comparison plot, the DES model stays within the empirical and theoretical curves at the carrier base.

The B-L model shows increased base pressure at the carrier base, and both the DES and B-L models give higher pressure than the theoretical and empirical data

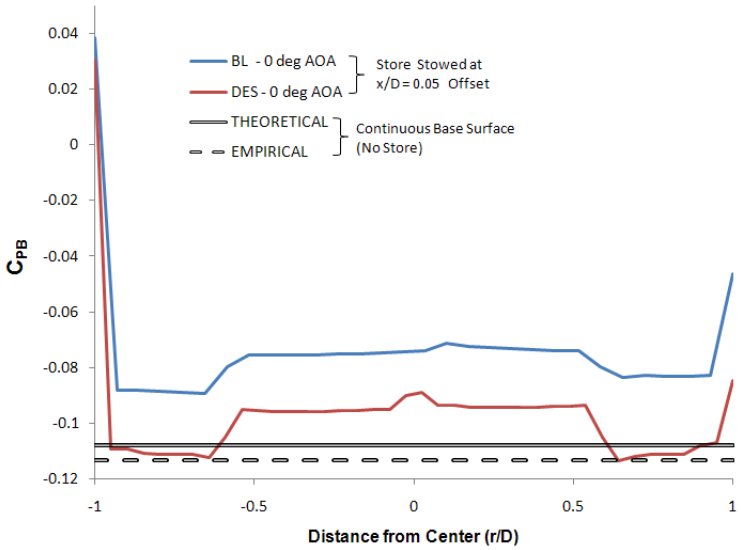

Figure 4.32: C_PB at $\alpha = 0°$ using DES and B-L

on the store face where it extends aft of the carrier base 5 mm. From this figure, it appears that the DES model better captures the base pressure at the carrier base than the B-L model in that it remains bounded by the empirical and theoretical models at the carrier base. This would imply that the DES model is probably a more accurate model to use for this type of study. However, as discussed in Section 4.3.3, there are geometric/computational differences between the theoretical/empirical solutions and the resulting data of this study that could account for differences in base pressure. Relative to the DES solution and the empirical and theoretical data, the B-L model results seem reasonable and fall fairly close to the rest of the data.

4.6 Impact of Store Initial Offset

The effect on drag and trajectory that a flush and offset base stowage configuration at an initial deployment orientation of $\alpha = 0°$ would have upon the separation simulation is addressed here. For both cases an ejection load of 15 G's was applied over a time period of .05 seconds for a ejection stroke length of x/D=0.39.

In Figure 4.33 the pressure profile on the base of the offset and flush carrier/-store system at 0° AOA is shown. Empirical and theoretical base pressure values

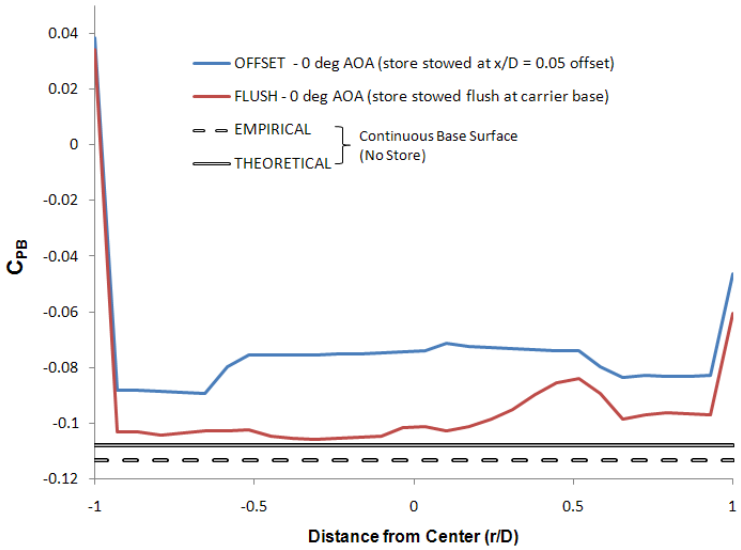

Figure 4.33: C_{PB} at $\alpha = 0°$ for Offset and Flush Carrier/Store Base Face

are provided for a identically shaped, continuous base geometry sphere cone body. Predictably, with the offset store, C_P on the store base region ($-.5 < r/D < .5$) is higher than for the flush store base face configuration. Interestingly, the offset case also shows a higher C_P on the carrier base region ($-.5 \leq r/D \geq .5$). As mentioned in Section 4.3.3 C_{PB} has some asymmetry acrosse the base. For the flush store stowage configuration, asymmetry in C_{PB} is particularily obvious compared to the offset case (albeit slight overall), and might point to some numerical error in the solution. In addition, the flush store stowage case shows a much closer match to empirical and theoretical C_{PB} values.

In Figures 4.34 and 4.35, carrier/store C_D and trajectory data is presented and compared. With the higher base pressure at ejection, C_D for the carrier for the offset case is notably lower than that of the flush case as shown in Figure 4.34(a). This allows the carrier to separate further away from the store during the separation event. Store C_D values remain close for the two cases with the store in the flush case showing a slightly higher drag just after it emerges from the near wake suction influence of the carrier body.

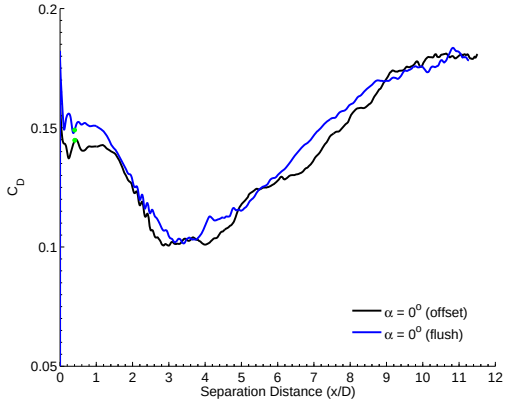

(a) Carrier C_D at $\alpha = 0$

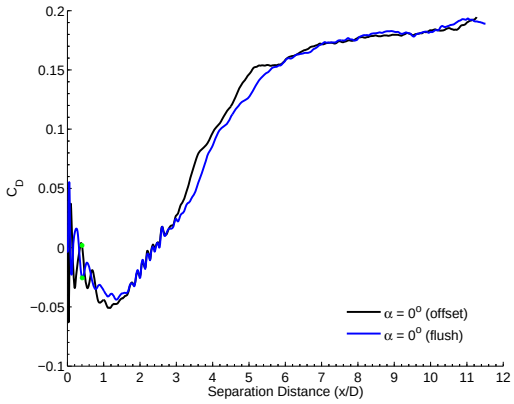

(b) Store C_D at $\alpha = 0$

Figure 4.34: C_D Comparison of Flush/Offset Store Stowage Configuration

Trajectory data for the carrier in Figure 4.35(a) shows that for both the offset and flush case, the carrier has reached a point of higher drag and begun to return back towards the point where separation occurred. As expected, the carrier with the initial flush store stowage configuration reaches a maximum separation distance first and begins to return at x/D = 8.72. With the lower drag experienced by the carrier in the initial offset store configuration, it travels out to an x/D = 9.15 before hitting a maximum drag and beginning to return backwards. The store trajectory information in Figure 4.35(b) shows the store in the offset configuration following almost identical trajectories. This is because the drag force acting on them is nearly the same. From the trajectory data, it can be seen that the offset configuration has a much greater effect on the distance traveled by the carrier than the distance traveled by the store, as compared to the flush store stowage configuration.

As touched on in Section 4.2, the reduced drag of the store offset stowage configuration as compared to the store flush stowage configuration is similar to effects obtained in which base drag can be reduced by modifying the aft base region of a projectile such that it converges towards the centerline at some angle. This is typically referred to as a boattail, and acts to increase mean base pressure, thus decreasing body drag. In Figure 4.36, striped Mach contours comparing the flush and offset store

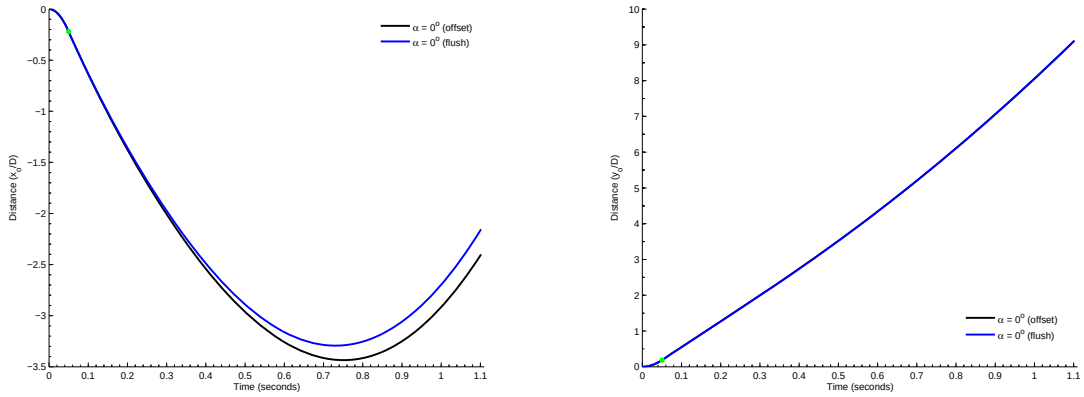

(a) Carrier Trajectory at $\alpha = 0$

(b) Store Trajectory at $\alpha = 0$

Figure 4.35: Trajectory Comparison of Flush/Offset Store Stowage Configuration

stowage configurations are shown so as to differentiate between the wake regions of the two cases.

It is immediately obvious that there are marked differences in the near wake region and shear layer location between the two flow solutions. Figure 4.36(a) shows the offset case with the shear layer displaced to a location immediately above the offset store base corner. Conversely, Figure 4.36(b) for the flush store stowage configuration shows the shear layer located off the carrier base corner as would be expected. The result is a sharper/stronger expansion for the flush store configuration.

Altering the store stowage placement such that the store base is displaced some distance aft of the carrier base has a relatively significant effect on the drag and trajectory of the two bodies upon store deployment. This would appear to be a plausible carrier/store configuration to use should a lower ejection force be required or if an increased margin of separation distance is needed for the aft ejection. The downside to an offset store stowage configuration is vehicle controllability, which is degraded as the boattail (or store in this case) is extended aft [11].

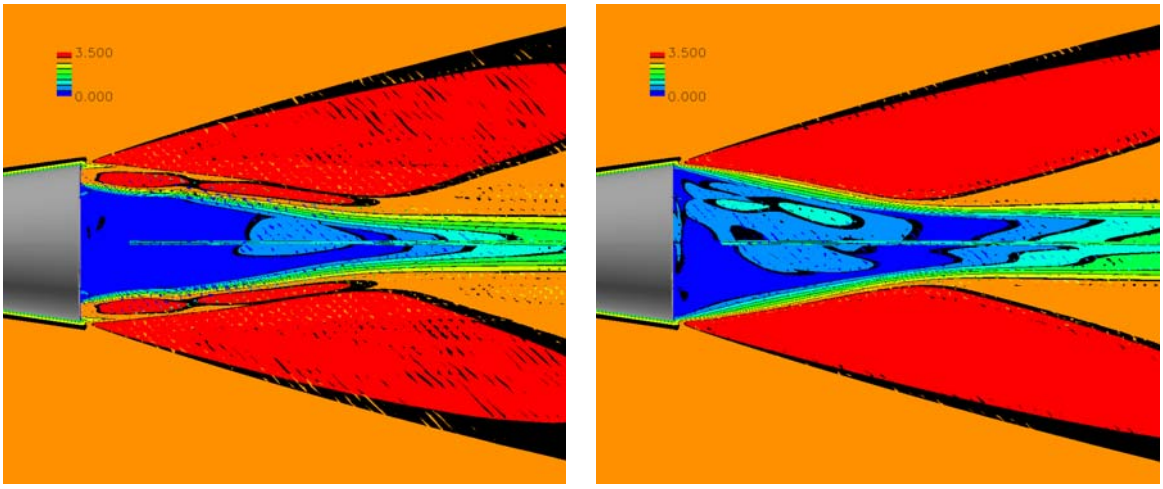

(a) Offset Store Stowage Configuration (b) Flush Store Stowage Configuration

Figure 4.36: Mach Contour Comparison of Offset Store Configuration vs. Flush Store Configuration

V. Conclusions and Future Work

5.1 Conclusions

Dynamic base store separation simulations at various conditions were successfully implemented using the Beggar CFD code with the Baldwin-Lomax algebraic turbulence model. In conjunction, key elements integral to modeling and understanding the physical characteristics of such an event were examined, including:

- derivation of body drag coefficients from static and dynamic solutions
- analysis of a failed separation simulation
- application of the DES turbulence model
- investigation into an alternative store stowage configuration

Base store separation simulations were implemented in a series of case studies through a range of flight path angles and AOA's. An 8.9° half cone angle was used for the carrier vehicle with an identically chaped store stowed within a cavity located in the aft section of the carrier body.Store separations were implemented at a free stream Mach of 2.9 with a Reynolds number of $Re = 6.9 \times 10^6/m$ referenced against carrier base diameter. Ejection loads of 7.5, 15 and 40 G's were applied in different test cases.

For all AOA cases, force contributions from gravity were neglected. The carrier/store two body system was not set to trimmed conditions before store ejection. For the AOA sweep, this resulted in a continuously damped wind driven pitching motion of the carrier and store, with an initial pitch angle magnitude directly related to the initial AOA.

Results indicated that an optimum separation was most likely to occur at $\gamma > 0°$ and at $\alpha > 0°$ for a safe store separation. At low flight path angles, the store had a tendency to stay submerged within the wake of the carrier, while the carrier would revert back towards the store once momentum from the separation event bled off. Likewise, at low AOA's, the store maintained it's position firmly within the carrier

wake, only slipping out of the wake at higher AOA's due to the pitching moment of the carrier. For $\alpha = 0^\circ$ and $\alpha = 2^\circ$ (15G ejection load), the carrier met an ejection force thrust/drag match and began to return in the direction of the retreating store towards the end of the simulation. At high AOA's, a necessary high 40G ejection force coupled with the store's immediate displacement out of the wake environment of the carrier indicated almost certain success as the separation progressed. The impact that such high ejection forces have on vehicle controllability as well as flight instrument and munition survival should be considered. In all cases, a characteristic store drag 'bucket' occurred showing a strong suction force toward the carrier at a position near the carrier base. In addition, the width of the drag bucket is directly correlated to the two body system's initial incidence to free stream upon store deployment.

At $\alpha = 0^\circ$, static solutions of the store and carrier were found at different fixed separation distances. Static carrier and store body force coefficients were decomposed into drag coefficients at each separation distance. These values were compared against the resultant free-motion dynamic solution at identical separation distances with $\alpha = 0^\circ$ after being subjected to a 15G ejection load. The static solutions were found to overestimate the carrier and store drag by as much as 141%. Furthermore, the static solution was unable to resolve the characteristic suction effect on the store that is seen in all the dynamic solutions. This was largely a result of the static solution computing a stronger expansion region at the base, thus decreasing pressure and increasing drag. It is apparent that for the case of an unconstrained dynamic separation, the flow field differs to such an extent that an equivalent static system will not accurately estimate the body forces experienced in the dynamic system.

An inadequate ejection force combined with an initial two-body incidence of $\alpha = 0^\circ$ provided the conditions for a failed store separation scenario, such that the store and carrier reconnected and impacted by the conclusion of the simulation. Drag profiles of the store and carrier show the store drag in a suction state for most of the separation and with two drag 'buckets' as the carrier initially separates from the store and then returns to the store. As opposed to the store suctioning into the carrier, the

carrier instead overtakes and impacts the store. Interestingly, the store stays so firmly positioned within the carrier wake, that it is effectively re-stowed perfectly within the carrier cavity by the end of the simulation.

The DES turbulence model was implemented on a statically stowed store/carrier configuration. Consistent with Simko's [29] results, the DES turbulence model produced a structured and symmetric recirculation region in the near wake environment, whereas the B-L turbulence model showed strong asymmetry in the recirculation region. Both turbulence models computed a mean base pressure that fell close to empirical and theoretical results. However, the B-L turbulence model showed itself to slightly overestimate the base pressure compared to that of the DES model and empirical and theoretical results. This indicates that DES might more accurately define the near wake and base region of a base flow problem, thus providing for a more accurate store separation scenario. This is not unexpected in that history effects and unsteady flow characteristics of the near wake environment cannot be resolved by the algebraic B-L turbulence model.

For all store separation simulations, the store is initially stowed such that its base is offset aft at x/D = 0.005 (5 mm) relative to the base face of the carrier. In order to gauge the effect that a flush store stowage configuration has upon the separation simulation compared to that of the offset store stowage configuration, separation simulations for each case were carried out at $\alpha = 0^{\circ}$ with identical ejection load specifications of 15G's. Somewhat surprisingly, when the store is initially offset x/D = 0.005, the two-body system enjoys increased mean base pressure and decreased drag similar to the affects of boattailing, where the aft base region of a projectile is modified with an angle relative to the forebody. Since the carrier's drag has been reduced at separation, it is able to travel further in the offset store stowage configuration than that of the flush store stowage configuration.

5.2 Future Work

Based on this research, there is much work that can be done to widen its scope and increase its depth. An important first step to take would be modifying the Beggar code such that a given separation event can be evaluated from an initially trimmed condition for the carrier/store system. This would provide for a more accurate 'real world' separation simulation event. In contrast, for the current research, the store is essentially being released at the height of an oscillatory pitching vehicle. Presently, Beggar is not capable of constraining the store relative to the carrier while it is allowed to move in free motion. This is critical in that as Beggar exists now, the store will move around within the carrier and either impact or slip out of the carrier base cavity as trim conditions are met. Code modification would probably be minimal since Beggar already allows for an array of body constraints relative to a fixed position. These constraints should be fairly straightforward to adapt to a relative moving position.

Separation simulations using the DES turbulence model could be implemented immediately with the latest version of Beggar. This would allow an in-depth investigation into the unsteady recirculation and near wake region of the base flow environment. In addition, results from the DES store separation cases could be compared and contrasted to the results from using the Baldwin-Lomax turbulence models. In order to achieve this, the computational domain as it exists now will probably have to be modified in order to take full advantage of DES. Likewise, an appropriately small time step is required so that unsteady turbulent effects are resolved.

Additional flush carrier/store base face stowage configuration separation simulation scenarios could also be implemented almost immediately with the newest version of Beggar. It would be interesting to see if the difference in drag and trajectory changes as sweep angle and AOA is adjusted. Also, higher initial AOA's could be introduced at separation to determine if performance trends continue as observed in the lower AOA cases.

Finally, experimentation with adjusting the static margin of the carrier vehicle might be attempted. Simulations where the static margin was adjusted so that C.G. fell behind the center of pressure on the carrier would provide insight into the resulting dynamics and flow environment of a store separation from a statically unstable carrier. Unfortunately, such testing comes with fairly high computational cost. With every adjustment of C.G. a new static solution must be generated and then used for the dynamic store separation simulation. For the current work (using ten 2.2GHZ processors in parallel), such an effort would have taken nearly 200 hrs of wall time to finish.

Appendix A. Reference Results

This chapter provides auxilary and addition reference information from the Chapter IV. All subject data is presented in the order it was given in the Chapter IV.

A.1 Flight Path Angle Sweeps

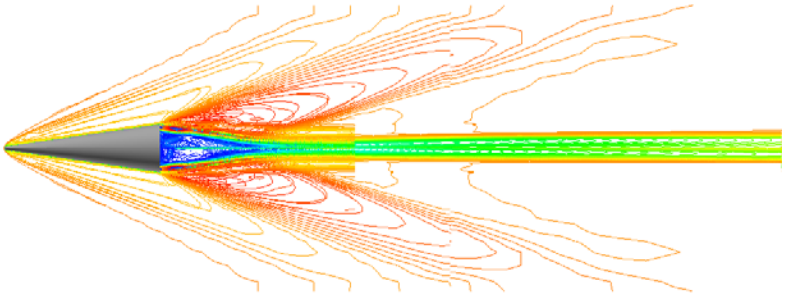

(a) x/D = 0 (time = 0.0 sec)

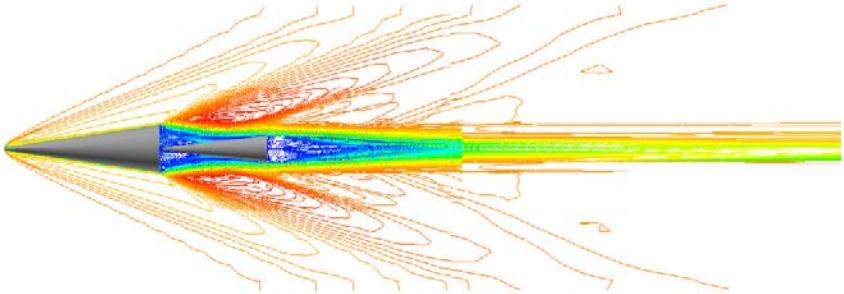

(b) x/D = 2.22 (time = 0.165 sec)

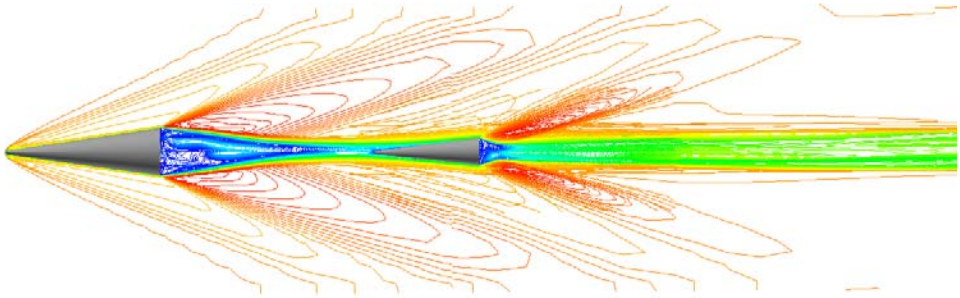

(c) x/D = 6.57 (time = 0.509 sec)

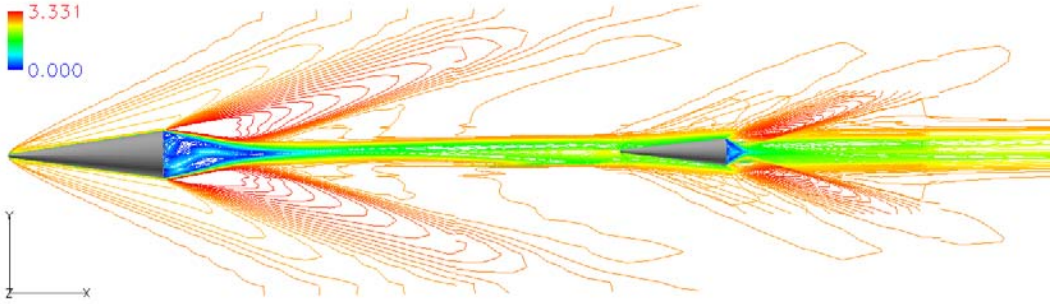

(d) x/D = 11.58 (time = 1.10 sec)

Figure A.1: Mach Contours at Various Separation Distances for $\gamma = 30^o$

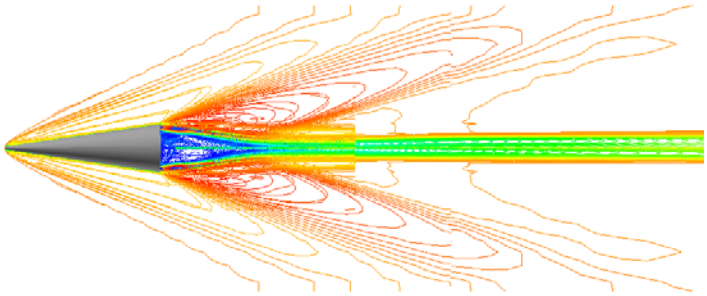

(a) x/D = 0 (time = 0.0 sec)

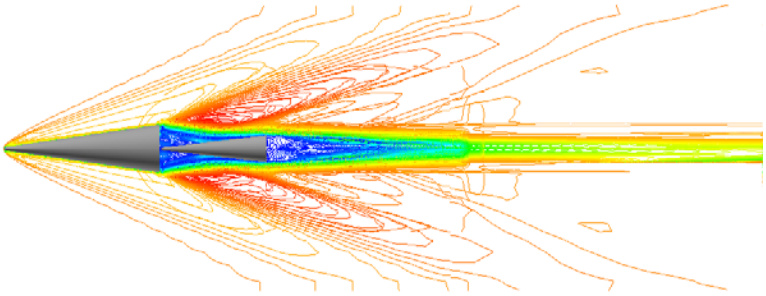

(b) x/D = 2.22 (time = 0.165)

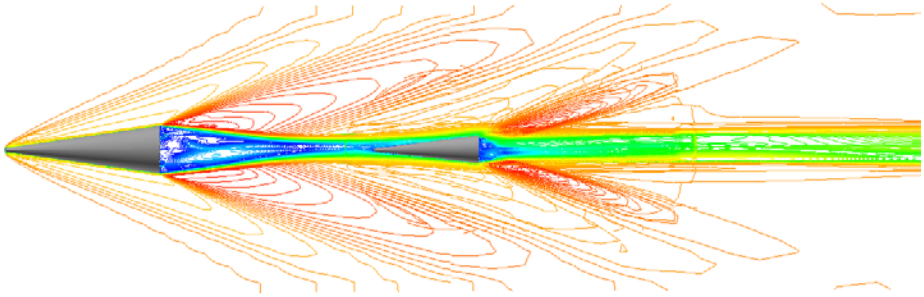

(c) x/D = 6.57 (time = 0.509 sec)

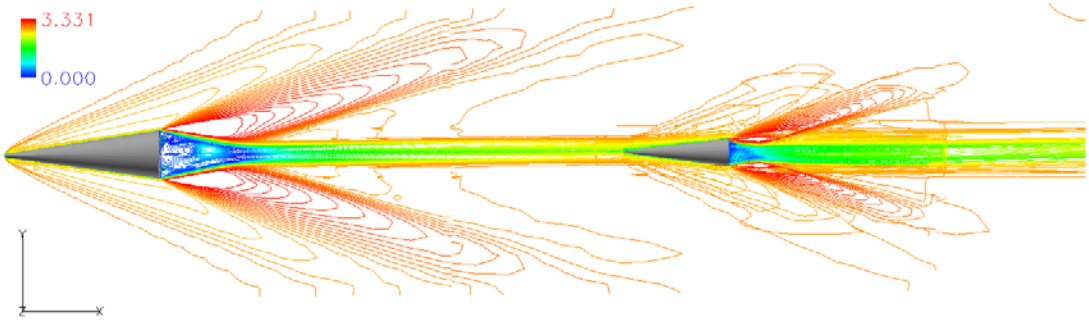

(d) x/D = 11.73 (time = 1.10 sec)

Figure A.2: Mach Contours at Various Separation Distances for $\gamma = 60^o$

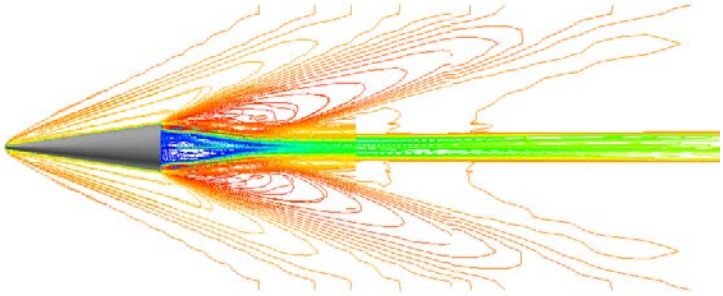

(a) x/D = 0 (time = 0.0 sec)

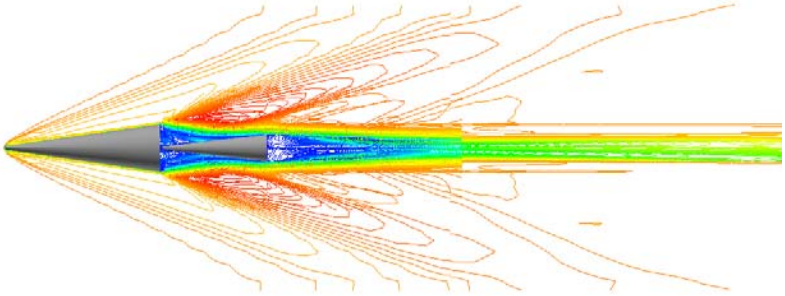

(b) x/D = 2.22 (time = 0.165)

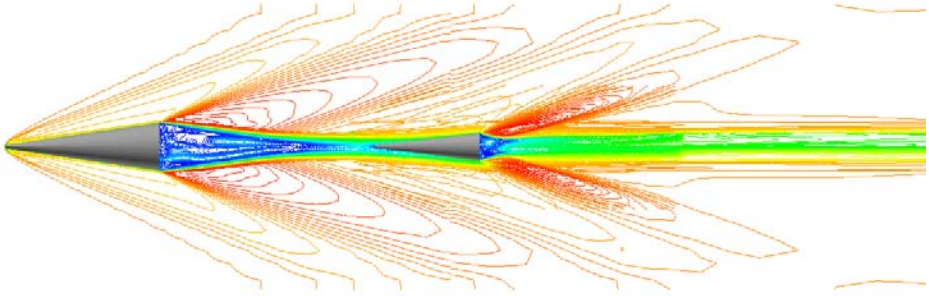

(c) x/D = 6.59 (time = 0.509 sec)

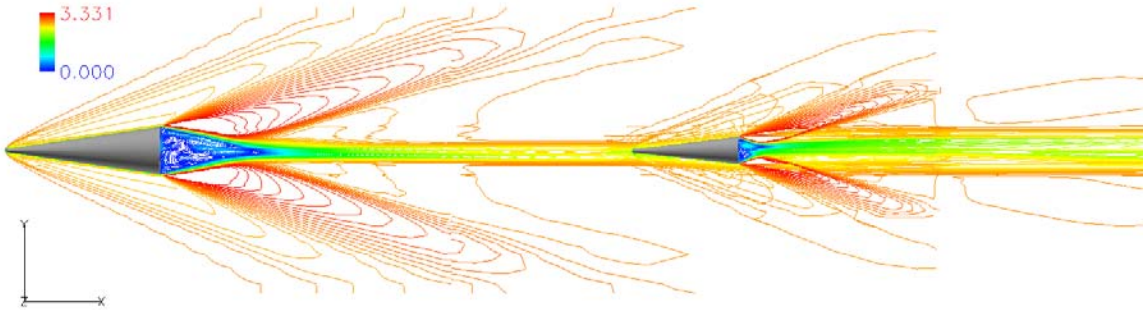

(d) x/D = 11.89 (time = 1.10 sec)

Figure A.3: Mach Contours at Various Separation Distances for $\gamma = 90^o$

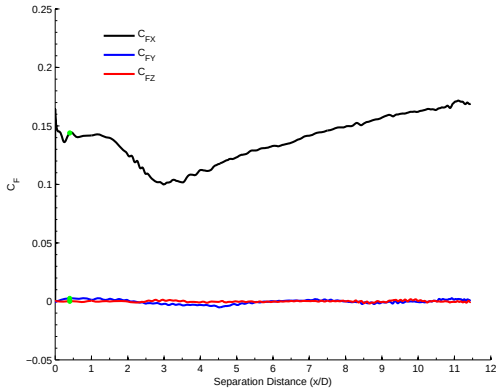

(a) Carrier C_F at $\gamma = 0^o$

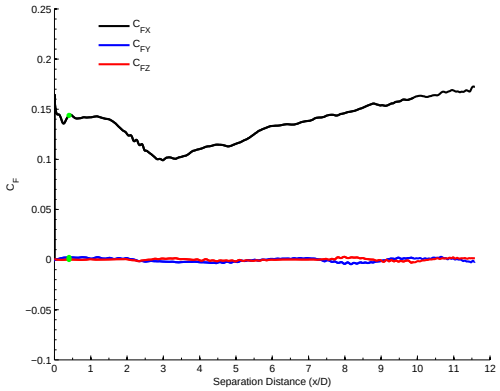

(b) Carrier C_F at $\gamma = 30^o$

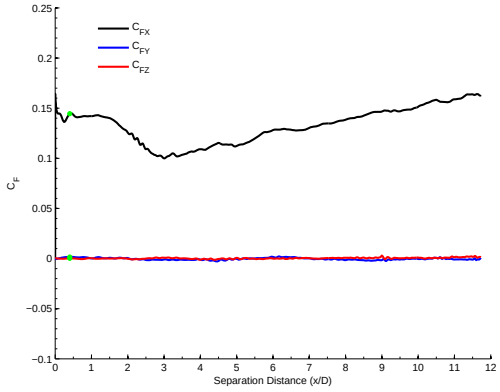

(c) Carrier C_F at $\gamma = 60^o$

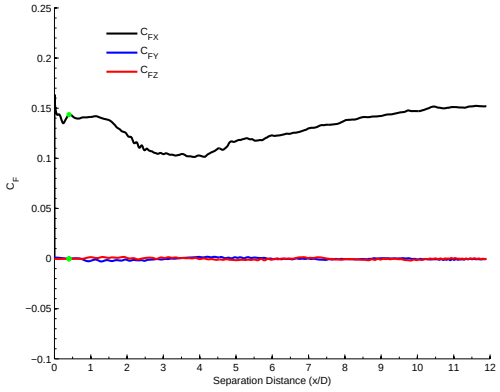

(d) Carrier C_F at $\gamma = 90^o$

Figure A.4: Carrier Force Coefficients at all $\gamma's$

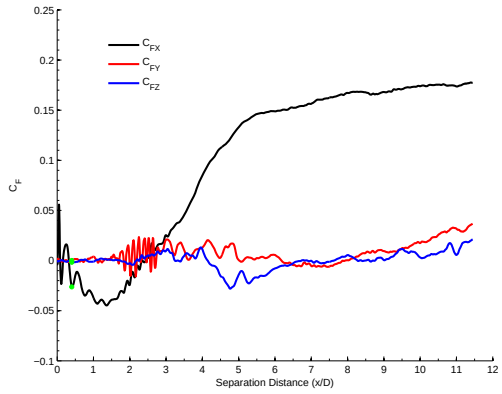

(a) Store C_F at $\gamma = 0^o$

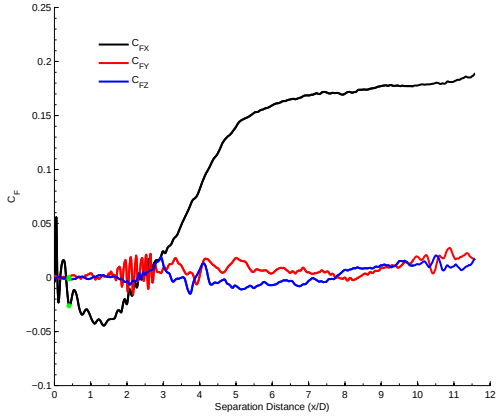

(b) Store C_F at $\gamma = 30^o$

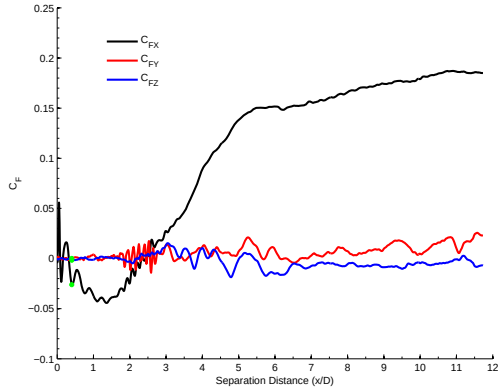

(c) Store C_F at $\gamma = 60^o$

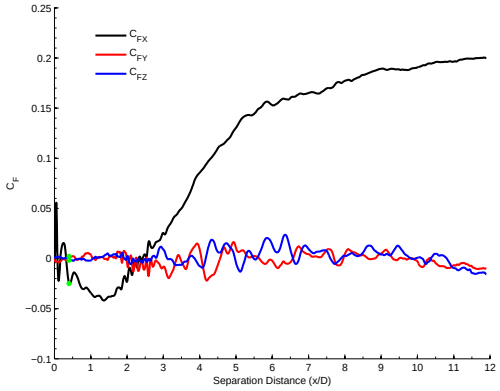

(d) Store C_F at $\gamma = 90^o$

Figure A.5: Store Force Coefficients at all $\gamma's$

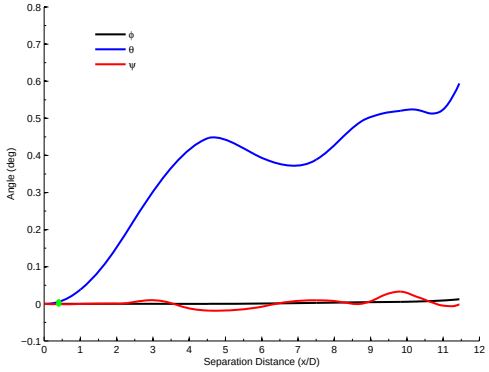

(a) Carrier Angular Movement $\gamma = 0^o$

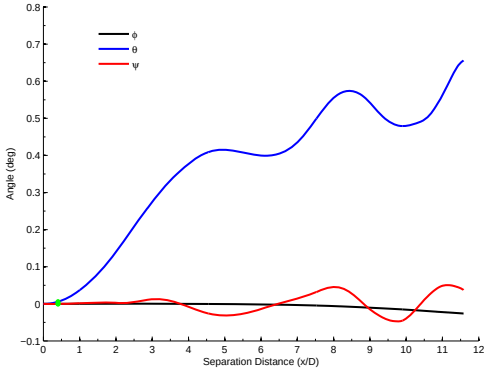

(b) Carrier Angular Movement $\gamma = 30^o$

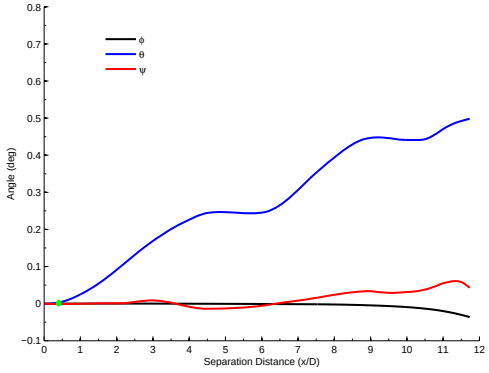

(c) Carrier Angular Movement $\gamma = 60^o$

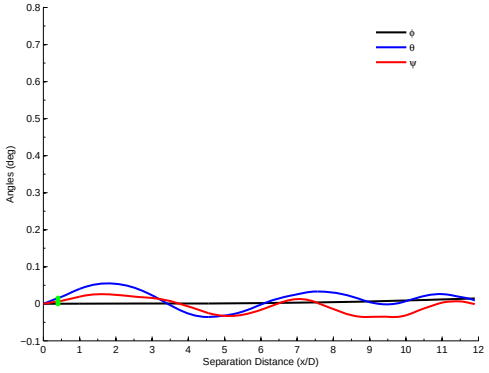

(d) Carrier Angular Movement $\gamma = 90^o$

Figure A.6: Relative Carrier Angular Movement

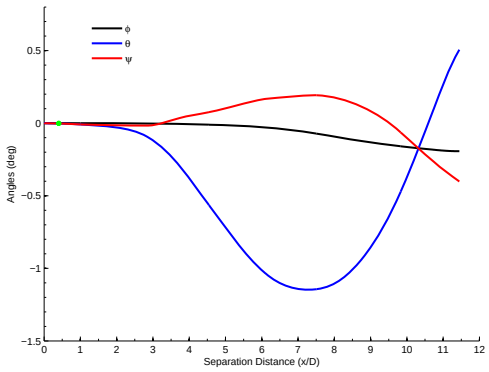

(a) Store Angular Movement $\gamma = 0^o$

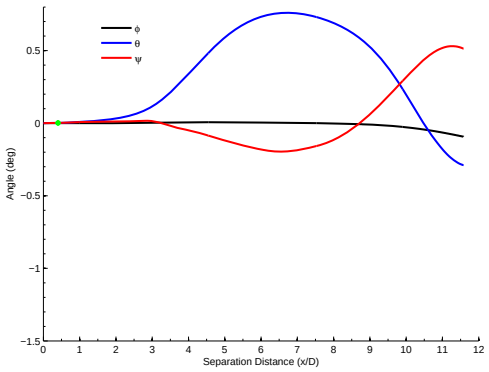

(b) Store Angular Movement $\gamma = 30^o$

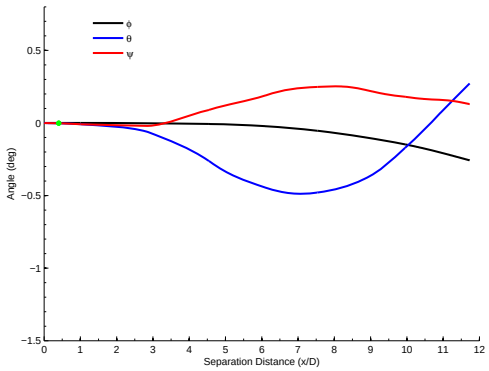

(c) Store Angular Movement $\gamma = 60^o$

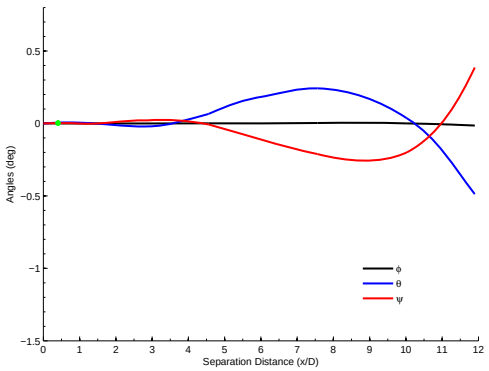

(d) Store Angular Movement $\gamma = 90^o$

Figure A.7: Relative Store Angular Movement

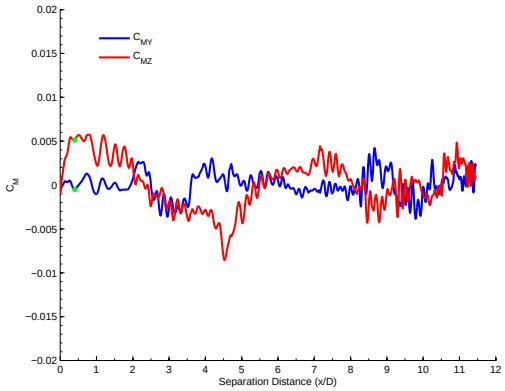

(a) Carrier C_M $\gamma = 0^o$

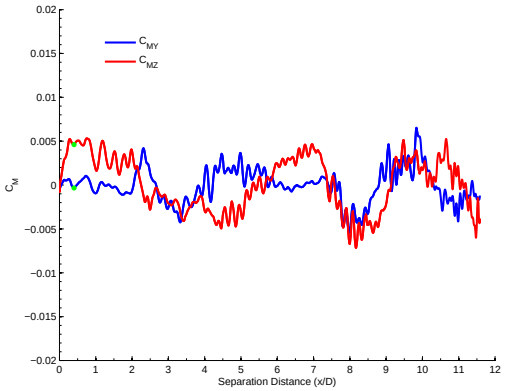

(b) Carrier C_M $\gamma = 30^o$

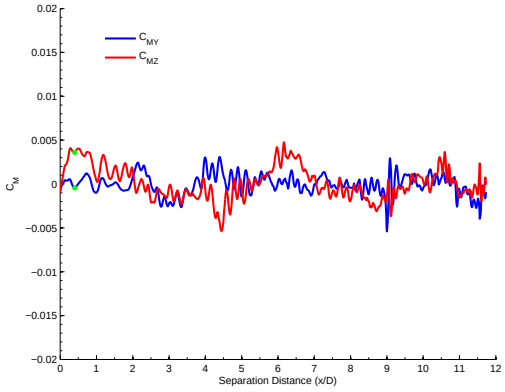

(c) Carrier C_M $\gamma = 60^o$

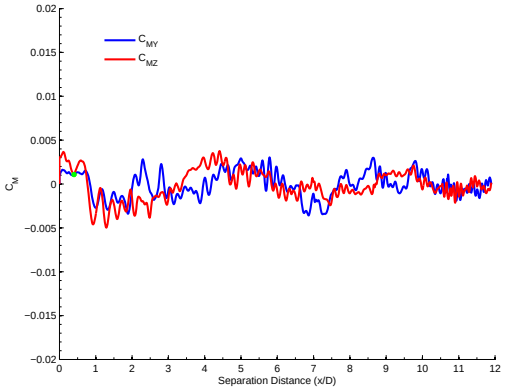

(d) Carrier C_M $\gamma = 90^o$

Figure A.8: Carrier Moment Coefficients $\gamma = 0^o, 30^o, 60^o, 90^o$

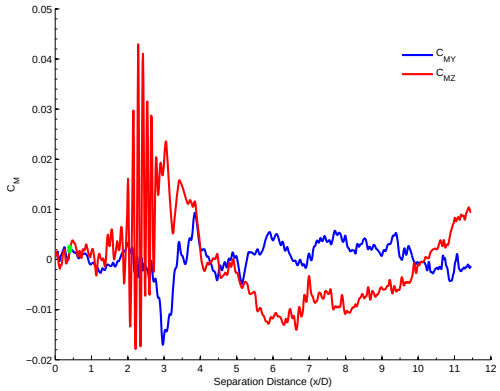

(a) Store C_M $\gamma = 0^o$

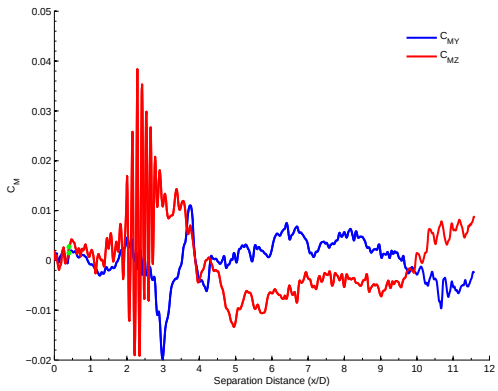

(b) Store C_M $\gamma = 30^o$

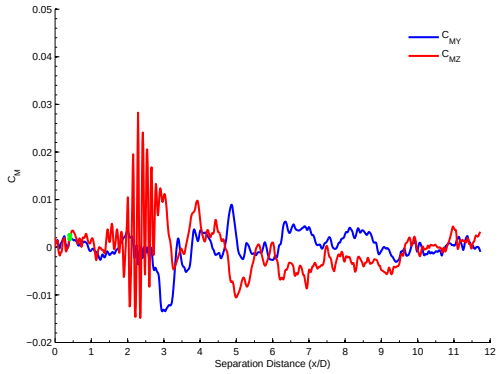

(c) Store C_M $\gamma = 60^o$

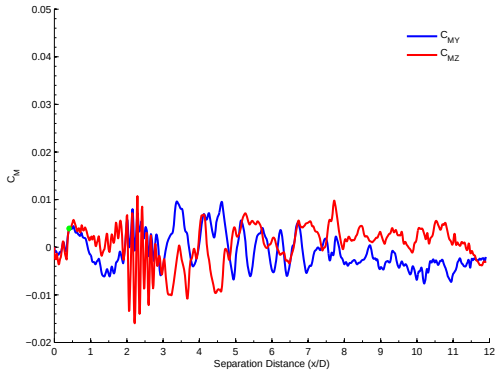

(d) Store C_M $\gamma = 90^o$

Figure A.9: Store Moment Coefficients $\gamma = 0^o, 30^o, 60^o, 90^o$

A.2 Low Angle of Attack Sweeps

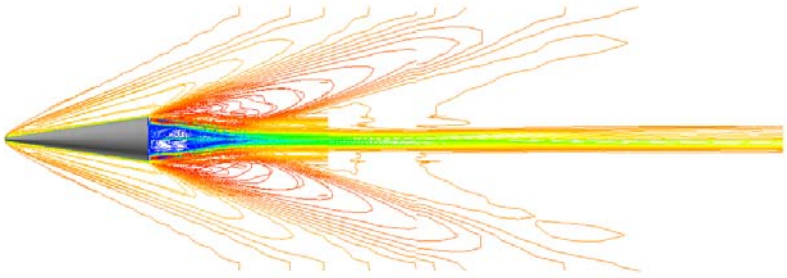

(a) x/D = 0 (time = 0.0 sec)

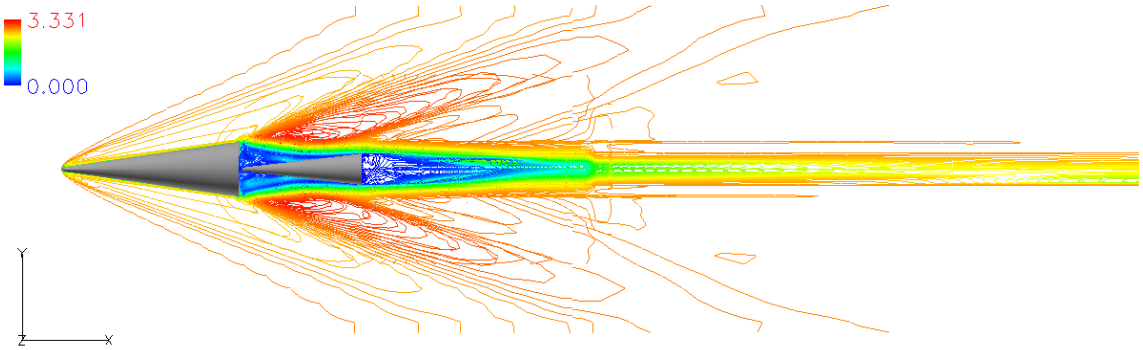

(b) x/D = 2.20 (time = 0.165 sec)

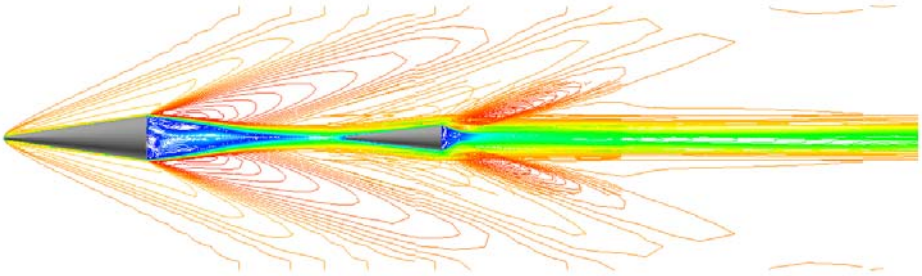

(c) x/D = 6.58 (time = 0.509 sec)

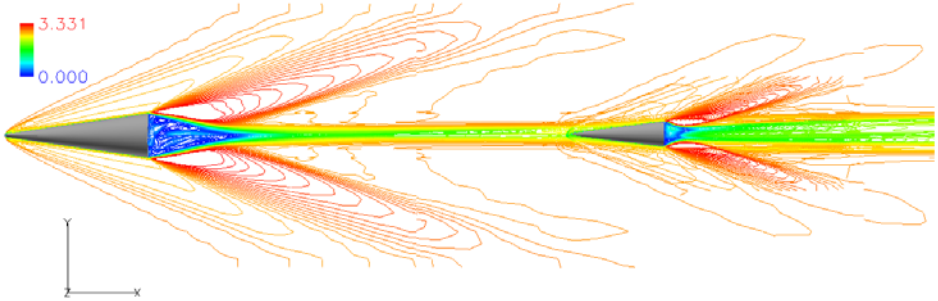

(d) x/D = 11.51 (time = 1.10 sec)

Figure A.10: Mach Contours at Various Separation Distances for $\alpha = 0^o$

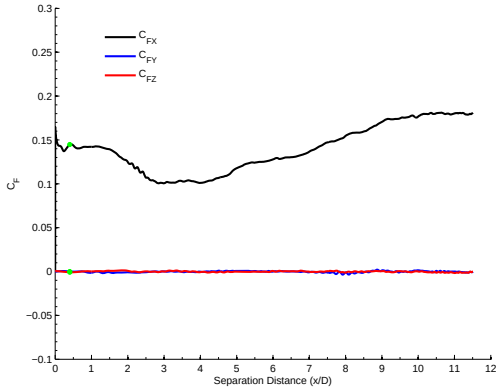

(a) C_F at $\alpha = 0^o$

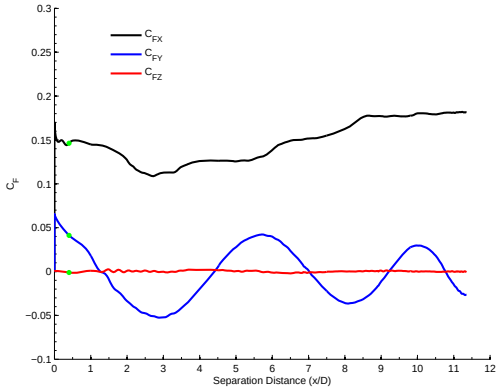

(b) C_F at $\alpha = 2^o$

Figure A.11: Carrier Force Coefficients at $\alpha = 0^o, 2^o$

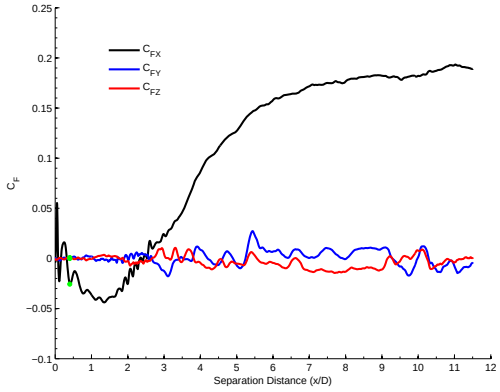

(a) C_F at $\alpha = 0^o$

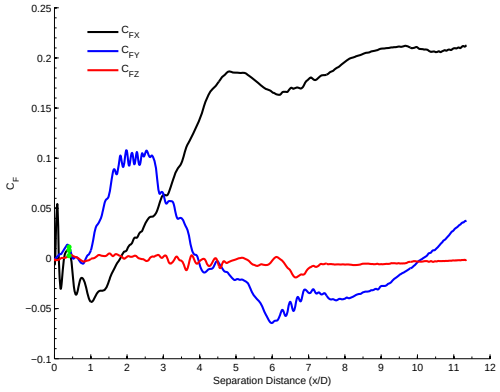

(b) C_F at $\alpha = 2^o$

Figure A.12: Store Force Coefficients at $\alpha = 0^o, 2^o$

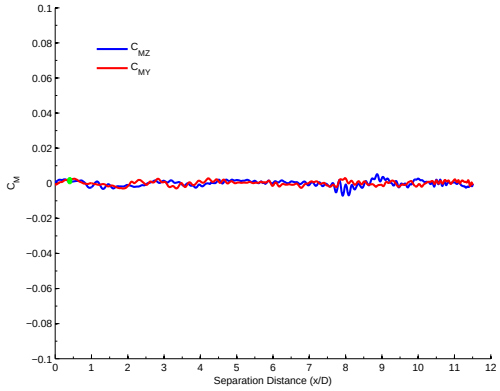

(a) C_M at $\alpha = 0^o$

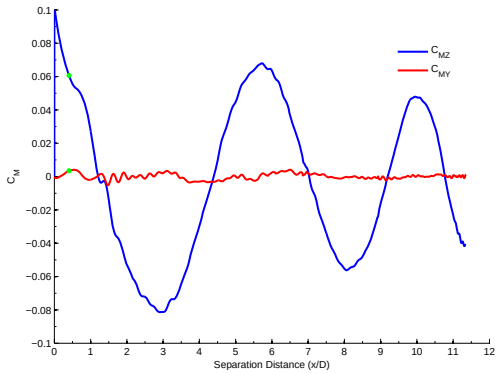

(b) C_M at $\alpha = 2^o$

Figure A.13: Carrier Moment Coefficients at $\alpha = 0^o, 2^o$

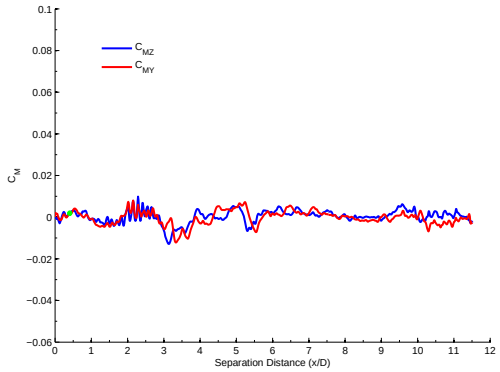

(a) C_M at $\alpha = 0^o$

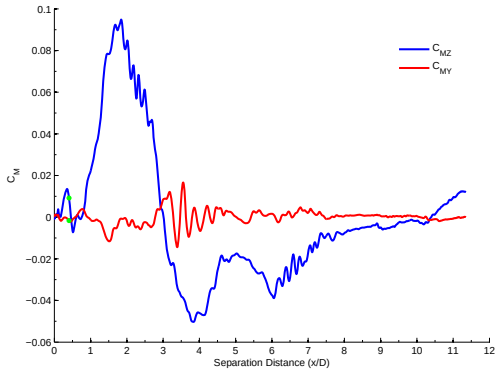

(b) C_M at $\alpha = 2^o$

Figure A.14: Store Moment Coefficients at $\alpha = 0^o, 2^o$

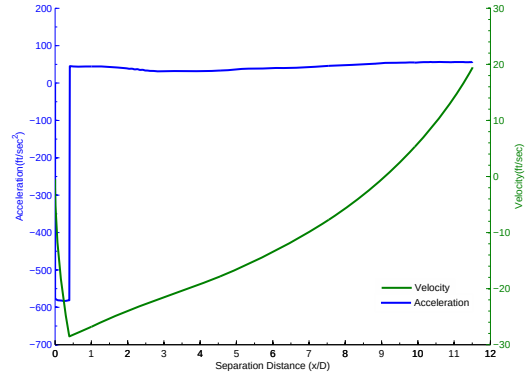

(a) Acceleration/Velocity at $\alpha = 0^o$

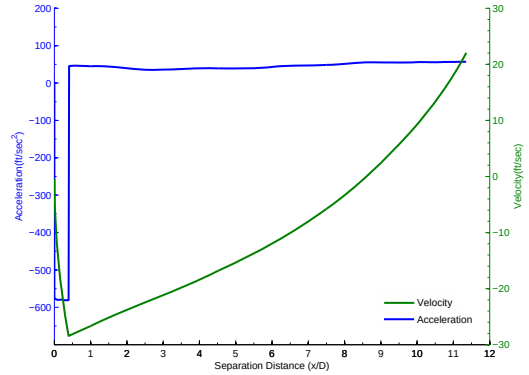

(b) Acceleration/Velocity at $\alpha = 2^o$

Figure A.15: Carrier Acceleration and Relative Velocity at $\alpha = 0^o, 2^o$

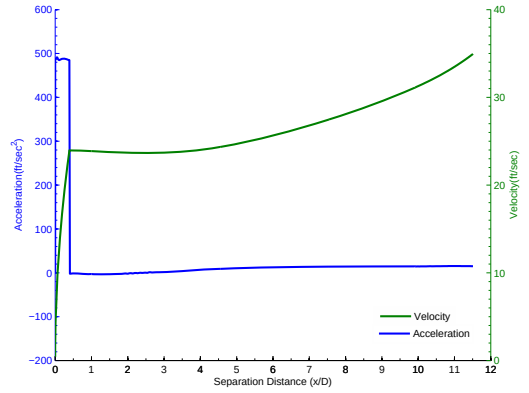

(a) Acceleration/Velocity at $\alpha = 0^o$

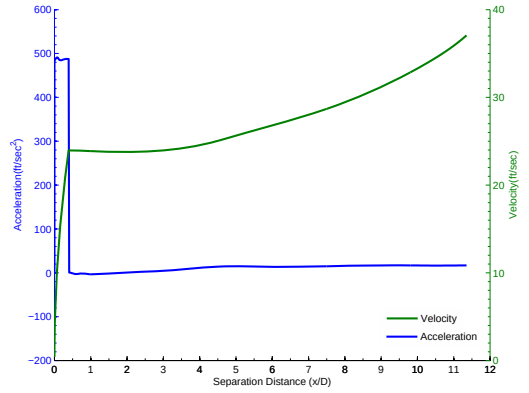

(b) Acceleration/Velocity at $\alpha = 2^o$

Figure A.16: Store Acceleration and Relative Velocity at $\alpha = 0^o, 2^o$

A.3 High Angle of Attack Sweeps

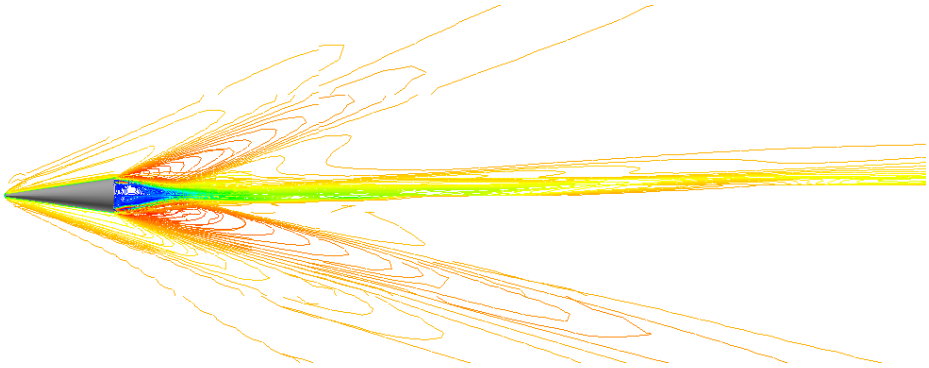

(a) x/D = 0 (time = 0.0 sec)

(b) x/D = 1.80 (time = 0.063 sec)

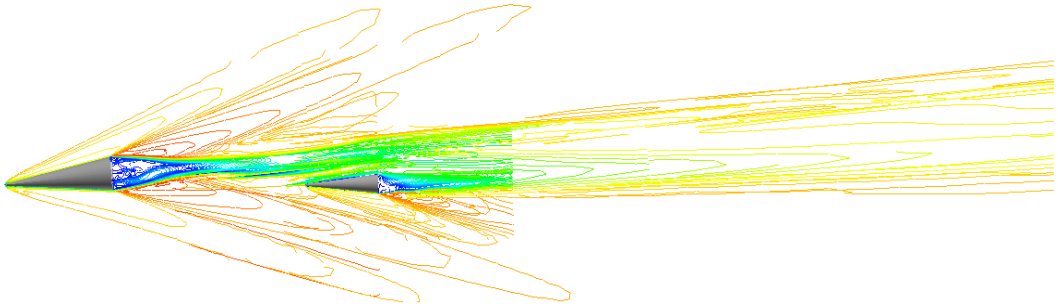

(c) x/D = 7.99 (time = 0.165 sec)

(d) x/D = 32.92 (time = 0.60 sec)

Figure A.17: Mach Contours at Various Separation Distances for $\alpha = 4^o$

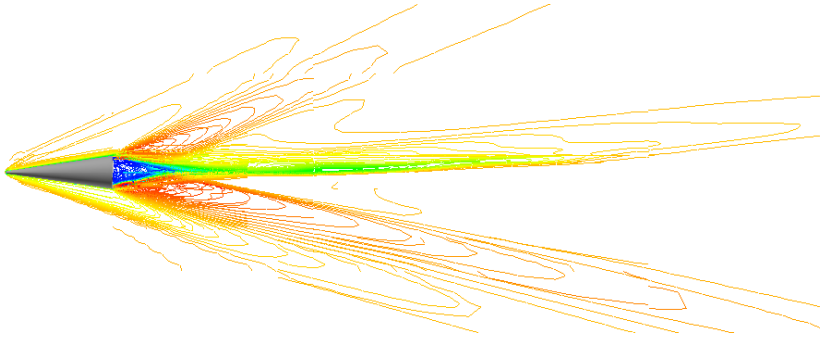

(a) x/D = 0 (time = 0.0 sec)

(b) x/D = 1.80 (time = 0.063 sec)

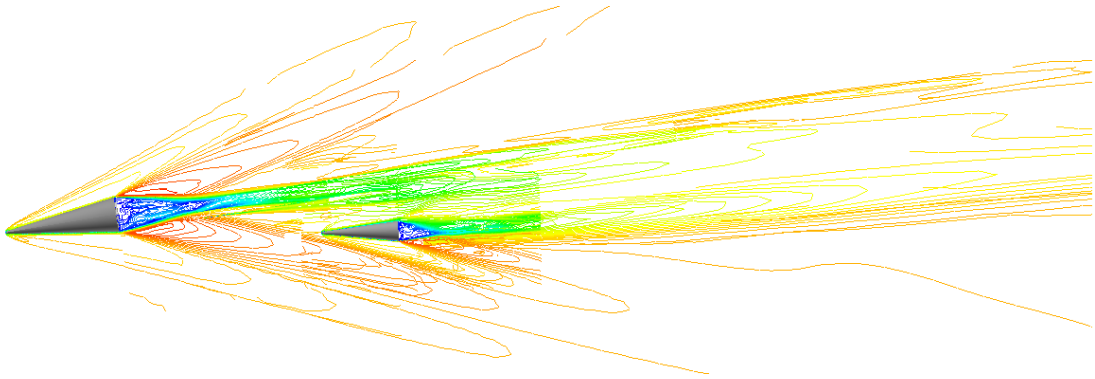

(c) x/D = 7.99 (time = 0.165 sec)

(d) x/D = 32.87 (time = 0.60 sec)

Figure A.18: Mach Contours at Various Separation Distances for $\alpha = 6^o$

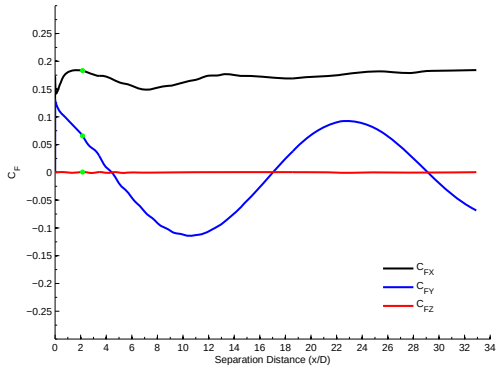

(a) Carrier C_F at $\alpha = 4^o$

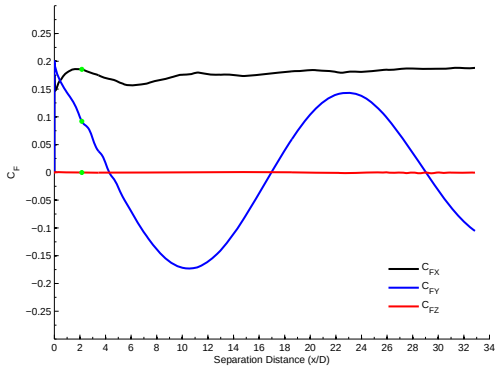

(b) Carrier C_F at $\alpha = 6^o$

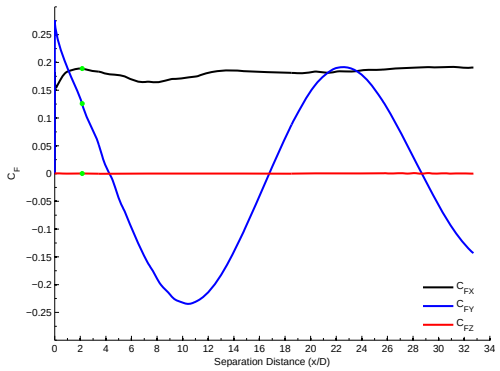

(c) Carrier C_F at $\alpha = 8^o$

Figure A.19: Carrier Force Coefficients at $\alpha = 4^o, 6^o, 8^o$

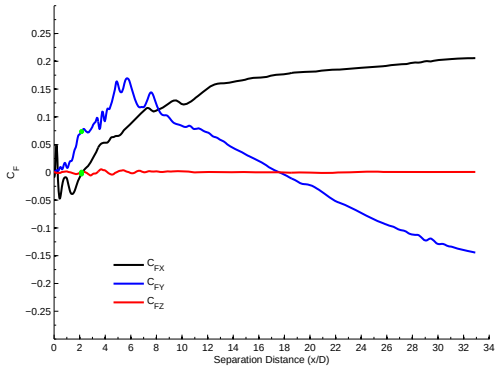

(a) Store C_F at $\alpha = 4^o$

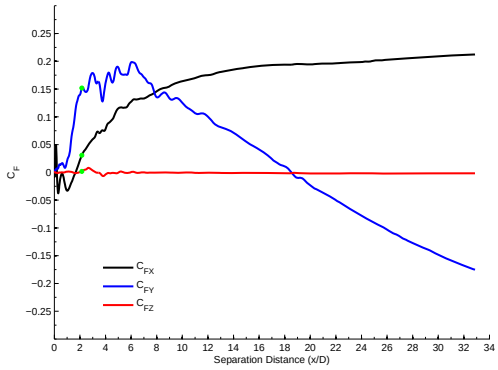

(b) Store C_F at $\alpha = 6^o$

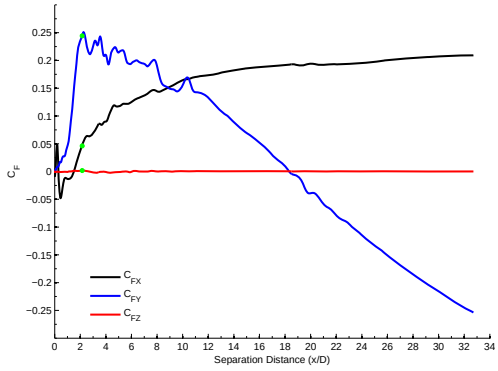

(c) Store C_F at $\alpha = 8^o$

Figure A.20: Store Force Coefficients at $\alpha = 4^o, 6^o, 8^o$

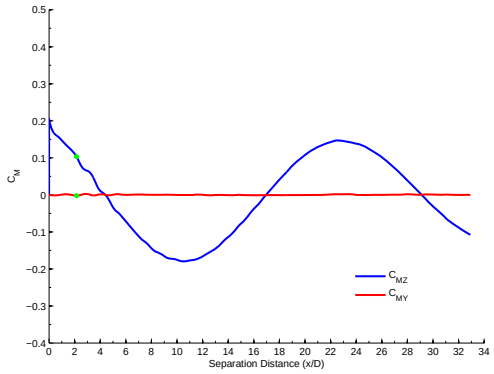

(a) Carrier C_M at $\alpha = 4^o$

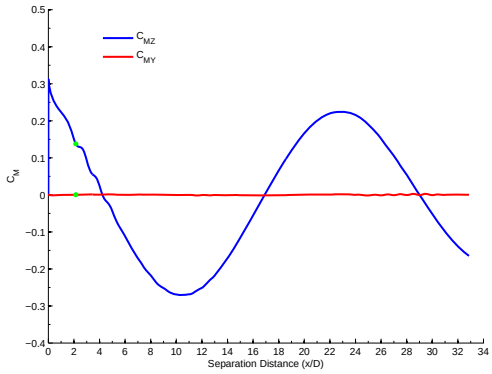

(b) Carrier C_M at $\alpha = 6^o$

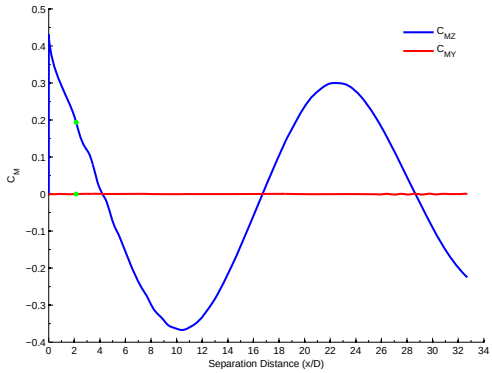

(c) Carrier C_M at $\alpha = 8^o$

Figure A.21: Carrier Moment Coefficients at $\alpha = 4^o, 6^o, 8^o$

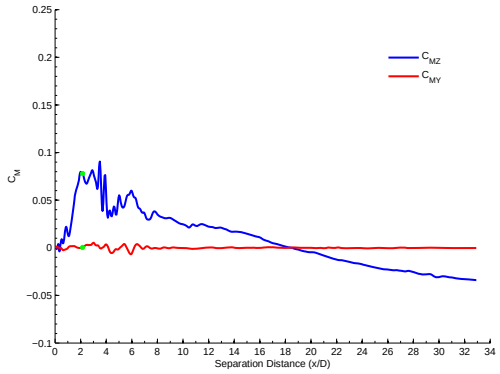

(a) Store C_M at $\alpha = 4^o$

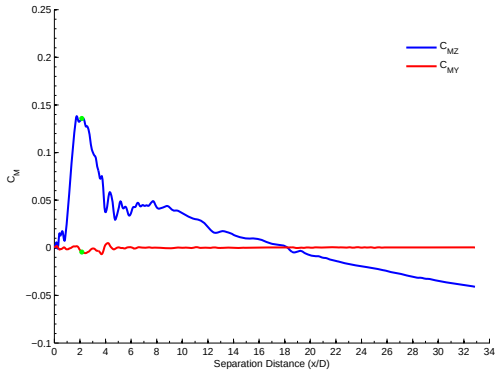

(b) Store C_M at $\alpha = 6^o$

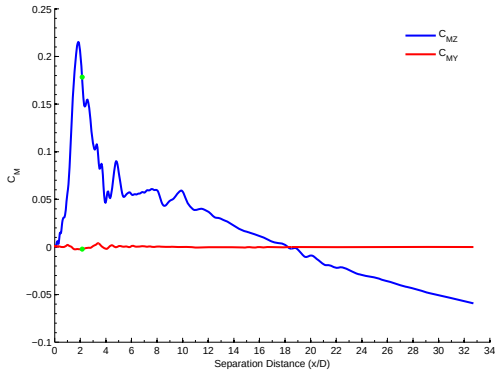

(c) Store C_M at $\alpha = 8^o$

Figure A.22: Store Moment Coefficients at $\alpha = 4^o, 6^o, 8^o$

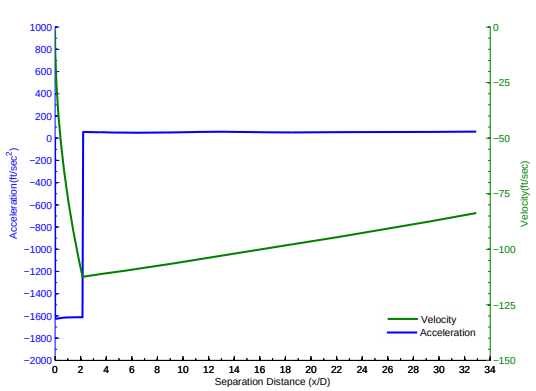

(a) Acceleration/Velocity at $\alpha = 4^o$

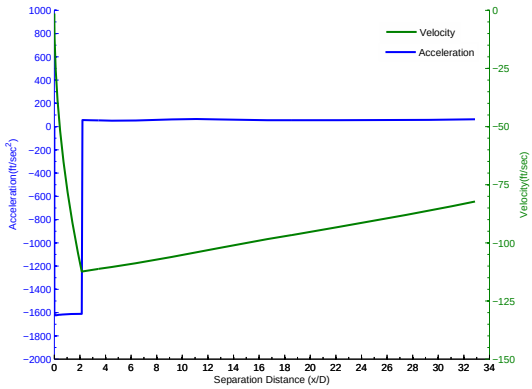

(b) Acceleration/Velocity at $\alpha = 6^o$

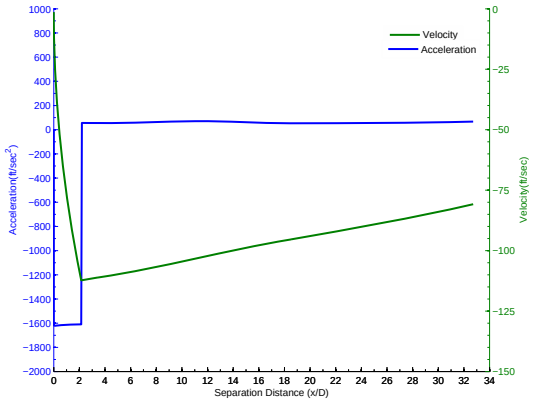

(c) Acceleration/Velocity at $\alpha = 8^o$

Figure A.23: Carrier Acceleration and Relative Velocity at $\alpha = 4^o, 6^o, 8^o$

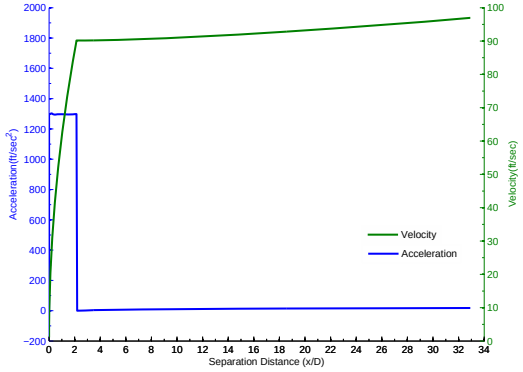

(a) Acceleration/Velocity at $\alpha = 4^o$

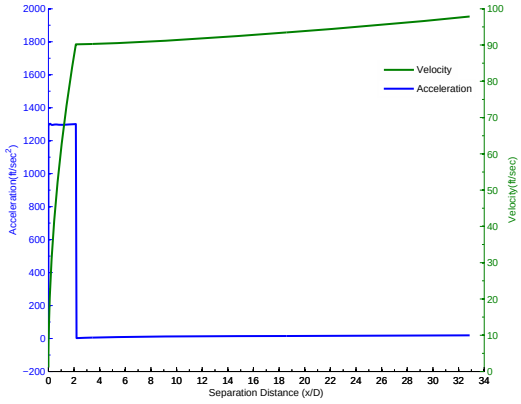

(b) Acceleration/Velocity at $\alpha = 6^o$

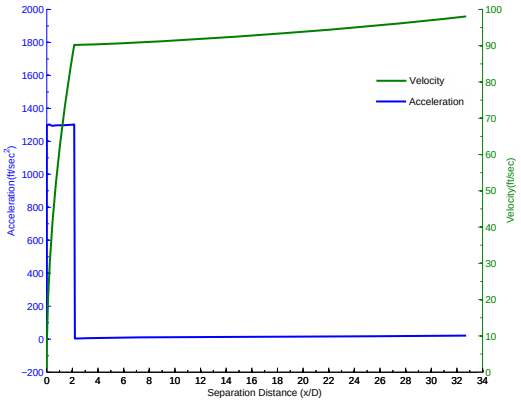

(c) Acceleration/Velocity at $\alpha = 8^o$

Figure A.24: Store Acceleration and Relative Velocity at $\alpha = 4^o, 6^o, 8^o$

Appendix B. Beggar Input Files

Representative Beggar input files and auxilary files necessary to perform the store separation simulations are provided in this Appendix.

B.1 Static RV Input File

```
#_____________________________________________________________
#
#                    INITIALIZATION PARAMETERS
#_____________________________________________________________

verbose = 1
ptol = 1e-8
nopatch

inner_tol = 1.e-08
inner_tol_ratio = 1.e+4

#Set AOA here in degrees
# rot z -4.0

#_____________________________________________________________
#
#                    FLOW PROPERTIES
#           (Ref. Beggar Manual, Chapter 4, para. 1)
#_____________________________________________________________

mach = 2.9
gamma = 1.4

#Re at 60,000 ft at M 2.9
reynolds = 6933950

#_____________________________________________________________
#
#                     SIX+DOF PARAMETERS
#         (Ref. Beggar Manual, Chapter 5, para. 4 & 5)
#_____________________________________________________________

sixdof gravity = <0,-32.17,0>  #ft/s^2
sixdof density = .000223874  # slug/ft^3
sixdof soundspd = 967.84776  #ft/sec
sixdof refl = 3.281  #meters/ft
```

```
#_____________________________________________________________
#
#                    DYNAMIC CASE PRE-CHECK
#             (Ref. Beggar Manual, Chapter 5, para. 17)
#
#_____________________________________________________________
#

 dt=0.0001
 dtiter = 1
 inner = 80

#_____________________________________________________________
#
#                       FLOW SOLVER PARAMETERS
#                   (Ref. Beggar Manual, Chapter 7)
#_____________________________________________________________
#

# Choose turb model: BL or DES

# BL Turbulence Model
 stencil=viscous2
 solver=second order, full, viscous baldwin_lomax,
      steg_warm_xair jacobians,
      implicit bcupdate, primitive extrap,
      steger_warming right_side,
      implicit viscous_k, implicit viscous_j,
implicit viscous_i

# DES Turbulence Model
# kinit=0.099
# stencil=viscous2
#  solver=second order, full, viscous spalart,
#     detchd_edd_sim,
#     steg_warm_xair jacobians,
#     implicit bcupdate, primitive extrap,
#     steger_warming right_side,
#     implicit viscous_k, implicit viscous_j,
#     implicit viscous_i
```

```
#  BC update weighting
   bcrelax = 1.0              # default = 1.0
   block to block relax = 0.4   # default = 0.4

# Set iteration to apply char BC's fully
  ngrad = 20

#-----------------------------------------------------------------
#                        Body Grids
#-----------------------------------------------------------------


#get grid definitions for carrier body
 include "../beg/aeroshell_merged_extended.beg"

#get grid definitions for interface grid
 include "../beg/big_interface.beg"

#get grid definitions for store body
 include "../beg/store.beg"

#pos store body .005 m offset from carrier base within cavity
 trans 1.030,0,0

#-----------------------------------------------------------------
#
#                SET WORLDSIDE FOR CCUT OPTIONS
# (Ref. Beggar Manual, Chapter 8, para. 6)
#-----------------------------------------------------------------

sb 1
 g 1
  set (1,1,1) (2,2,2) to worldside

#-----------------------------------------------------------------
#
#                      FORCE SPEC
#
#-----------------------------------------------------------------
#

###### Aeroshell #####
```

```
forcespec "aeroshell_loads": dump every 1 to
    "aeroshell_forces.dat" as ascii with noheader
         with refl = 1.0  #meters
         with refa = .7854  #meters^2
         with mcenter = <0.542,0,0>  #meters
forcespec "aeroshell_loads": add "shell"

###### Store #####

forcespec "store_loads": dump every 1 to
    "store_forces.dat" as ascii with noheader
          with refl = 0.575  #meters
    with refa = .2597  #meters^2
    with mcenter = <2.288,0,0>   #meters
forcespec "store_loads": add "store"
```

B.2 Dynamic RV Input File

```
#_____________________________________________________________
#
#                   INITIALIZATION PARAMETERS
#_____________________________________________________________

verbose = 1
ptol = 1e-8
nopatch

inner_tol = 1.e-08
inner_tol_ratio = 1.e+4

#_____________________________________________________________
#
#                   FLOW PROPERTIES
#           (Ref. Beggar Manual, Chapter 4, para. 1)
#_____________________________________________________________

mach = 2.9
gamma = 1.4

#Re at 60,000 ft at M 2.9
reynolds = 6933950

#_____________________________________________________________
```

```
#
#                     SIX+DOF PARAMETERS
#          (Ref. Beggar Manual, Chapter 5, para. 4 & 5)
#_____________________________________________________________

sixdof gravity = <0,-32.17,0>  #ft/s^2
sixdof density = .000223874  # slug/ft^3
sixdof soundspd = 967.84776  #ft/sec
sixdof refl = 3.281  #meters/ft

#_____________________________________________________________
#
#                    DYNAMIC CASE PRE-CHECK
#             (Ref. Beggar Manual, Chapter 5, para. 17)
#
#_____________________________________________________________
#

#global dt for time-accurate runs
#increase dtiter for store separation simulation
 dt=.25
 dtiter = 5
 inner = 100

#_____________________________________________________________
#
#                       FLOW SOLVER PARAMETERS
#                   (Ref. Beggar Manual, Chapter 7)
#_____________________________________________________________
#

# BL Turbulence Model
 stencil=viscous2
 solver=second order, full, viscous baldwin_lomax,
      steg_warm_xair jacobians,
      implicit bcupdate, primitive extrap,
      steger_warming right_side,
      implicit viscous_k, implicit viscous_j,
implicit viscous_i


#  BC update weighting
   bcrelax = 1.0              # default = 1.0
```

```
   block to block relax = 0.4   # default = 0.4

#-----------------------------------------------------------------
#                        Body Grids
#-----------------------------------------------------------------
#         Apply alternate grid definitions with no flow
#         initialization paramters
#-----------------------------------------------------------------

#get grid definitions for carrier body
 include "../beg/aeroshell_merged_extended_motion.beg"

#get grid definitions for interface grid
 include "../beg/big_interface_motion.beg"

#get grid definitions for store body
 include "../beg/store_motion.beg"

#pos store body completely in cavity
 trans 1.030,0,0

#_________________________________________________________________
#
#                SET WORLDSIDE FOR CCUT OPTIONS
# (Ref. Beggar Manual, Chapter 8, para. 6)
#_________________________________________________________________

sb 1
 g 1
  set (1,1,1) (2,2,2) to worldside

#_________________________________________________________________
#
#                      FORCE SPEC
#
#_________________________________________________________________
#

###### Aeroshell #####

forcespec "aeroshell_loads": dump every 1 to
    "aeroshell_forces.dat" as ascii with noheader
         with refl = 1.0  #meters
```

```
         with refa = .7854  #meters^2
         with mcenter = <0.542,0,0>  #meters
forcespec "aeroshell_loads": add "shell"

###### Store #####

forcespec "store_loads": dump every 1 to
    "store_forces.dat" as ascii with noheader
          with refl = 0.575  #meters
    with refa = .2597  #meters^2
    with mcenter = <2.288,0,0>   #meters
forcespec "store_loads": add "store"

#_____________________________________________________________________
#
#                      DYNAMIC SPEC
#
#_____________________________________________________________________


###### Aeroshell #####

dynamicspec 'aeroshell':
add fspec 'aeroshell_loads';
add sb 'shell';
mass = 23.963;  #slugs
ixx = 27.378; iyy = 349.72; izz = 349.72;  #slug/ft^2
ixy = 0.0; iyz = 0.0; ixz =0.0;
cg = <1.778,0,0>;  #ft
dump idaps left release;
dump gandc z down;
trelease = 0.0;
read gandc z down gviz;

add force with
components = <-1.0,0.0,0.0>,
location = <3.297,0,0>,  #ft
duration = 0.05, #seconds
const_magnitude = 15000,  #LBS!
system = local


###### Store #####
```

```
dynamicspec 'store':
add fspec 'store_loads';
add sb 'store';
mass = 30.809; #slugs
ixx = 6.255; iyy = 115.065; izz = 115.065; #slug/ft^2
ixy = 0.0; iyz = 0.0; ixz =0.0;
cg = <7.506,0,0>;  #ft
dump idaps left release;
dump gandc z down;
trelease = 0.0;
read gandc z down gviz;

add force with
components = <1.0,0.0,0.0>,
location = <4.891,0,0>, #ft
duration = 0.05, #seconds
const_magnitude = 15000, #LBS!
system = local
```

B.3 Auxilary Beggar Files

The grid definition files and typical time ramping schedule are provided here. Note that in the grid definition files, various grid regions in the near wake base flow regime are initialized to subsonic flow. This was done to eliminate problems early in the flow solution as the sharp expansion flow angle and recirculation area was resolved. For any dynamic or separation simulations, the initalization regions in the grid definition files are removed as seen in section B.2.

B.3.1 Carrier Grid Definitions.

```
directory prefix = '../grids/'
readgrids 'cone_cav_merged_fifteen.p3df' as plot3d ascii
tag 'shell_SB'

g 1
   set "shell" = (1,1,1) (*,1,*) to noslip
g 2
   set "shell" += (1,1,1) (*,1,*) to noslip
```

```
g 3
   set "shell" += (1,1,1) (*,1,*) to noslip
g 4
   set "shell" += (1,1,1) (*,1,*) to noslip
g 7
   set "shell" += (1,1,1) (1,*,*) to noslip
   init (1,1,1) (60,*,*) using mach = 0.25
g 9
   set "shell" += (1,1,1) (1,*,*) to noslip
   init (1,1,1) (60,*,*) using mach = 0.25
g 11
   set "shell" += (1,1,1)(1,*,*) to noslip
   init (1,1,1) (60,*,*) using mach = 0.25
g 13
   set "shell" += (1,1,1) (1,*,*) to noslip
   init (1,1,1) (60,*,*) using mach = 0.25
g 26
   set "shell" += (1,*,1) (150,*,*) to noslip
   set "shell" += (1,1,1) (1,*,*) to noslip
   init (1,1,1)(230,*,*) using mach = 0.25
g 27
   set "shell" += (1,*,1) (150,*,*) to noslip
   set "shell" += (1,1,1) (1,*,*) to noslip
   init (1,1,1)(230,*,*) using mach = 0.25
g 28
   set "shell" += (1,*,1) (150,*,*) to noslip
   set "shell" += (1,1,1) (1,*,*) to noslip
   init (1,1,1)(230,*,*) using mach = 0.25
g 29
   set "shell" += (1,*,1) (150,*,*) to noslip
   set "shell" += (1,1,1) (1,*,*) to noslip
   init (1,1,1)(230,*,*) using mach = 0.25
```

B.3.2 Store Grid Definitions.

```
directory prefix = '../grids/'
readgrids 'store.p3df' as plot3d ascii
tag 'store_SB'

g 1
   set "store" = (1,1,1) (*,1,*) to noslip
   init (1,1,1)(*,55,*) using mach = 0.25
g 2
   set "store" += (1,1,1) (1,*,*) to noslip
```

```
   init (1,1,1) (60,*,*) using mach = 0.25
g 3
   init (1,1,1) (60,60,*) using mach = 0.25
g 4
   set "store" += (1,1,1) (*,1,*) to noslip
   init (1,1,1)(*,55,*) using mach = 0.25
g 5
   set "store" += (1,1,1) (1,*,*) to noslip
   init (1,1,1) (60,*,*) using mach = 0.25
g 6
   init (1,1,1) (60,60,*) using mach = 0.25
g 7
   set "store" += (1,1,1) (*,1,*) to noslip
   init (1,1,1)(*,55,*) using mach = 0.25
g 8
   set "store" += (1,1,1) (1,*,*) to noslip
   init (1,1,1) (60,*,*) using mach = 0.25
g 9
   init (1,1,1) (60,60,*) using mach = 0.25
g 10
   set "store" += (1,1,1) (*,1,*) to noslip
   init (1,1,1)(*,55,*) using mach = 0.25
g 11
   set "store" += (1,1,1) (1,*,*) to noslip
   init (1,1,1) (60,*,*) using mach = 0.25
g 12
   init (1,1,1) (60,60,*) using mach = 0.25
```

B.3.3 Interface Grid Definitions.

```
directory prefix = '../grids/'
readgrids 'big_interface.p3df' as plot3d ascii
tag 'interface'

g 1
  init (1,1,1) (*,*,*) using mach = 0.25
g 2
  init (1,1,1) (*,*,*) using mach = 0.25
g 3
  init (1,1,1) (*,*,*) using mach = 0.25
g 4
  init (1,1,1) (*,*,*) using mach = 0.25
```

B.3.4 Time Step Ramp Schedule.

```
apply_at_iter = 200
dt = 0.001
apply_at_iter = 600
dt = 0.01
apply_at_iter = 800
dt = .1
apply_at_iter = 1000
dt = 1
apply_at_iter = 1200
dt = 10

dump plot3d every 3000
dump restart every 3000
```

Bibliography

1. Private conversation with Steven W. Lingenfelter, October 9, 2007.

2. Babcock, J. T. *Free Flight Store Simulation Using Beggar*. Master's thesis, Graduate School of Engineering, Air Force Institute of Technology (AFIT), 2006.

3. Blazek, J. *Computational Fluid Dynamics: Principles and Applications*. Elsevier Ltd, Kidlington, Oxford, second edition, 2005.

4. Bulmer, B. M. "Flight-Test Base Pressure Measurements in Turbulent Flow". *Journal of Aircraft*, Vol 14, No 12:1783-1785, 1976.

5. Butler, G., D. King, G. Abate, and M. Stephens. "Ballistic Range Tests of Store Separation at Supersonic to Hypersonic Speeds". *29th Aerospace Sciences Meeting*. AIAA Paper 1991-0199, Reno, NV, January 1991.

6. Chapman, D. R. *An Analysis of Base Pressure at Supersonic Velocites and Comparison with Experiment*. Technical Report 1051, NACA, 1951.

7. Dutton, J. C., J. L. Herrin, M. J. Molezzi, T. Mathur, and K. M. Smith. "Recent Progress on High Speed Separated Base Flows". *33rd Aerospace Sciences Meeting and Exhibit*. AIAA Paper 1995-0472, Reno, NV, January 1995.

8. Erengil, M. E., D. S. Dolling, J. Pike, and W. G. Reinecke. "The Aerodynamics of Tandom Bodies at Mach 5 Part I: Preliminary Experimental Results". *33rd Aerospace Sciences Meeting and Exhibit*. AIAA Paper 1995-0319, Reno, NV, January 1995.

9. Fureby, C., Y. Nilsson, and K. Andersson. "Large Eddy Simulation of Supersonic Base Flow". *37th AIAA Aerospace Sciences Meeting and Exhibit*. AIAA Paper 1999-0426, Reno, NV, January 1999.

10. Herrin, J. L. and J. C. Dutton. "Supersonic Base Flow Experiments in the Near-Wake of a Cylindrical Aferbody". *24th AIAA Fluid Dynamics Conference*. AIAA Paper 1993-2785, Orlando, FL, July 1993.

11. Janssen, J. R. and J. C. Dutton. "Time-Series Analysis of Supersonic Base Pressure Fluctuations". *AIAA Journal*, Vol 42, No. 3, March 2004.

12. J.Sahu and K. R. Heavey. "Numerical Investigation of Supersonic Base Flow with Base Bleed". *AIAA Atmospheric Flight Mechanics Conference*. AIAA Paper 1995-3459, Washington, DC, August 1995.

13. Jung, T. P., M. F. Reeder, R. C. Maple, and J. Crafton. "Wind Tunnel Study of Interference Effects Relating to Aft Supersonic Ejection of a Store". *AIAA 36th Fluid Dynamics Conference and Exhibit*. AIAA Paper 2006-3363, San Francisco, CA, June 2006.

14. Lamb, J. P. and W. L. Oberkampf. "A Review and Development of Correlations for Base Pressure and Base Heating in Supersonic Flow". *Prepared by Sandia National Laboratories*, 1993.

15. Lin, T. C., L. K. Sproul, M. Kim, M. Olmos, and H. Feiz. "Hypersonic Reentry Vehicle Wake Flow Fields at Angle of Attack". *AIAA 44th Aerospace Sciences Meeting and Exhibit*. AIAA Paper 2006-582, Reno, Nevada, January 2006.

16. Newman, G., K. Fulcher, R. Ray, and M. Pinney. "On the Aerodynamics/Dynamics of Store Separation from a Hypersonic Aircraft". *AIAA 10th Applied Aerodynamics Conference*. AIAA Paper 1992-2722, Palo Alto, CA, June 1992.

17. Nichols, R. "Turbulence Models and Their Application to Complex Flows". Contract no. N62306-01-D-7110.

18. Ober, C. C., J. P. Lamb, and T. M. Kiehne. "A Computational Study of the Aerodynamics of a Body Immersed in a Supersonic Wake". *AIAA Atmospheric Flight Mechanics Conference*. AIAA Paper 1994-3519, Scottsdale, AZ, August 1994.

19. Ober, C. C., J. P. Lamb, and W. G. Reinecke. "The Aerodynamics of Tandem Bodies at Mach 5 Part II: Computational Results". *33rd AIAA Aerospace Sciences Meeting and Exhibit*. AIAA Paper 1995-0320, Reno, NV, January 1995.

20. Prewitt, N. C., D. M. Belk, and R. C. Maple. "Multiple-Body Trajectory Calculations Using the Beggar Code". *AIAA Journal*, Vol 36, No. 5, September-October 1999.

21. van Raalte, M. H. and B. W. van Oudheusden. "An Analytical Model to Describe the Reynolds Number Effects in Supersonic Base Flow". *31st AIAA Fluid Dynamics Conference and Exhibit*. AIAA Paper 2001-2785, Anaheim, CA, June 2001.

22. Raymer, D. P. *Aircraft Design: A Conceptual Approach*. AIAA, Inc., Reston, VA, third edition, 1999.

23. Regan, Frank J. *Re-Entry Vehicle Dynamics*. AIAA, Inc., New York, NY, first edition, 1984.

24. Richie, G. "The Common Aero Vehicle: Space Delivery System of the Future". *AIAA Space Technology Conference*. AIAA Paper 1999-4435, Albuquerque, NM, September 1999.

25. Rizk, M., S. Ellison, and J. M. Lee. "Beggar Code Implementation of the (6+)DOF Capability for Stores with Moving Components". *42nd AIAA Fluid Aerospace Sciences Meeting and Exhibit*. AIAA Paper 2004-1251, Reno, NV, January 2004.

26. Rizk, M., S. Ellison, and N. C. Prewitt. "Beggar - A Store Separation Predictive Tool". *32nd AIAA Fluid Dynamics Conference and Exhibit*. AIAA Paper 2002-3190, St. Louis, MO, June 2002.

27. Sahu, J. and C. J. Neitubicz. *A Computational Study of Cylindrical Segments in the Wake of a Projectile*. Technical Report Technical Report BRTL-TR-3254, Ballistic Research Laboratory Aberdeen Proving Ground, MD, 1991.

28. Sahu, J. and C. J. Neitubicz. *Applications of Chimera Technique to Projectiles in Relative Motion*. Technical Report AIAA Paper, 1993-3632, U.S. Army Research Laboratory Aberdeen Proving Ground, MD, 1993.

29. Simko, R. J. *Store Separations from a Supersonic Cone*. Master's thesis, Graduate School of Engineering, Air Force Institute of Technology (AFIT), 2006.

30. Tannehil, J. C., D. A. Anderson, and R. H. Pletcher. *Computational Fluid Dynamics and Heat Transfer*. Taylor & francis, Washington, DC, second edition, 1997.

31. Team, Computational Aeromechanics. *Beggar Version 117+ User's Manual*. Air Force Seek Eagle Office, Eglin AFB, FL, December 2006.

32. Vatsa, V. N., J. L. Thomas, and B. W. Wedan. "Navier Stokes Computations of a Prolate Spheroid at Angle of Attack". *Journal of Aircraft*, Vol.26, No.11 (986-993), 1989.

33. White, F. M. *Viscous Fluid Flow*. McGraw-Hill, Inc., New York, New York, second edition, 1991.

34. Young, D. D. and D. B. Goldstein. "A Study of Unsteady Hypersonic Segmented Projectile Aerodynamics". *14th Computational Fluid Dynamnics Conference*. AIAA Paper 1999-3379, Norfolk, VA, June 1999.

REPORT DOCUMENTATION PAGE

Form Approved
OMB No. 0704–0188

1. REPORT DATE (DD–MM–YYYY)	2. REPORT TYPE	3. DATES COVERED *(From — To)*
16-12-2008	**Master's Thesis**	Aug 2007 – Dec 2008

4. TITLE AND SUBTITLE

Dynamic Supersonic Base Store Ejection Simulation Using Beggar

5a. CONTRACT NUMBER

5b. GRANT NUMBER

5c. PROGRAM ELEMENT NUMBER

6. AUTHOR(S)

Michael D. Johnson

5d. PROJECT NUMBER

5e. TASK NUMBER

5f. WORK UNIT NUMBER

7. PERFORMING ORGANIZATION NAME(S) AND ADDRESS(ES)
Air Force Institute of Technology
Graduate School of Engineering and Management (AFIT/ENY)
2950 Hobson Way
WPAFB OH 45433-7765

8. PERFORMING ORGANIZATION REPORT NUMBER

AFIT/GAE/ENY/08-D01

9. SPONSORING / MONITORING AGENCY NAME(S) AND ADDRESS(ES)

N/A

10. SPONSOR/MONITOR'S ACRONYM(S)

11. SPONSOR/MONITOR'S REPORT NUMBER(S)

12. DISTRIBUTION / AVAILABILITY STATEMENT

Approval for public release; distribution is unlimited.

13. SUPPLEMENTARY NOTES

14. ABSTRACT

Static and dynamic conditions throughout various aft supersonic store separation events are examined using the Beggar Computational Fluid Dynamics (CFD) code from Air Force SEEK Eagle Office at Eglin Air Force Base, FL. An 8.9^{o} half angle sphere cone is used for the carrier vehicle with an identically shaped store stowed within a hollow compartment in the aft section of the carrier body. Dynamic store separation simulations are implemented at a free-stream Mach of 2.9 with a Reynolds number of $Re = 6.9x10^{6}$/m referenced against carrier base diameter. Analysis covers multiple dynamic separation events along with studies of the carrier/store body at various static conditions and configurations. Dynamic store separation simulations show that a successful store separation is more likely to occur at high angles of attack and high flight angles. When a low angle of attack and low flight angle are combined with inadequate ejection forces, it appears that the carrier and store will eventually impact each other due to the tendency of the store to remain within the low drag wake region of the carrier. For all dynamic separation cases, a suction effect or negative drag forces is observed acting on the store as it separates through the near wake region of the carrier body. The duration of the suction effect is found to be directly related to the initial free stream incidence of the two body system at store deployment. The suction force acting upon the store is not observed for identical static cases at equivalent fixed separation distances. This finding indicates that a static system does not accurately capture the body forces of a dynamic store separation event. When the store is stowed slightly offset of the carrier base prior to deployment, it separates further than when the store is stowed flush to the carrier. This phenomenon is due to an increase in mean pressure and thus a decrease in drag on the two-body system. A pre-deployment reduction in drag on the carrier effectively reduces the required ejection force necessary for a safe store separation.

15. SUBJECT TERMS
computational fluid dynamics, aft store separation, base pressure, sphere cone re-entry, supersonic drag

16. SECURITY CLASSIFICATION OF:			17. LIMITATION OF ABSTRACT	18. NUMBER OF PAGES	19a. NAME OF RESPONSIBLE PERSON
a. REPORT	b. ABSTRACT	c. THIS PAGE			Dr. Mark F. Reeder
U	U	U	UU	148	19b. TELEPHONE NUMBER (Include Area Code) (937) 255-3636, ext 4530; e-mail: mark.reeder@afit.edu

Standard Form 298 (Rev. 8–98)
Prescribed by ANSI Std. Z39.18